Electrospinning as a Potential Electrode Preparation Technique for PEM Fuel Cells

Inaugural-Dissertation
to obtain the academic degree
Doctor rerum naturalium (Dr. rer. nat.)

submitted to the Department of Biology, Chemistry and Pharmacy

of Freie Universität Berlin

by

Manoj Krishna Kayarkatte Narayan

from Mangalore, India

2017

The present work was prepared in the period from July 2013 to December 2016 at the Institute of Chemistry at the Freie Universit ät Berlin under the guidance of Prof. Dr.-Ing Christina Roth. Parts of this work have been published. The relevant publications are referred to in each section.

1 st Reviewer: Prof. Dr.-Ing. Christina Roth
2 nd Reviewer: Prof. Dr.-Ing. Arne Thomas

Date of defence: 24.01.2017

My humble effort I dedicate this thesis to my sweet and loving

Amma & Appa,

whose affection, love, encouragement and prayers

make me able to get such success and honour.

Declaration

I hereby declare that I have this work written independently and have used no other than the specified sources and aids.

Manoj Krishna Kayarkatte Narayan Berlin

Acknowledgements

First and foremost I offer my sincerest gratitude to my PhD *guru*, Prof. Christina Roth, who has supported me throughout my thesis with her knowledge whilst allowing me the room to work in my own way. She provided a friendly atmosphere, gave freedom to explore newer ideas, supported for the conferences which motivated me to work harder. Her degree of commitment and enthusiasm to the work with a stupendous amount of energy will be remembered and followed in my career.

I thank Prof. Arne Thomas for accepting to be the second supervisor. I also thank the committee members for their valuable time.

On this occasion I would like to convey my appreciativeness towards "ERASMUS MUNDUS PhD scholarship", organized by European Union. I thank the Erasmus Mundus team for the initial arrangements for the stay and taking care when I arrived new in Berlin. I also thank Dahlem Research School for financing my last half year of my stay.

I am indebted to my lab mates for providing a fun and happening environment to work and learn. Without their precious support it would not be possible to conduct this research. I thank in particular Öznur, Aseem and Anastasia for contributing to the thesis. I also thank my friends in Berlin for making the 3.5 years stay memorable.

I thank Anjana, my *fiancee*, being supportive and going through all the pains to correct this thesis.

I owe special thanks to my parents and my sister, who encouraged me, prayed for my happiness and well being. This thesis is dedicated to them.

Summary

In this thesis, the potential of the electrospinning technique as a tool for the preparation of fuel cell electrodes was studied.

In the first part of the work, electrospinning was used to prepare porous electrode structures that allow for rapid transport of both fuel and water as well as protons and electrons to and from the electrodes. A solution containing polyacrylonitrile (10 wt.%) and a small amount of carbon nanotubes (0.25 wt.%) was electrospun to get highly porous structures. The pyrolsis of the structure results in carbon nanotube enforced carbon nanofiber networks which are freestanding. Pt was deposited on the surface of the fiber structure via impregnation of Pt precursor and successive reduction with sodium borohydride. X-ray diffractogram showed a crystal size of 5.3 nm, transmission electron micrographs showed a uniform distribution of Pt nanoparticles on the network. Electrochemical surface area (ECSA) was calculated as 30.1 m^{-2} g_{Pt}^{-1}. The catalyst layer which retained its morphology, was hotpressed as cathode electrode for testing in a fuel cell test-bench. The electrospun catalyst performed better at higher potential (between 0.95 V and 0.6 V) and poorer at high currents. From the ECSA, calculated using in-situ cyclic voltammetry, a high Pt utilization of approx. 90% for a loading of 0.3 mg_{Pt} cm^2 was demonstrated. In comparison, a standard electrode prepared via the air-brush technique had a catalyst utilization of 60% for the same loading. A new technique for fabrication of catalyst layers independent of ink formulation was hence successfully developed.

In the second part of the work, the role of polyacrylic acid (PAA) in enhancing the stability of the electrodes was studied. Polyacrylic acid is a common additive for electrospinning Nafion. Here, an electrode containing PAA/Nafion polymer as support for Pt nanoparticles was prepared. Pt nanoparticles were produced by photochemical reaction of the Pt precursor induced by UV light. PAA-Nafion was added to the solution covering the Pt nanoparticles and thereby separating Pt particles from carbon. By this approach, the Pt enhanced carbon corrosion was decreased. The prepared electrode was characterized by both physical and electrochemical characterization techniques. From the potential cycling experiment, it was revealed that Pt nanoparticles were indeed separated from carbon particles due to which there was no change in crystallite sizes of Pt before and after cycling. This was also confirmed by accelerated degradation studies in a fuel cell test-bench which showed that 52% of the ECSA was retained after 5000 cycles, whereas the commercial catalyst lost most of its activity in the first 2000 cycles.

The results suggest use of electrospinning as an indispensable tool for designing advanced fuel cell electrodes.

Zusammenfassung

In dieser Arbeit wurde das Potenzial des Elektrospinnverfahrens für die Herstellung von Brennstoffzellelektroden untersucht.

Im ersten Teil der Arbeit wurden poröse Elektrodenmaterialien mittels des Elektrospinnverfahrens hergestellt. Die hergestellten Materialien wiesen Strukturen auf, die sowohl eine hohe Permittivität für Gase, Wasser und Protonen, als auch eine hohe Elektronenleitfähigkeit besaßen. Eine Lösung aus Polyacrylnitril (10 wt.%) und einem geringen Anteil an Kohlenstoffnanoröhren (0,25 wt.%) wurde versponnen, um hochporöse Strukturen zu erhalten. Die Pyrolyse dieses Materials ergab freistehende Kohlenstoffnanofasernetzwerke, welche durch die Kohlenstoffnanoröhren stabilisiert wurden. Das Platin wurde anschließend über einen Pt-Precursor auf die gesponnenen Kohlenstoffstrukturen aufgebracht und anschließend mit Natriumborhydrid reduziert. Röntgenbeugungs Untersuchungen ergaben eine Platinpartikelgröße von 5,3 nm und Transmissionsmikroskopische Aufnahmen zeigten eine gleichmäßige Verteilung des Katalysators auf dem gesponnenen Material. Aus Berechnungen ging eine elektrochemisch aktive Oberfläche von 30,1 $m^2\ g_{Pt}^{-1}$ hervor. Die Morphologie der Katalysatorschicht blieb erhalten, was die Herstellung einer Elektrode durch Heißpressen erlaubte. Diese Elektrode wurde anschließend auf der Kathodenseite der Brennstoffzelle untersucht. Die elektrogesponnene Elektrode wies höherer Leistung in hohen Potentialbereichen zwischen 0,95 V bis 0,6 V auf. Die Leistung bei hohen Strömen war jedoch geringer. Durch die in-situ Bestimmung der elektrochemisch aktiven Oberfläche mittels zyklovoltermmetrischer Messungen, konnte eine Platinausnutzung von ca. 90 % für eine Beladung von 0,3 $mg_{Pt}\ cm^{-2}$ nachgewiesen werden. Zum Vergleich wurde eine Standardelektrode, die mit dem Heißsprayverfahren hergestellt wurde, herangezogen. Diese wies eine Platinausnutzung von 60% für eine vergleichbare Beladung auf. Somit wurde ein neues Verfahren zur Herstellung von Brennstoffzellenkatalysatoren entwickelt, die unabhängig von der Formulierung des Tintenrezeptes ist.

Im zweiten Teil dieser Arbeit wurde der Einfluss von Polyacrylsäure auf die Verbesserung der Stabilität der elektrogesponnenen Elektroden untersucht. Polyacrylsäure ist ein gängiges Additiv, dass zum Elektrospinnen von Nafion verwendet wird. Daher wurden Elektroden aus Polyacrylsäure/Nafion-Polymeren zur Stabilisierung von Platinnanopartikeln hergestellt. Die Platinnanopartikel wurden mittels einer durch UV-Licht induzierten photochemischen Reaktion des Platin-Precursors hergestellt. Polyacrylsäure/Nafion wurde hinzugegeben, wodurch die Platinpartikel umschlossen wurden und somit vom Kohlenstoffträger separiert blieben. Durch diesen Ansatz wurde die durch Platin induzierte Korrosion des Kohlenstoffträgermaterials verringert. Die hergestellten Elektroden wurden sowohl mit physikalischen, als

auch mit elektrochemischen Methoden charakterisiert. Durch das Zyklieren des Potentials konnte gezeigt werden, dass die Platinpartikel tatsächlich keinen direkten Kontakt zum Kohlenstoffträger hatten, da die Partikelgröße nach dem Experiment unverändert blieb. Dies wurde zusätzlich durch beschleunigte Alterungstests in einem Brennstoffzellenteststand bestätigt. Außerdem konnte dabei nach 5000 Zyklen eine elektrochemisch aktive Oberfläche von 52% nachgewiesen werden. Im Vergleich dazu verliert ein kommerziell erhältlicher Katalysator bereits nach 2000 Zyklen den Großteil seiner Aktivität.

Die Ergebnisse belegen, dass das Elektrospinnen das Potenzial besitzt zu einer unverzichtbaren Methode zur Herstellung von maßgeschneiderten Elektroden für die Brennstoffzelle zu werden.

Contents

List of Figures

List of Tables

Symbols and Abbreviations

AFC	Alkaline fuel cell
CNF	Carbon nanofiber
CNT	Carbon nanotube
CV	Cyclic voltammetry
DL	Diffusion layer
DMFC	Direct methanol fuel cell
DOE	Department of energy
ECSA	Electro-chemical surface area, (m^2 $g_{Pt}{}^{-1}$)
FCCJ	Fuel cell corportation Japan
FTIR	Fourier transform infrared spectroscopy
GCE	Glassy carbon electrode
GDL	Gas diffusion layer
MCFC	Molten carbonate fuel cell
MEA	Membrane electrode assembly
MSA	Mass specific activity, mA $mg_{Pt}{}^{-1}$
SHE	Standard hydrogen electrode
ORR	Oxygen reduction reaction
PEM	Proton exchange membrane
PAFC	Phosphoric acid fuel cell
PAA	Polyacrylic acid
PAN	Polyacrylonitrile
PGM	Platinum group metal
SEM	Scanning electron microscopy
SMSI	Strong metal support interaction
SOFC	Solid oxide fuel cell
TEM	Transmission electron microscopy
TGA	Thermogravimetric analysis
TPB	Triple phase boundary
XRD	X-ray diffraction

ΔG	Change in Gibbs free energy, J
n	Number of electrons
F	Faraday's constant, 96,487 C $gmole^{-1}$
°C	Degree in celsius
i	Current, A
r	Resistance, ohm
T	Temperature, °C
β	Line broadening at FWHM in radians
τ	Mean crystallite size, nm
h	Planck's constant, $6.62606810^{-34} m^2 kgs^{-1}$
E	Ideal cell potential
V	Actual cell potential

S	Surface area, m^2
θ	Angle, $radians$
d	Interplanar distance, nm
$K\alpha$	Wavelength of the X-ray source, m
λ	Wavelength, m
K	Shape factor
j	Current density $A\ cm^{-2}$
W_{el}	Electrical work done, J
m	Mass, kg
P	Pressure, $N\ m^{-2}$
H	Enthalpy, J
ϵ	Efficiency
η	Overall efficiency
v	Volume, m^3
c	BET constant
N	Avogadro's number (6.022×10^{23})
Γ	Charge to oxidize a monolayer of H_2 on Pt, 210 $\mu C cm^{-2}$
L	Pt loading $g\ m^{-2}$
Q_{pt}	Charge on Pt, $C\ cm^{-2}$

Chapter 1

Introduction and motivation

Today's world is marked by rapid changes and striking technological inventions, changing the way of life forever. The rapid economic and technological advances have increased the energy demand of the world. The world energy consumption has doubled in the last 30 years and the world is still dependent on fossil fuels as the primary source of energy. Together, petroleum oil, coal and natural gas share approximately 66% of the global energy usage [1]. The combustion of these fossil fuels has resulted in an increase in emission level of carbon dioxide along with other toxic gases. The emission of CO_2, a green-house gas, has outbalanced the natural equilibrium in this decade and is increasing steadily with a rate of 3.0%, as of the year 2015. A direct consequence of this is seen in the rise in temperature around 0.094 °C per year resulting in increasing sea level and decreasing ice sheets [2].

In order to reduce CO_2 emission levels, dependence on renewable, environmentally-friendly energy technologies should be emphasized. For stationary appliances, wind, solar and hydroelectric power are considered. For portable and automotive purposes, fuel cells, like proton exchange membrane (PEM) fuel cells, and batteries, like Li-ion, Li-air, are seen as the clean alternative technologies. Both fuel cells and rechargeable batteries provide electricity. While the former converts chemical energy of the fuel to electricity, the latter provides electricity from the energy stored inside the cell whenever required. Both technologies complement each other providing energy for the future.

Although fuel cells are clean and energy efficient, the benchmarks needed for a commercial success are not achieved owing to cost and durability factors. The major challenge being the electrode of the fuel cell.

The price tag associated with the noble metal (platinum-based) catalysts for the power output delivered, is one of the prominent factors determining the cost of the fuel cell systems. To reduce the Pt loading in the electrode, many strategies have been employed like alloying [3], core-shell [4], Pt-free concepts, etc. [5]. Not only improving catalyst activity is important but also improving the accessibility and utilization of the catalyst is essential. An electrode should efficiently transport protons from the membrane, electrons from the current collector to the catalyst and the reactant and product gases to and from the catalyst. Research on the electrode structure is pivotal and currently many alternative techniques to prepare PEM fuel cell membrane-electrode-assemblies (MEAs) to the conventionally prepared standard

catalyst-coated membrane [6, 7] and catalyst-coated gas diffusion electrode [8] have been developed like plasma sputtering [9], ion beam bombardment [10], electrodeposition [11], electrospray [12], inkjet printing [13] etc. These techniques, however, are largely dependent on ink formulation, and depending on the formulation the structure of the layer is formed. The dispersion medium governs the ink's properties like viscosity, dispersion and aggregation size of the catalyst/ionomer particles, rate of solidification and finally the mass, electron and proton transport properties of the catalyst layer.

As mentioned earlier, another issue persisting with the fuel cells is the durability of the electrodes. The carbon used as catalyst support exhibits corrosion in fuel cell operating conditions. The instability of the carbon support results in loss of Pt surface area following both Pt sintering and Pt release from the carbon support. In this regard, many attempts are done by replacing the support material with stable ceramic oxides [14] and polymer supports [15]. The alternative materials provide the required stability, but conduct electrons poorly, affecting the fuel cell performance. Also, they tend to form a dense electrode structure and educts and products cannot diffuse easily. Strategies to mitigate the poor conductivity and prepare porous electrode structures need to be developed.

This work addresses these two issues by using the technique of electrospinning. Electrospinning is a fascinating technique with which fibers of very small diameter can be drawn from a polymer solution.

Electrospinning of polyacrylonitrile and successive pyrolysis forms carbon nanofibers which can be used to form the electrode structure. In this thesis, a new technique of electrode preparation is developed, by preparing an interconnected porous fiber network using electrospinning.

Electrospinning of Nafion along with the catalysts increases the triple phase density of the electrodes increasing the performance of the electrodes. To make this possible, a small amount of polymers such as polyacrylic acid, poly ethylene oxide etc. needs to be added. The addition of these polymers does not only influence the performance but also the stability of the electrodes. The stability of one such system involving polyacrylic acid and Nafion is evaluated and the potential of PAA to stabilize the Pt nanoparticles is discussed.

Chapter 2

Theory

A fuel cell is an electrochemical cell that converts chemical energy of a fuel into electrochemical energy. It holds a great promise as a clean and efficient energy technology for the future.

The principle of the fuel cell was discovered by German scientist Christian Friedrich Schönbein in 1838 and published in one of the scientific magazines of that time. In 1839 the first fuel cell was conceived by Sir William Robert Grove, a Welsh judge, inventor and physicist in an edition of a Philosophical Magazine and Journal of Science and later sketched, in 1842 (Figure 2.1).

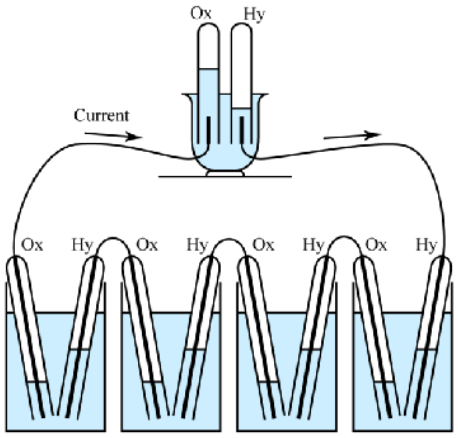

Figure 2.1: First fuel cell sketch by Sir W. Grove

2.1 Type of fuel cells

There are several types of fuel cells under construction. They can be classified according to electrochemical reactions, electrolyte employed, kind of catalysts required, the operating temperature range etc. Some of the important types of the fuel cells are summarized in Table 2.1 classified based on their operating temperature.

Each type of fuel cell has its own unique advantages and disadvantages making it useful for certain applications. In the following section, proton exchange membrane fuel cells are discussed in length which are in the forefront for commercialization and the main focus of this work.

Table 2.1: Different types of fuel cells and their characteristics.

Fuel cell types	**Operating temperature (K)**	**Current density**	**Charge carrier**	**Electrodes**	**Cell Reactions: Anode Cathode**
Proton exchange membrane fuel cell (PEMFC)	303-353	High	H^+	Pt	$2\,H_2 \rightarrow 4\,H^+ + 4\,e^-$ $O_2 + 4\,H^+ + 4\,e^- \rightarrow 2H_2O$
Alkaline fuel cell (AFC)	353-373	High	OH^-	Ni/Ag metal oxides, Noble metals	$2\,H_2 + 4\,OH^- \rightarrow 4\,H_2O + 4\,e^-$ $O_2 + 2\,H_2O + 4e^- \rightarrow 4\,OH^-$
Phosphoric acid fuel cell (PAFC)	373-493	Moderate	H^+	Pt	$2\,H_2 \rightarrow 4\,H^+ + 4\,e^-$ $O_2 + 4\,H^+ + 4\,e^- \rightarrow 2\,H_2O$
Molten carbonate fuel cell (MCFC)	873-973	Moderate	${CO_3}^{-2}$	Ni anode, NiO cathode	${CO_3}^{2-} + H_2 \rightarrow H_2O + CO_2 + 2\,e^-$ $CO_2 + \frac{1}{2}\,O_2 + 2\,e^- \rightarrow {CO_3}^{-2}$
Solid oxide fuel cell (SOFC)	973-1273	High	O	Co-ZrO_2, $NiZrO_2$ anode $Sr-LaMnO_3$ cathode, Y_2O_3 stabilized ZrO_2 electrolyte	$H_2 + \frac{1}{2}\,O^{2-} \rightarrow H_2O + 2\,e^-$ $H_2 + \frac{1}{2}\,{O_2}^{+}{}_2e^- \rightarrow O^{2-}$

2.2 Proton exchange membrane fuel cells

A fuel cell in general consists of an electrolyte (an ion-conducting material: liquid or solid) in contact with two electrodes (mostly Pt-based) capable of converting any consumable fuel directly to electrical energy via a chemical reaction. In PEM fuel cells, the hydrogen gas is used as the fuel and oxygen/air is used as oxidizing agent. The combustion reaction can be split into two electrochemical half cell reactions with hydrogen oxidation reaction (HOR) taking place at anode and oxygen reduction reaction (ORR) at cathode as shown:

$$\text{Anode reactions (HOR):} \quad \mathrm{H_2} \rightarrow 2\mathrm{H^+} + 2\mathrm{e^-} \quad E = 0\ V_{SHE} \tag{2.1}$$

$$\text{Cathode reactions (ORR):} \quad \frac{1}{2}\mathrm{O_2} + 2\mathrm{H^+} + 2\mathrm{e^-} \rightarrow \mathrm{H_2O} \quad E = 1.229\ V_{SHE} \tag{2.2}$$

$$\text{Overall cell reactions:} \quad 2\,\mathrm{H_2} + \mathrm{O_2} \rightarrow 2\mathrm{H_2O} \quad E = 1.229\ V_{SHE} \tag{2.3}$$

Figure 2.2 shows a very simple representation of a typical fuel cell. At the anode, where the oxidation of hydrogen takes place, the newly formed protons permeate through the polymer electrolyte membrane to the cathode side. The electrons travel along an external load circuit to the cathode side, thus creating the current output of the fuel cell. Meanwhile, a stream of oxygen is delivered to the cathode side. Here, oxygen molecules react with the protons permeating through the proton exchange membrane and the electrons arriving through the external circuit to form water molecules. The reduction of oxygen is a sluggish reaction and requires a lot of noble metal catalyst.

As water is the major exhaust product of the fuel cells, they are considered as clean energy. Also, since the fuel is directly converted to electricity the efficiencies are much higher than the conventional fossil fuel based devices. High efficiencies can be maintained for partial or variable loadings. The operating temperature of the fuel cell is around 80°C. These features make it ideal to power many different devices. Fuel cells have been used for a variety of applications as shown in Figure 2.3. In transport, fuel cells have been used, especially in indoor applications like forklifts, where the clean emissions are important to maintain air quality. Much efforts are done by different car manufacturers like Honda, Daimler, Toyota etc. to bring out zero-emission cars that emit only water and heat. As of June 2016, the Toyota Mirai (Figure 2.3a) is available for retail sale in Japan, California, the UK, Denmark, Germany, Belgium, and Norway costing around USD 60,000.

Many buses running on fuel cells are operating worldwide. One such bus, named Citaro from Mercedes is shown in Figure 2.3b. These vehicles are highly efficient even if the hydrogen is produced from fossil fuels and thus reducing CO_2 emissions which would become zero if the hydrogen is produced from renewable sources. In addition, they assist

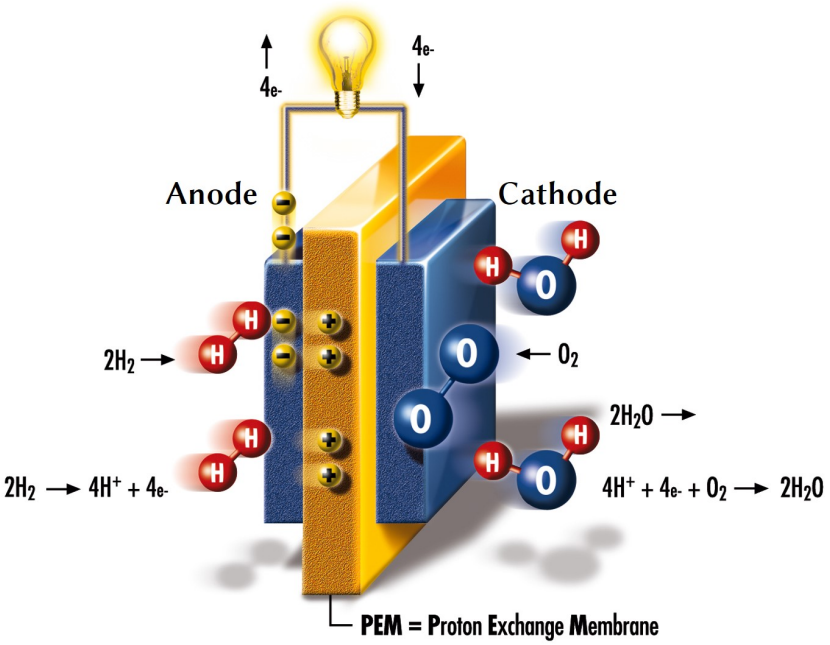

Figure 2.2: Schematic of the processes taking places in a PEM fuel cell [16].

in reducing noise pollution. Fuel cells are also used in aeroplanes, ships etc. for use in commercial as well as military purposes. In case of stationary applications, fuel cells that are used at high temperature, with co-generation (heating unit) can have efficiencies up to 85%. Fuel cells can be used as a back-up power and have been used in many buildings and the power can also be fed into the grid. Figure 2.3c shows the Chevron's fuel cell station setup in California USA. There is a growing market for fuel cells in mobile phones (Figure 2.3d), laptops and portable electric devices. Water treatment plants and waste dumps are beginning to use fuel cells to carry out the process of converting the methane gas produced for electricity generation.

2.2.1 Fuel cell performances

Total energy is composed of free energy (G) and unavailable energy (TS). The maximum electrical work (W_{el}) obtainable in a fuel cell operating at constant temperature and pressure is given by the change by Gibbs free energy (ΔG) of the electrochemical reaction:

$$W_{el} = \Delta G = -\Delta n F E \tag{2.4}$$

where n is the number of electrons participating in the reaction, F is Faraday's constant (96,487 coulombs/gmole electron), and E is the ideal potential of the cell.

(a) Toyota Mirai fuel cell car [17]

(b) Mercedes Citaro fuel cell bus [18]

(c) Chevron's fuel cell station [19]

(d) Toshiba's DMFC powered cellphone charger [20]

Figure 2.3: Fuel cell applications: From power generators to mobile phone charger.

For the reactions taking place in a fuel cell ($H_2 + \frac{1}{2}O_2 \rightarrow H_2O$), the ideal performance of the cell is defined by its Nernst potential (E):

$$E = E^\circ - \frac{RT}{nF} \ln \frac{[C]^c[D]^d)}{([A]^a[B]^b} \tag{2.5}$$

$$E = E^\circ + \frac{RT}{nF} \ln(\frac{a_{H_2} * a_{O_2}^{0.5}}{a_{H_2O}}) \tag{2.6}$$

where a is the activity of the gases, which can be related to the partial pressure of the gases.

The reaction has a Gibbs free energy change of -237 kJ/mol under the standard conditions for liquid water product. The reversible voltage generated can be calculated as

$$E^\circ = \frac{-\Delta G^\circ}{nF} = \frac{237000 \frac{J}{mol}}{296400 \frac{C}{mol}} = 1.23 \text{ V} \tag{2.7}$$

2.2.2 Efficiencies of electrochemical cells

Overall efficiency

Overall efficiency of electrochemical energy conversion depends on intrinsic efficiency (ϵ_i), voltage efficiency (ϵ_e) and faradaic efficiency (ϵ_f) and can be given by:

$$\epsilon = \epsilon_\text{i}\ \epsilon_\text{e}\ \epsilon_\text{f} \tag{2.8}$$

Intrinsic maximum efficiency

Intrinsic maximum efficiency is defined thermodynamically as ratio of Gibbs free energy to enthalpy change.

$$\epsilon_i = \frac{\Delta G}{\Delta H} \tag{2.9}$$

At standard conditions of 25 °C and 1 atmosphere, the thermal energy (ΔH) in the hydrogen-oxygen reaction is 285.8 kJ/mole, and the free energy available for useful work is 237.1 kJ/mole. Thus, the thermal efficiency of an ideal fuel cell operating reversibly on pure hydrogen and oxygen at standard conditions would be:

$$\eta_{ideal} = \frac{237.1}{285.8} = 83\% \tag{2.10}$$

which is high compared to a combustion engine which has a low efficiency at room temperature and has a maximum efficiency of 73% at a working temperature of 816 °C.

Voltage efficiency

Voltage efficiency is defined as cell voltage under load to thermodynamic reversible potential.

$$\epsilon_e = \frac{E}{E_r} \tag{2.11}$$

The actual cell potential is decreased from its equilibrium potential because of irreversible losses. Multiple phenomena contribute to irreversible losses in an actual fuel cell. The losses, which are called polarization, over potential or over voltage (η), originate primarily from three sources:

1. Activation polarization (η_{act}),
2. Ohmic polarization (η_{ohm}) and
3. Concentration polarization (η_{conc}).

Activation polarization (η_{act}): This loss is due to the energy barrier, which must be overcome in order for the electrochemical reaction to occur. The activation potential can be considered to be the extra potential required to reduce the activation energy barrier of the rate-limiting step to a value such that the electrode reaction proceeds at the desired rate.

Activation region also called kinetic control region is the region where Tafel plot is valid.

$$\eta_{act,c} = b_c \, log(\frac{i}{i_0}) \tag{2.12}$$

where b_c is the Tafel slope, i_0 is the exchange current determined by extrapolating the iR-corrected cell voltage to the theoretical potential, E_{theor}. Activation losses is attributed to the catalysts used and also varies with the size and shape of the catalyst

Ohmic polarization (η_{ohm}): Ohmic losses occur because of resistance to the flow of ions in the electrolyte and resistance to flow of electrons through the electrode. The dominant ohmic losses through the electrolyte are reduced by decreasing the electrode separation and enhancing the ionic conductivity of the electrolyte. As the electrolyte and fuel cell electrodes obey Ohm's law, the ohmic losses can be expressed by the equation $\eta_{\text{ohm}} = IR$, where, I is the current flowing through the cell, and R is the total cell resistance, which includes electronic, ionic, and contact resistance. η_{ohm} can be calculated using current interrupt technique. Generally, membranes are the main contributor of ohmic losses.

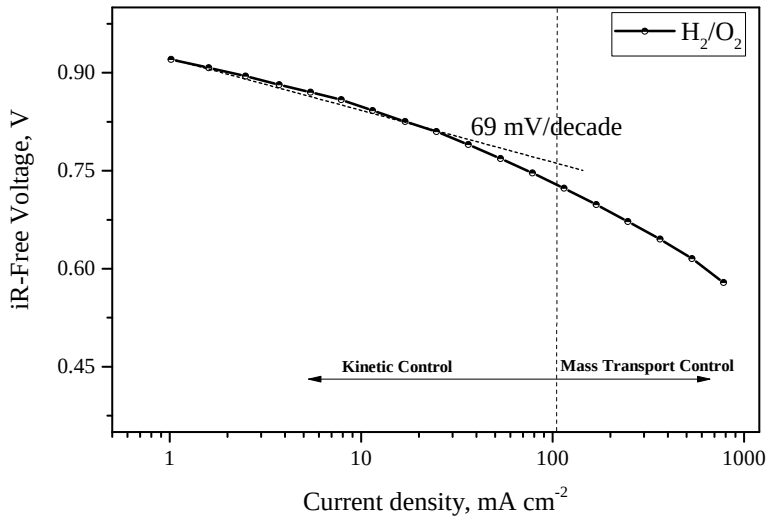

Figure 2.4: Semi-log plot of iR free voltage vs. current density highlighting the difference of kinetic control region and mass transport control region for a in house prepared catalyst.

Concentration polarization ($\eta_{\mathbf{conc}}$): As reactant is consumed at the electrode by electrochemical reaction, there is a loss of potential due to the inability of the surrounding material to maintain the initial concentration of the bulk fluid. That is, a concentration gradient is formed . At practical current densities, slow transport of reactants and products to and from the electrochemical reaction site is a major contributor to concentration polarization.

$$\eta_{conc} = \frac{RT}{nF} \ln \frac{C_s}{C_b} \tag{2.13}$$

where, C_s is concentration at the surface and C_b is bulk concentration. It can be also shown that

$$\eta_{conc} = \frac{-RT}{nF} \ln \left(1 - \frac{i}{i_l}\right) \tag{2.14}$$

where, i_l = limiting current (i.e current when concentration is C_s).

Concentration polarization can also be calculated as:

$$\eta_{conc} = E_{theor} - E_{cell} - |\eta_{act,c}| - \eta_{ohm} \tag{2.15}$$

Figure 2.5 shows the different polarization curves and associated losses attached with it, for a 50 cm^2, single-cell, H_2-air, having anode and cathode loadings of 0.4 mg_{Pt} cm^{-2}.

Figure 2.4 tries to differentiate these regions using a semi-log plot. The ohmic region is eliminated by performing IR corrections and compensating with the voltage.

Electrode structuring plays an important role in decreasing the concentration polarization.

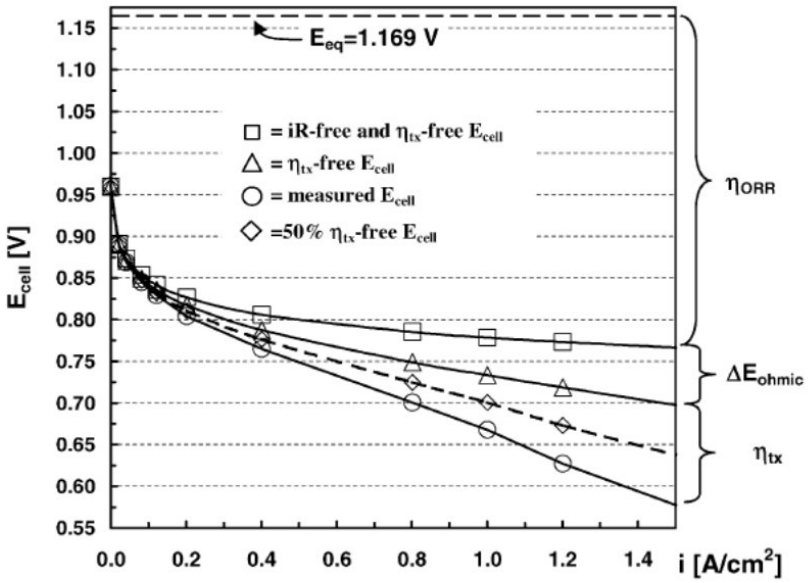

Figure 2.5: Fuel cell polarization curve showing different losses as described by Gasteiger et al. [21]. The nomenclature used $\eta_{\text{ORR}} = \eta_{\text{act}}$, $\Delta E_{\text{ohmic}} = \eta_{\text{act}}$ and $\eta_{\text{tx}} = \eta_{\text{conc}}$. Catalyst loading anode and cathode 0.4 mg_{Pt} cm^{-2}. Temperature of the cell 80 °C.

Faradaic efficiency

Efficiency is reduced if not all reactants are converted to reaction products, or if some electrons are involved in alternative reactions such as corrosion. For 100% conversion the cell current density (j_F) is given by Faraday's law:

$$j_F = ZF\frac{df}{dt} \tag{2.16}$$

where, f represents the amount of fuel supplied (mol), Z is the number of electrons transferred per molecule of fuel. For incomplete conversion the current density produced is given by:

$$j_F = ZF(\frac{df}{dt})_{consumed} \tag{2.17}$$

Hence the current/faradaic efficiency is given by:

$$\epsilon_f = \frac{j}{j_f} \tag{2.18}$$

These losses result in a cell voltage (V) that is less than its ideal potential, E i.e $V = E - Losses$

2.2.3 Components of PEM fuel cells

A conventional PEM fuel cell consists of a so-called **membrane electrode assembly (MEA)** compressed between an anode and a cathode bipolar plate. Membrane electrode assembly is a multi-layered structure that is composed of an **anode diffusion layer (DL)**, an **anode catalyst layer (CL)**, a **polymer electrolyte membrane (PEM)**, a **cathode diffusion layer (DL)**, and a **cathode catalyst layer (CL)** as shown in Figure 2.7.

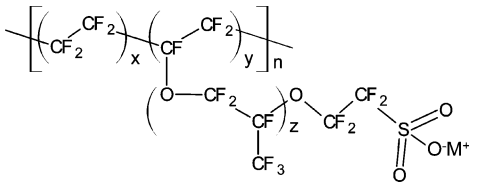

Figure 2.6: Structure of Nafion

A proton exchange membrane or polymer electrolyte membrane (PEM) is a semi permeable membrane generally made from ionomers and designed to conduct protons while being impermeable to gases such as oxygen or hydrogen. They provide electric insulation between anode and cathode. Typically, perfluorinated sulfonic acid ion exchange membranes developed by DuPont and trademarked as Nafion are used in fuel cells. Chemical structure of Nafion is shown in Figure 2.6. Nafion membrane absorbs water to form cluster networks, and the transfer of protons takes place via a Grotthuss hopping mechanism [22].

Catalyst layer consists of catalysts with Nafion ionomer to provide triple-phase boundaries for the hydrogen/fuel oxidation and oxygen reduction reactions, to facilitate the simultaneous transport of protons, electrons and reactants/products. Generally, noble nano metals like nano Pt dispersed on catalyst support catalyze the reaction.

The diffusion layers at both anode and cathode are made of two layers, a backing layer made of carbon cloth or carbon paper, and a micro porous layer composed of hydrophobic polymer and carbon powder. The function of each DL is to provide a support to the corresponding CL and to distribute reactants over the catalyst layer, and to conduct electricity to the current collector. The water generated on the cathode is vented out of the cell.

The anode and cathode electrode plates also called bipolar plates or end plates, usually incorporate flow channels for the fluid and gas feeds and may contain conduits for heat transfer. In a fuel cell stack, these plates act as anode for one cell and as cathode for other.

A brief summary of fuel cell components and their function in the assembly is tabulated in Table 2.2.

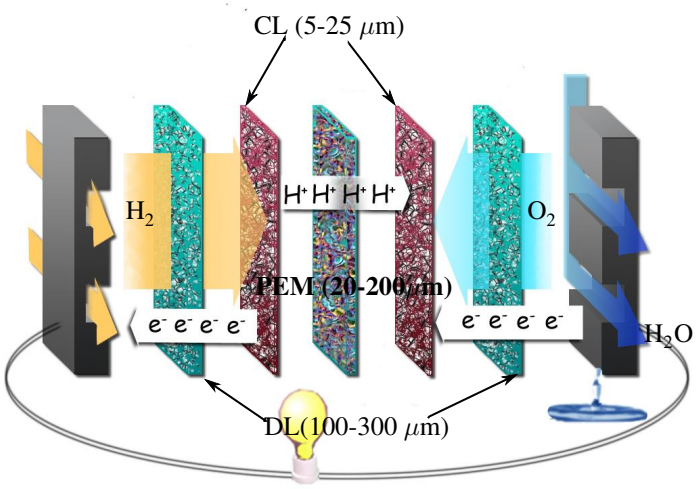

Figure 2.7: Components of single fuel cell

Table 2.2: PEM fuel cell components and their functions

Components	Function	Properties	Materials used
Catalyst	Facilitate HOR and ORR	Catalytically active, high surface area, physical and chemical stability in fuel cell conditions	Pt, Pt alloys
Catalyst support	Prevents catalyst sintering, facilitates reactant and electron transport	Porous, large surface area, electrically conductive, stable in fuel cell conditions.	High surface area carbon, doped TiO_2 etc.
Gas diffusion layer	Uniformly distributes the gaseous and liquid reactants, water management, provides electron path to the external circuit.	High electrical conductivity, pores for gas transport	Teflon treated carbon paper and woven cloth
Membrane	Conducts protons, separates the anode and cathode reactant from mixing	High proton conductivity, non-permeable to the reactants.	Nafion

2.3 Challenges in PEM fuel cells

PEM fuel cells find a major application in the automotive and portable fields as a clean energy technology. However, for their commercialization, they have to overcome the two major hurdles i.e cost and durability of the cells.

A breakdown of the cost estimates by DOE (Figure 2.8) indicates that for a large scale manufacturing, the cost of the catalyst and its application make up to 45% of the total costs [23]. Roughly for commercial success, the Pt content should be less than 8 g per car i.e a power output 5 KW/g_{Pt} with efficiency greater than 50%. For example, the Pt content in the Toyota Mirai 2015 model has a loading of roughly 30 g of Pt [24]. A gram of pure Pt costs between 30 € to 40 € per gram in 2016. Except for the electrode, development of inexpensive membranes which can withstand high temperatures and cheaper bipolar plate materials are also necessary.

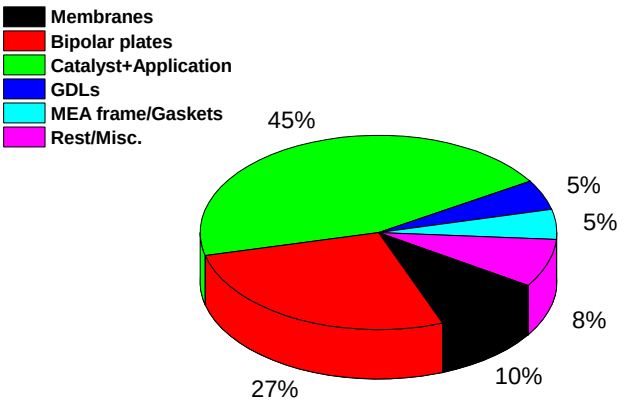

Figure 2.8: Projected cost breakdown of fuel cell components for 500,000 systems per year as of 2015

Life time of a PEM fuel cell is another important factor, the requirements of which ranges from 5000 operating hours for car application, up to 20,000 hours for bus applications and up to 40,000 hours for stationary applications [25, 26]. Studies have shown that several factors can affect the durability of a PEM fuel cell. These factors include PEM thinning [27–29], catalyst layer degradation due to platinum sintering [30, 31] or carbon support corrosion [32, 33], gas diffusion layer (GDL) degradation [34, 35], bipolar plates [36]. Table 2.3 lists the important fuel cell conditions affecting the fuel cell components. Among these, catalyst layer degradation is one of the most critical factors.

Table 2.3: Fuel cell components and their degradation characteristics

Components	**Degrading condition of fuel cell**	**Effect**
Catalyst	Start- Stop cycle, rapid potential cycling	Pt dissolution and particle growth
Catalyst support	Start stop cycle, potential cycling, fuel starvation	Carbon oxidation, Pt particle growth
Membrane	Chemical attack by radical $OH^{\bullet}$ or $OOH^{\bullet}$ during ORR, mechanical failures - pin holes, substitution of proton by metal ions Na, K, Pt etc.	Loss of proton conductivity, fuel crossover
GDL	Surface oxidation by humid gas stream, mechanical stress	Loss in hydrophobicity, break in pore structure
Bipolar plates	Humid oxygen in the gas stream, mechanical stress	Increased resistance, poisoning of the membrane

2.4 Electrode performance aspects

Performance of an electrode depends on two aspects that are: *how good is the catalyst* and *how well is it structured/arranged.*

2.4.1 Catalyst activity

At the heart of the PEM fuel cell is the MEA, and catalyst inside the MEA are the working parts where the reaction takes place. Pt is the best pure metal in terms of activity, selectivity and stability for both the anode and the cathode.

At the anode, the hydrogen adsorbs onto the surface of the Pt electrode, breaking the H-H bond to give adsorbed atomic hydrogen (H-Pt or H^*) and subsequently loses an electron from each adsorbed hydrogen, which leads to hydrogen leaving the surface of the Pt as protons (H^+).

$$\frac{1}{2}\,\mathrm{H_2} + \mathrm{Pt} \xrightarrow{k_1} \mathrm{H{-}Pt} \xrightarrow{k_2} \mathrm{H^+} + \mathrm{Pt} + \mathrm{e^-} \tag{2.19}$$

The kinetics of this reaction are very fast and voltage losses are small even for very low Pt loadings.

However at the cathode, the mechanism of ORR is more complicated with sluggish kinetics. Two mechanisms are proposed. The direct pathway involves a 4 electron reaction to obtain H_2O without the formation of intermediates whereas the second pathway is the indirect pathway involving 2 electrons with formation of H_2O_2. The mechanisms are shown in Figure 2.9.

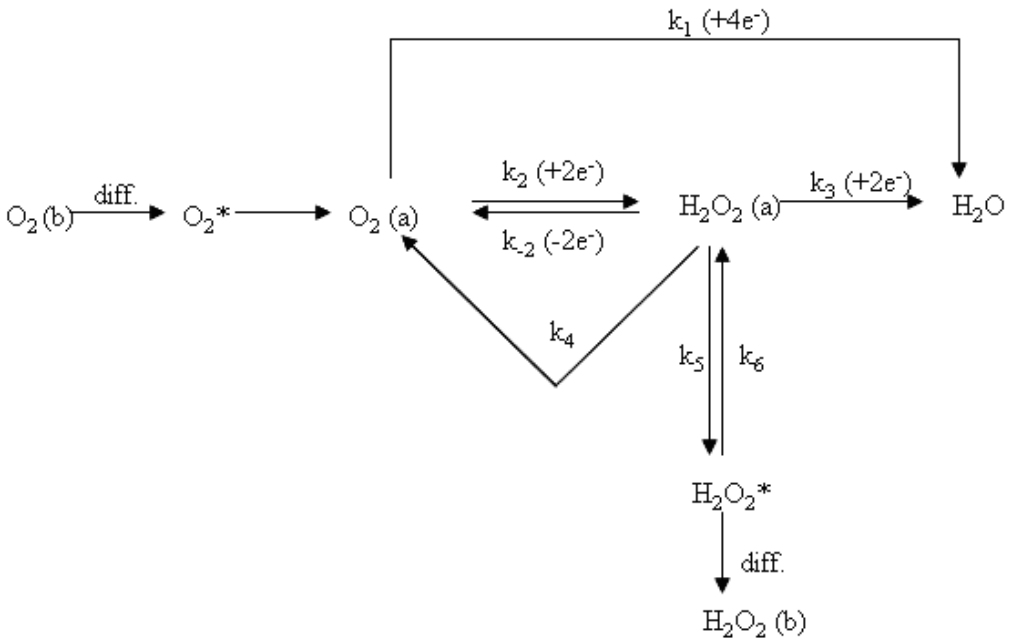

Figure 2.9: General scheme of ORR showing direct 4 electrons, and indirect 2 electrons pathways

Pt has better ORR activity than other single-element catalysts such as Pd, Ir, Ag, Au, Co, Ni, Ru, and Cu as Pt has an appropriate electronic structure for oxygen- and OH-binding [37, 38]. Still, Pt does not sit at the peak of the volcano plot for the ORR. It has been shown that alloying Pt with Cu, Ni etc., enhance their activity towards ORR. Figure 2.12 shows the volcano plot for some of the important alloys (calculated and experiment) relative to Pt. Their catalytic activities are much higher, as a result of compressive strain and electronic ligand effects.

Even though Pt alloys showed enhanced performances, the durability of these catalysts remained a concern. Exposing Pt alloys to the acidic environments and high potentials resulted in facile dissolution and oxidation of the alloyed metal, significantly decreasing their ORR activities after a long-term test. Hence, except alloying researchers have developed following techniques:

- Core-shell [4]: A core-shell concept as a new catalyst structure was developed to protect the transition metal easily dissolved from nanoparticle surfaces. In this ap-

proach, a monolayer of Pt is used to cover the surface layer of the metal, and the core-shell catalyst design is very efficient as electrochemical reactions occur only on the nanoparticle surface layer [39, 40]. A representation of core-shell model is shown in Figure 2.10.

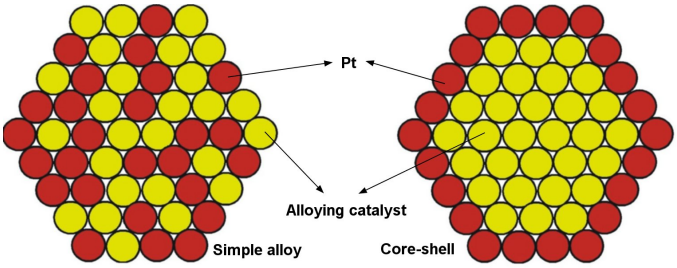

Figure 2.10: Representation of core-shell (Pt is shown in red and alloying catalyst in yellow).

- Dealloyed catalysts: In recent times, there has been an increased interest in the surface composition of the samples rather than the bulk composition of alloy nanoparticles. Dealloying is the selective removal of a less noble component from a bimetallic alloy where the competition of dissolution and surface diffusion give rise to three-dimensional metal removal and restructuring inside the bulk of the alloy. A cross-section of the cell structure of the dealloying process is represented in Figure 2.11. Dealloyed Pt catalysts are extremely active materials for the ORR catalysis in terms of their noble-metal mass based ORR activity as well as their intrinsic surface area normalized activity [41, 42].

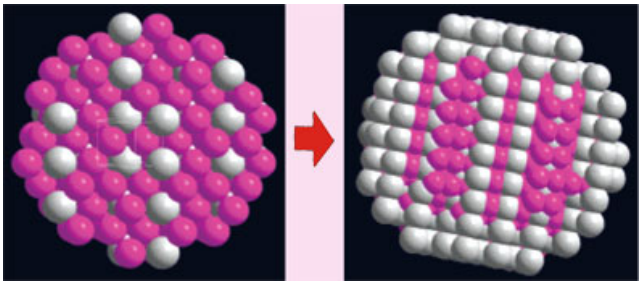

Figure 2.11: Cross-section of the cell structure of dealloying process (white - Pt atoms, pink - alloyed catalyst [43]).

Recently, non Pt group metal catalysts have also been prepared as cathode catalysts. The class of pyrolized metal porphyrins with Co or Fe under controlled conditions produce M-Nx (M = Fe,Co) which are the active sites for ORR [5, 44]. Bashyam and Zelenay [45] developed Co-polypyrole composite which showed power densities of 0.15 W cm^{-2} in a H_2/O_2 cell with no signs of degradation for more than 100 hours.

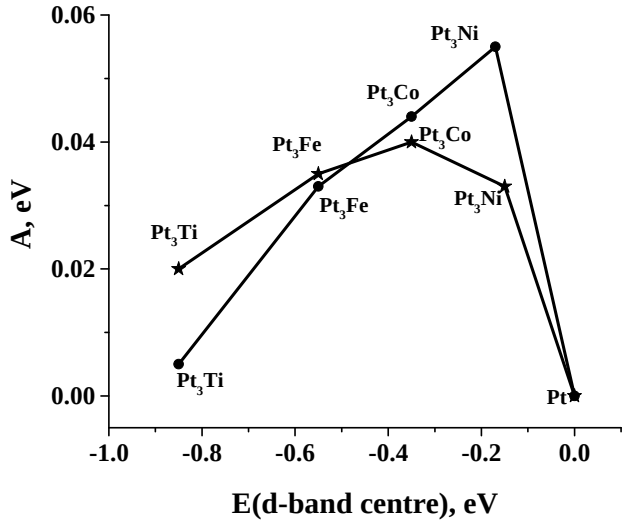

Figure 2.12: Activity versus the experimentally measured d-band centre relative to platinum. The activity predicted from DFT simulations (•), and the measured activity is ($\star$) are shown . Reproduced from [3].

2.4.2 Electrode structure

To reduce the catalyst loading in the electrode, apart from the catalyst properties, the catalyst needs to be structured in a way to maximize its accessibility and utilization. An ideal electrode has to efficiently transport protons from the membrane, electrons from the current collector to the catalyst and the reactant and product gases to and from the catalyst as shown in Figure 2.13. The performance of the electrode depends on the triple phase boundary (TPB), where the electrolyte, the catalyst, and the fuel come in contact. Kinetics of the reaction depends on the TPB, increase in TPB density will increase the reaction rate, and thus the cell performance. In order to increase the TPB density, the following factors play a role:

Porosity

Porosity of the electrode plays a vital role for fuel cell performance. Even an excellent catalyst can give poor fuel cell performance, when the resulting electrode structure is dense or disconnected. The relevant parameters like pore connectivity, pore size distribution, and pore length, influence not only the gas flow, but also the ion transport and diffusion distance.

A material can consist of three types of porosity:

1. Microporosity: Microporosity refers to porosity in the materials which have pore diameters of less than 2 nm. In a fuel cell, microstructure of a catalytic layer strongly

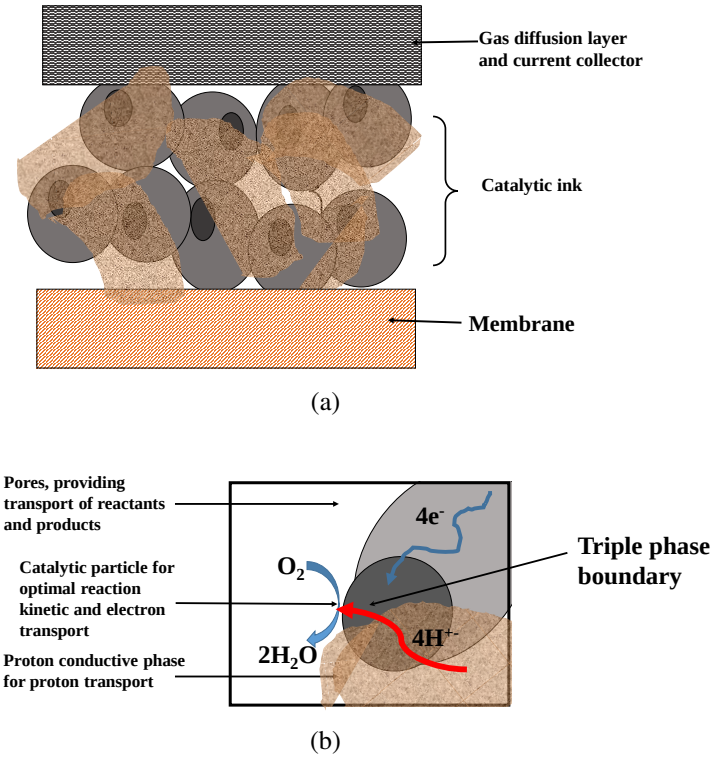

Figure 2.13: Representation of gases, protons and electron transport in a PEM fuel cell electrode

affects the gas transport rate as oxygen could diffuse fast along the grain boundaries in the layer [46]. Microporous sites in catalyst supports are important as the sites for anchoring Pt particles. As a downside, micropores are inefficient for gas and liquid flow.

2. Mesoporosity: The pores having diameter between 2 nm to 50 nm are generally regarded as mesoporous. These types of pores allow the flow of gases. Mesoporosity in the catalyst support is effective in catalyst dispersion, decreasing Pt sintering and agglomeration. The high degree of mesoporosity results in increase in geometrical surface area, unfotunately, leading to poor nafion penetration, providing inefficient proton conductivity, resulting in a poor fuel cell performance [47]. In case of unsupported Pt, intrinsic mesoporosity has shown to provide good electrochemical activity mimicking the activity of a supported catalyst [48].

3. Macroporosity: The pores of size range from 100 nm to 1000 nm in an electrode can be termed as macropores. While microporosity and mesoporosity are structural properties associated intristically with catalyst/catalyst support, macropores are formed between the catalyst agglomerates and are influenced by the fabrication technique used. Hence, they are also called the secondary pores. The tortuosity i.e the ratio of average path of gas flow in free space to the length of that in the catalyst layer, plays an important

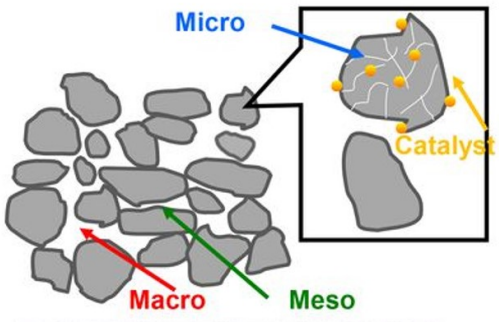

Figure 2.14: Electrode showing macropores, mesopores and micropores.

role in the mass transport. According to Suzuki et al. [49] a porosity of 40% with a tortuosity of 1.1 is necessary for a 11 µm thick catalyst. Except the gas flows, mesoporous and macroporous structures help in expelling water produced from the cell avoiding the issues related to flooding in the cathode.

Figure 2.14 represents an electrode showing these pores. All type of porosities play an important role in fuel cell performances. A hierarchical approach of macropores, mesopores and micropores has also been tried with limited success [50].

Electrode ionic and electric conductivity

High electrical conductivity is a basic requirement for support materials because a conductive support can provide a good pathway for the transport of electrons between the support and either Pt or Pt-alloy nanocatalysts, which is favorable for PEM fuel cell operation. The support should have high electrical conductivity to have a minimum ohmic loss. For proton conductivity, different ionomers have been tested, but till date, no other ionomer suitable for fuel cell application was found to have a better proton conductivity than Nafion. Nafion ionomer has a bulk conductivity of 0.1 S cm^{-1}. In general, the electrodes have a resistance greater or equal to 0.1 S cm^{-1}.

Electrical conductivity, specific surface area and porosity of some common support material are shown in Table 2.4.

MEA fabrication

The performance of the fuel cell depends finally on how the MEA is fabricated. The fabrication technique used ensures the efficient transport of protons, electrons and materials to and from the catalyst. MEA fabrication determines the secondary porosity in the electrode.

Table 2.4: Some of the important properties of support materials [14, 51].

Support material	**Surface area ($m^2\ g^{-1}$)**	**Porosity**	**Electrical conductivity ($S\ cm^{-1}$)**
Vulcan XC 72	254	Microporous	4.0
Carbon gels	400-900	Mesoporous	≥ 1
Multiwalled carbon nanotube	200-400	Mesoporous	0.3-3 (depends on functionalization)
Carbon nanofiber	10-300	Microporous	100-10^4
Doped TiO_2	1.4 -136	Microporous	0.1-100

The fabrication also determines the triple phase boundary (TPB) density and the performance of the cell. In this regard, research on the electrode structure has gained momentum and investigators have developed many methods to prepare MEAs.

The general and most commonly applied method for preparation of MEAs was developed by Wilson [6, 7] which was modified later. An ink is formed from catalyst, ionomers and solvent consisting of water and isopropanol, and airbrushed onto the heated membrane.

The three most common types of membrane fabrication involve:

- Catalyst coated membrane (CCM): The catalyst ink is sprayed or brushed on the membrane
- Catalyst coated gas diffusion layer (CCGDL): The catalyst ink is sprayed or brushed on the GDL
- Decal process: The catalyst ink is sprayed or brushed on a transferring film and peeled off the transfer layer

Figure 2.15 shows the general steps in MEA preparation.

In all the three methods, the general idea remains the same wherein an ink is prepared and transferred to form a thin layer of the catalyst. In these techniques, however, the latter structure of the layer is already formed within the ink by the agglomeration of the particles and the ionomer. The control of the electrode structure is not easy as the dispersion medium governs the ink's properties like viscosity, dispersion and aggregation size of the catalyst/ionomer particles, rate of solidification and ultimately the physical and mass transport properties of the catalyst layer.

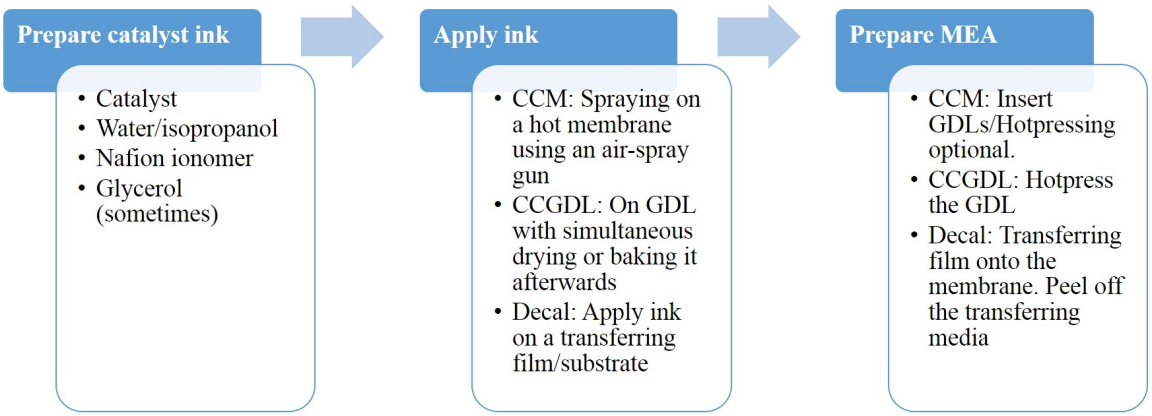

Figure 2.15: General steps of MEA preparation

Researchers have also come up with various new techniques such as plasma sputtering [9], ion beam bombardment [10], electrodeposition [11], electrospray [12], inkjet printing [13] etc., for increasing the fuel cell performance and durability. Some of the methods, even though effective, are either too expensive to prepare in large scale or physically not possible to scale up.

In this thesis, a new method of fabrication of MEA is discussed using the inexpensive, scalable technique of electrospinning. The versatile properties of the technique give excellent control on porosity, thereby facilitating transport of reactants and products. The technique of electrospinning is described in the following section.

2.5 Electrode stability aspects

In the electrode, both the catalyst and the catalyst-support undergo degradation. Several studies have observed the growth of Pt particles as well as their dissolution. Experiments on Pt thin films and nanosized Pt on carbon have shown that at 80 °C above 0.85 V versus RHE Pt dissolution is seen to occur [52]. The dissolution is maximum at 1.15 V as shown in Figure 2.16. This was ascribed to formation of an oxide layer and subsequent chemical dissolution.

$$\mathrm{Pt} + \mathrm{H_2O} \rightarrow \mathrm{PtO} + 2\,\mathrm{H^+} + 2\,\mathrm{e^-} \quad \mathrm{E_0} = 0.98\ \mathrm{V_{SHE}} \tag{2.20}$$

$$\mathrm{PtO} + 2\,\mathrm{H^+} \rightarrow \mathrm{Pt^{2+}} + \mathrm{H_2O} \tag{2.21}$$

Pt oxide formation is also seen in fast potential cycling, resulting in formation of what is called β-oxides, reduction of these oxides are accompanied by dissolution of Pt and formation of Pt ions. These Pt ions have the potential to replace H^+ in the membrane.

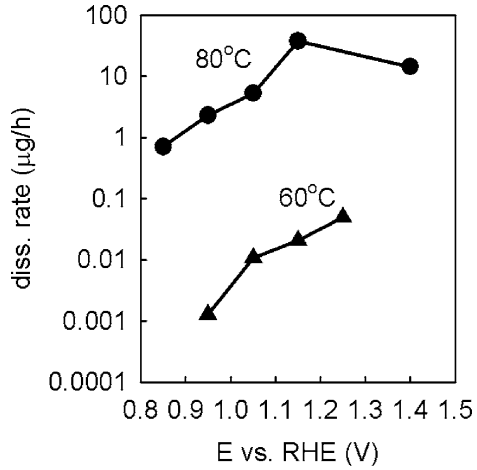

Figure 2.16: Pt dissolution rate vs. dissolution potential and temperature. Reproduced from [52].

There has also been debate on particle growth associated with coalescence. Brownian motion causes surface diffusion of particles with random collisions leading to coalescence. Also, this process is a natural tendency of particles to coagulate and decrease the surface energy which cannot be avoided via so-called Ostwald ripening process. However, many recent studies have suggested that Ostwald ripening under operating conditions is slow and should not be significant for 10,000 hours of operation [21, 53, 54].

Degradation associated with the support material (generally carbon is used) is found to be more severe than the catalyst. Carbon is thermodynamically unstable and undergoes corrosion in presence of humidity as given below:

$$\mathrm{C} + 2\,\mathrm{H_2O} \;\rightarrow\; \mathrm{CO_2} + 4\mathrm{H^+} + 4\mathrm{e^-} \quad E \;=\; 0.207\;V_{SHE} \tag{2.22}$$

Due to slow kinetics, carbon can still be used as support material. However, Pt seems to accelerate its corrosion [55]. It was also found that carbon corrosion of the cathode catalyst layer increases with increasing potential and increasing humidity [56].

Many degradation models on catalyst corrosion exist, however, it is generally accepted that as carbon starts corroding, Pt particles tend to agglomerate. When Pt particles become larger, they disconnect from the membrane electrode assembly as shown in Figure 2.17.

The carbon can also become partially oxidized to oxygenated surface carbon species like quinone-hydroquinone, due to which the conductivity at the contact between carbon support and catalyst nanoparticles may decrease. Also, the presence of surface oxides may weaken the platinum-support interaction, leading to lower resistance against surface migration of Pt particles [58]. The anode catalyst could also be exposed to much more oxidative conditions than the cathode during cell voltage reversal caused by fuel starvation [59]. If hydrogen is

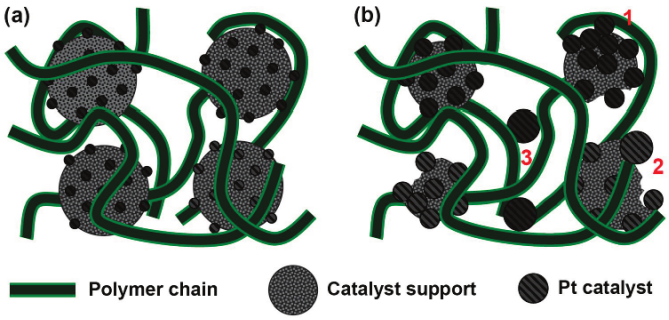

Figure 2.17: Schematic representation of the effect of carbon corrosion on (1) agglomeration, (2) coalescence and (3) loss of Pt particles in the membrane electrode assembly (MEA) during operation of PEM fuel cells: (a) Normal (corrosion-resistant) electrode and (b) corroded electrode. Reproduced from [57].

no longer available to be oxidized, the anode potential which can go up to 1.4 V, resulting in either oxidation of carbon or electrolysis of water at the anode according to equation shown.

$$\mathrm{C} + 2\,\mathrm{H_2O} \rightarrow \mathrm{CO_2} + 4\,\mathrm{H^+} + 4\,\mathrm{e^-} \tag{2.23}$$

$$2\,\mathrm{H_2O} \rightarrow \mathrm{O_2} + 4\,\mathrm{H^+} + 4\,\mathrm{e^-} \tag{2.24}$$

Summarizing, high-surface-area carbon supports in PEM fuel cell electrodes are susceptible to corrosive conditions, which include high water content, low pH, high temperature, high potential, high oxygen concentration and the presence of Pt particles itself.

Many approaches are dedicated to improve the stability of the carbon black, for instance by increasing their degree of graphitization. For example, Makharia et al. [60] studied the stability of Pt/Vulcan and Pt/Graphitized-Vulcan and found that the activity of Pt/Vulcan was 50% less than Pt/Graphitized-Vulcan after 2500 potential cycles. Alternative carbon materials like multiwalled carbon nanotubes (MWCNTs), carbon nanofibers [61], ordered mesoporous carbons (OMCs) [51] etc., have shown to have better stability. For example, Park et al [62] studied the electrochemical behaviour of two different electrocatalysts (Pt/MWCNTs and Pt/Vulcan XC-72) under accelerated stress tests at 1.2 V and found that the Pt/MWCNT had a smaller decrease in electrochemical surface area and a slight increase in their interfacial charge transfer resistance, suggesting that MW-CNTs exhibit good corrosion resistance and a strong bonding with Pt nanoparticles. Thermally stable boron doped diamonds have also shown promising results as stable catalyst material [63].

Another approach that is followed is the application of non-carbon, inert supports. Conducting ceramic oxides like TiO_2 [57], WO_x[64], SnO_2 [65] offer promising properties due to their high chemical stability and strong interaction with Pt (co-catalytic effect). At

the same time, the low price and the abundance of metal oxides can help reduce the cost of the fuel cell. On the downside, their electrical conductivity is low, even metal-doping is not sufficient in many cases.

Polymers due to their high surface area and proton conducting ability act as a catalytic support. Conducting polymers (CPs) such as polyaniline, polypyrrole, polythiophene and their derivatives, fulfill the requirements of a suitable fuel cell catalyst support. For PAni supported catalysts, in addition to an increase in metal surface area, an enhancement in catalytic activity was seen which was ascribed to a synergy between metal and the polymer matrix [15].

Unfortunately, neither ceramic materials, nor polymers provide sufficient electrical conductivity. New systems of hybrid catalyst supports of carbon-ceramic, carbon-polymer, and ceramic-polymer are being studied to latch the benefits of both worlds. For example, the hybridization of polymer and carbon should provide high electron conductivity, high surface area, proton conductivity [66]. Figure 2.18 shows the main characteristics of pure support materials, hybridization of the support material can provide.

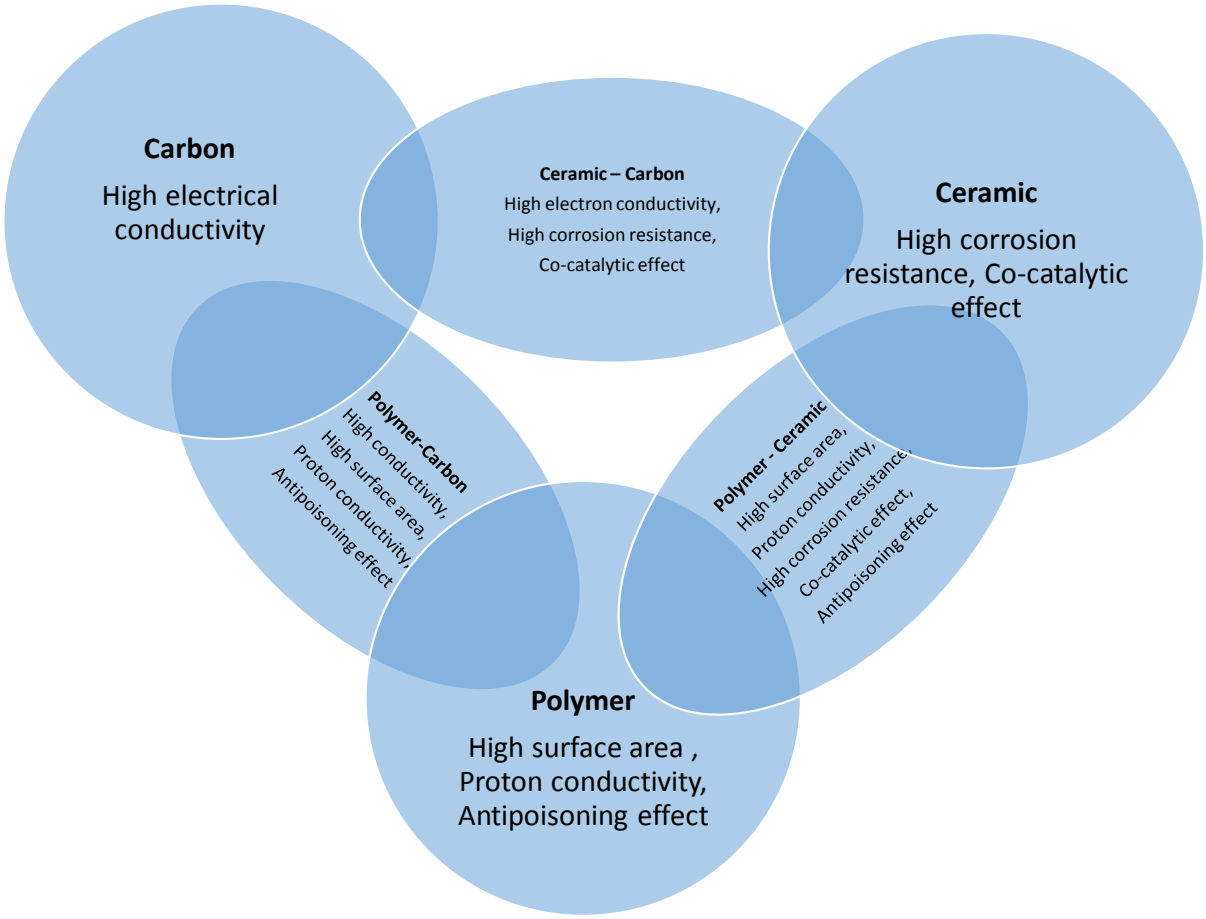

Figure 2.18: Scheme showing the main characteristics of pure and hybrid support materials [66].

2.6 Electrospinning

In this work, the two challenges of the fuel cell electrodes i.e cost and durability, are addressed using the technique of electrospinning.

Electrospinning is a method to prepare highly porous fiber networks whose fiber diameters can be anywhere from 2 nm to 2000 nm. The versatility of electrospun materials not only depends on the precursor, but also on modifying the solution and process parameters, giving a great control over the morphology [67]. Figure. 2.19 shows a representation of the electrospinning technique. A polymer solution of the required electrospinnable polymer is prepared and passed through a small needle tip. At the needle tip, a potential between 5 - 30 kV is applied with respect to the collector plate. At this potential, the electrostatic repulsion is sufficient for surface tension to break, forming what is called a Taylor cone. Due to molecular cohesion forces, the stream does not break up, forming a continuous jet. The solvent vaporizes along the path leaving behind the polymer fiber.

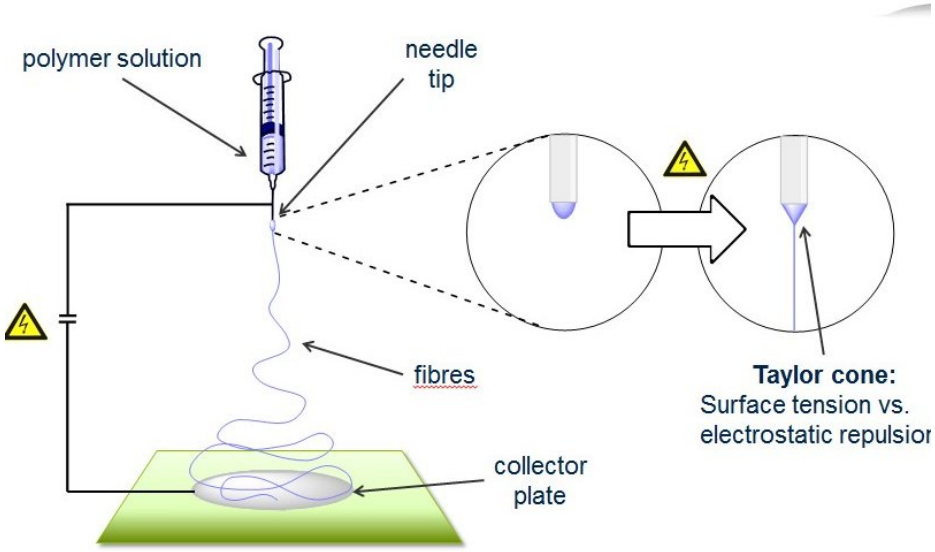

Figure 2.19: Representation of electrospinning technique.

A great number of parameters affect the electrospinning process. Many of the parameters are, however, inter-dependent and cannot be separated as such. For example, a change in molecular weight changes the viscosity and surface tension of the solution resulting in change of the electrospinning characteristics. With this in mind, the factors affecting the electrospinning process can be summarized as below:

1. **Electrospinning solution**

- **Polymer properties**

  Molecular Weight: As molecular weight of the polymer increases, reduction in the number of beads and droplets is seen. But at very high molecular weights, the fibers can become entangled and this may result in formation of micro-ribbons [68].

  Molecular Entanglement: The polymer used to prepare the electrospinning solution should not only have suitable molecular weight but also sufficient entanglement. For example, owing to insufficient entaglement, it is not possible to electrospin Nafion alone [69]. Fiber formation occurs when there are more than 2.5 entanglements per chain [70].

- **Solution properties**

  Concentration: As the concentration of the polymer decreases, fiber diameters decrease till the jet becomes unstable resulting in formation of beads. Researchers have found out that a power law relationship can exist between the fiber diameter and concentration of polymer.

  Viscosity: At low viscosity there will not be uniform flow and formation of beads can take place. At higher viscosity there would be difficulty in ejection of jets. The range of viscosity that can be used differs from polymer to polymer, but as a starting point viscosity of 1 to 20 poise is suitable.

  Conductivity: Conductivity of the electrospinning solution results in stretching of the stream which results in thinning of the fibers. However, very high conductivity can result in formation of unstable jets and in extreme cases short-circuiting of the terminals (collector and the needle) is also possible.

  Surface tension: The electrostatic force required to electrospin is influenced by surface tension. The potential required for breaking the droplet increases. However, there is no change in fiber size observed with change in surface tension.

- **Effect of additives**

  Soluble salts, active materials, surfactants etc. can also be added to the electrospinning solution. The effect can be significant. For example, a small amount of salt or carbon can increase the conductivity of the solution which can significantly decrease the fiber size. Addition of surfactant, decreases the surface tension making it easier to electrospin.

2. **Process conditions**

   - **Electric potential applied**
     A minimum critical voltage needs to be applied to form the Taylor's cone and start electrospinning process. The voltage (Vc) can be calculated as shown in the equation below:

$$V_c^2 = 4\frac{H^2}{L^2}\left(ln\frac{2L}{R} - \frac{3}{2}\right)0.117\pi\gamma R \tag{2.25}$$

     where H is the separation distance between the needle and the collector, L is the length of the needle (or capillary), R is the radius of the needle and γ is the surface tension of the solution [71].

     Above this voltage, there is a decrease in fiber diameter with increase in voltage. In some cases, there can be an increase in the rate of electrospinning or spitting of the electrospinning solution.

   - **Flow rate**
     There can be a decrease in fiber diameter with decrease in flow rate, generation of beads with too high flow rate.

   - **Needle gauge**
     The bigger the needle diameter, the larger is the fiber size.

   - **Distance between the needle and collector**
     The horizontal spread of materials increases with increase in distance. Smaller distance may result in generation of beads.

   - **Motion and size of target screen (collector)**
     Semi-aligned electrospun fibers can be prepared by horizontal electrospinning and also using of rotating drums. Porosity of the fibers can be increased by moving the drum sideways.

3. **Ambient parameters**
   Temperature of electrospinning, humidity and air velocity in the chamber affect the electrospinning process.

2.6.1 Application of electrospun materials

Electrospinning is widely used in bio-medical applications. For engineering the living tissues, a biodegradable scaffold is generally considered as an indispensable element. Electrospinning is used to create nanofibrous scaffolds which act as a template for tissue engineering [72]. The electrospinning materials also meet the requirements outlined for a wound healing

polymer. As electrospun electrodes have a high surface area, fast dissolution of solvent takes place making it suitable for controlled drug delivery. The nanofibers can also easily trap particles of sizes between 1 μm to 5 μm via physical entrapment and electrokinetic capture, and hence have been extensively used in filtration. Electrospun materials are also used in the manufacturing of protective clothing, cosmetics etc.

In the area of energy, electrospinning has been currently applied for various applications [73]. The 1-D nanostructure materials for dye sensitized solar cells using electrospinning is reported to have a better electrical conductivity and allow rapid collection of charge carriers generated throughout the device [74]. The large porosity and high surface area anchor the maximum amount of dye sensitizers. In lithium ion batteries, electrospinning is used extensively to fabricate anodes, cathodes, and separator materials [75]. Electrospinning has also found application in flow batteries [76] and in superconductors [75, 77].

2.6.2 Electrospinning and fuel cells

In fuel cell research, electrospinning has been used to improve the properties of catalysts, electrodes and membranes.

With respect to the membrane, in the literature two approaches have been used. The first involves electrospinning a non-conductive or less conductive polymer into a porous matrix, which has mechanical or barrier properties and the pores are filled with a high proton conducting component. As an example, Mollá and Compañ [78] prepared Nafion/PVA membranes to decrease the methanol crossover in DMFCs. In the second approach, a high proton conducting matrix is electrospun into a porous fibre mat and then reinforced with a secondary polymer to provide mechanical stability. For example, Choi. et al. [79] prepared polymer/particle composite and electrospun to fabricate membranes with enhanced properties. The nanofibers are composed of a proton conducting polymer with proton conducting, water-retaining inorganic nanoparticles which would allow more water retention and provide better mechanical strength.

The preparation of electrospun catalysts for fuel cell applications is limited by the inability to prepare catalysts below 5 nm, which is often used in fuel cells. Nonetheless, some work has been carried out in this regard. Kim et al. [80] synthesized catalytic electrospun nanowires (NWs) of Pt/Rh and PtRu with 50 nm diameter and found that the mass activity for methanol oxidation of PtRu NWs was better than the conventional catalyst of highly dispersed PtRu NPs on carbon. Shui and Li [81] described the fabrication of centimeter-long nanowires of Pt by electrospinning, with the ultimate goal of removing the need for a catalyst support in the fuel cell electrode.

In case of non-precious metal catalysts, electrospinning is being successfully applied. Zamani et al. [82] prepared electrospun ironpolyanilinepolyacrylonitrile derived nanofibers which demonstrated high performance for oxygen reduction reaction. Shui et al. [83] were able to prepare highly efficient non-precious metal catalysts with metal-organic frameworks in a continuous carbon nanofibrous network. They were able to obtain high volumetric activities of 3.3 A cm^{-3} at 0.9 V.

The electrospinning approach is more suited for preparing continuous catalyst support material. Carbon nanofibres, derived from electrospun polyacrylonitrile (CNFs) represent a promising support material for fuel cells as CNFs have increased conductivity over carbon particles. This is due to easier electron transfer along the aligned CNF, in contrast to carbon particles where there are significant interfaces between the particles, which may add to the resistance of the system. Park et al. [84] prepared electrospun PAN-based carbon nanofibres which have high surface area, shallow pores and rough surfaces leading to significantly higher Pt utilization (69%) in the Pt/CNF than Pt/Vulcan XC-72R (35%). The electrical conductivity of the electrospun CNFs carbonized at 1000 °C was also higher at 9.9 S cm^{-1}, whereas the conductivity of Vulcan XC-72R was 4.5 S cm^{-1} which led to improved fuel cell performance of the electrospun electrode.

Jones group prepared novel complex loose-tube (fiber-in-tube) electrospun Nb-SnO_2 [85] and TiO_2 fibers [86] which they found to be highly stable with decent performance. Li et al. [87] prepared electrospun CNF mats as supports and then studied them for methanol oxidation. These exhibit high exchange current densities and a low charge transfer resistance.

With respect to the electrode structuring, Pintauro and co-workers [88, 89] have carried out pioneer work, wherein they electrospun polyacrylic acid (PAA) containing commercial catalyst and Nafion to obtain high performance electrodes. Electrospinning inks were prepared by mixing HiSpec 4000 Pt/C catalyst, Nafion ionomer, and poly acrylic acid 450 kDa in a ratio of 6:2:1 in a water/isopropanol solvent. Electrospinning of electrically conducting catalyst and proton conducting polymer increased the triple phase boundary density which resulted in enhanced performance. This resulted in maximum power density of 437 mW cm^{-2} for a H_2/air fuel cell operation at 80 °C and ambient pressure for a nanofiber cathode at 0.065 mg_{Pt} cm^{-2} loading. They also found the stability of the electrodes to be significantly higher than the electrodes prepared from the same catalyst by conventional methods [90].

2.6.3 Electrospraying

Electrospraying is a modified version of electrospinning, wherein no polymer is added. In the absence of any polymer, when an electrical potential difference is imposed between the

needle and the collector, the suspension pumped through the needle breaks up in a spray of charged tiny droplets to get a highly porous deposit. This technique is also used in fuel cells electrode in preparation of low loading electrodes. For example, Martin et al. [91] prepared an electrospraying ink containing Pt/C, Nafion and ethanol and electrosprayed on GDL and tested as fuel cell cathodes and found that a reduction of platinum content by a factor of four only reduces the performance by a factor two. A simultaneous electrospinning/electrospraying have been attempted with which Pt loading was further lowered to 0.022 mg_{Pt} cm^{-2} with modest reduction in power density (≈66-78%) [92].

Chapter 3

Materials and Methods

This chapter lists all the materials used, and the characterization techniques that have been carried out while synthesizing and studying the catalysts and electrodes for the experiments. The instrumentation and theoretical background of the analytical techniques used for various physical and electrochemical characterization in this work are discussed as well.

3.1 Materials

Table 3.1 shows the list of chemicals used for carrying out the experiments. Besides these, the deionized water (18.2 MΩ) was obtained using Milipore system.

Table 3.1: Lists of various materials and chemicals used in the experimental work.

Chemical Reagents	Company/Supplier
Binder	
Nafion 5 wt.%	Ion Power
Membrane	
Nafion 212	Ion Power
Catalyst and Metal Precursor	
hexachloroplatinic acid $(H_2PtCl_6) \cdot 6\,H_2O$	Sigma Aldrich
Polyacrylonitrile $(C_3H_3N)_n$, Mw ∼150,000	Sigma Aldrich
Polyacrylic acid $(C_3H_4O_2)_n$, Mw ∼450,000	Sigma Aldrich
Titania (TIO_2) (P25)	Aeroxide
20 wt.% Pt/C (Hispec 3000)	Alfa Aesar
Chemicals	
Sulfuric acid (96%)	Roth
Nitric Acid (65%)	Grusig
DMF (99.5%)	Acros Organics
Ethylene glycol	Merck
Isopropanol (99.8%)	Roth
Perchloric acid (70.%)	Aldrich
Miscellaneous	
Hydrogen gas (99.9999%)	Air Liquide
Nitrogen gas (99.8%)	Air Liquide
Oxygen gas (99.5%)	Air Liquide
Vulcan Carbon	Cabot Corporation
Multi-walled carbon nanotubes (6-9 nm 5 μm)	Sigma Aldrich
Gas diffusion layer (28BC)	Sigracet

3.2 Physical characterization techniques

In the following section, the instrumentation and brief description of X-ray diffraction method (XRD), scanning electron microscopy (SEM), transmission electron microscopy (TEM), Raman spectroscopy and thermogravimetric analysis (TGA) are given which have been used in the later chapters.

3.2.1 X-Ray diffraction

X-ray powder diffraction (XRD) is carried out to identify phases and to calculate particle sizes (for particles below 1 μm) of a crystalline material. It can also provide information on unit cell dimensions. Here, it is mostly used to characterize deposited Pt particles.

X-ray diffraction is based on constructive interference of monochromatic X-rays and a crystalline sample. X-rays of known wavelength, (in this case, Copper (Cu) x-ray tubes having (K_α = 1.54 Å)) are generated by striking a pure anode of a particular metal with high-energy electrons in a sealed vacuum tube. These x-rays are monochromated to separate $K_{\alpha1}$ and $K_{\alpha2}$, collimated to concentrate, and directed toward the sample. The interaction of the incident rays with the sample produces constructive interference (and a diffracted ray) when conditions satisfy Bragg's Law :

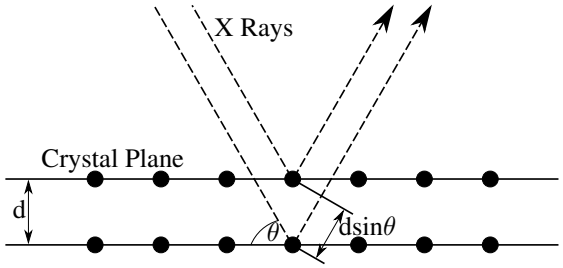

Figure 3.1: Diagram representing Bragg's Law

$$n\lambda = 2dsin\theta \tag{3.1}$$

where, n is an integer, λ is the wavelength of the x-rays, d is the interplanar spacing generating the diffraction and θ is the diffraction angle.

These diffracted X-rays are then detected, processed and counted. The samples are scanned through a range of 2θ angles (between 20° - 90° 2θ), to attain all possible diffraction directions of the lattice. Conversion of the diffraction peaks to d-spacings allows identification of the crystal because each crystal has a set of unique d-spacings, which is compared with standard reference patterns provided by the International Center for Diffraction Data (ICDD).

The XRD data was refined using Rietveld refinement using Fullprof software. The Rietveld method uses a least squares approach to refine a theoretical line profile until it

matches the measured profile. This refinement helps deal reliably with strongly overlapping reflections [93].

Scherrer equation [94, 95] gives a method to determine the crystal size of the particle.

$$\tau = \frac{K\lambda}{\beta \cos\theta} \tag{3.2}$$

where K is the shape factor, λ is the x-ray wavelength, β is the line broadening at half the maximum intensity (FWHM) in radians, and θ is the Bragg angle. τ gives the mean size of the crystal, which may be smaller or equal to the grain size. The refined reflections were calculated for particle size using the Y, parameter in Fullprof.

For XRD analysis, the powder to be analyzed is first dried, ground and a small amount placed between two acetate films. An adhesive consisting of 9: 1 collodium, amyl acetate is used to attach the samples together. The sample is then attached to a rotating support, which provides a better statistical distribution of the particles during the measurement. The XRD patterns were recorded in transmission geometry, using a STOE STADI P, operating with Cu $K_{\alpha 1}$ radiation. The XRD reflections were measured between 20° (2θ) - 90° (2θ).

3.2.2 Scanning electron microscopy

Scanning electron microscopy (SEM) is used to study the surface topography of a sample with areas ranging upto 5 microns in width (resolution $\approx$ 1 nm). It is used to study the shape, size and texture of the particles. Also, its possible to obtain qualitatively or semi-quantitatively chemical compositions of the prepared samples using energy-dispersive X-ray spectroscopy (EDX) attached to it.

The samples were analyzed by using a high-resolution scanning electron microscope (SEM, HITACHI UHR FE-SEM SU8030), operating between 5-20 kV acceleration voltage. The scanning electron microscope (SEM) uses a focused beam of high-energy electrons on the samples to produce electron sample interactions. The samples to be examined are first dried in a drying oven at 80 °C for 30 minutes. These are then cut to a suitable size of usually 0.5 x 0.5 cm and inserted into the device by means of a multiple sample holder. Most of the images are produced from the secondary electrons with different magnifications. In some cases, to get an insight of metal distribution, signals obtained from back scattered electrons are also used to collect the images.

The images were recorded at different magnifications and were analysed using ImageJ software with diameterJ plugin. DiameterJ is a validated technique for calculating diameters

of the fibers [96]. For diameter J analysis, a SEM image of suitable magnification is selected (Figure 3.2a). Using the technique of statistical region merging [97], the SEM image was segmented and the layers were separated (3.2b top left). The fibers are thinned to calculate the number of intersections (3.2b top right), and their distances were mapped (3.2b bottom left). The areal porosity was calculated using mesh-hole analysis (3.2b bottom right). Using this technique, the histogram of fiber radius analysis (3.2c) and the histogram of the areal void is calculated (3.2d).

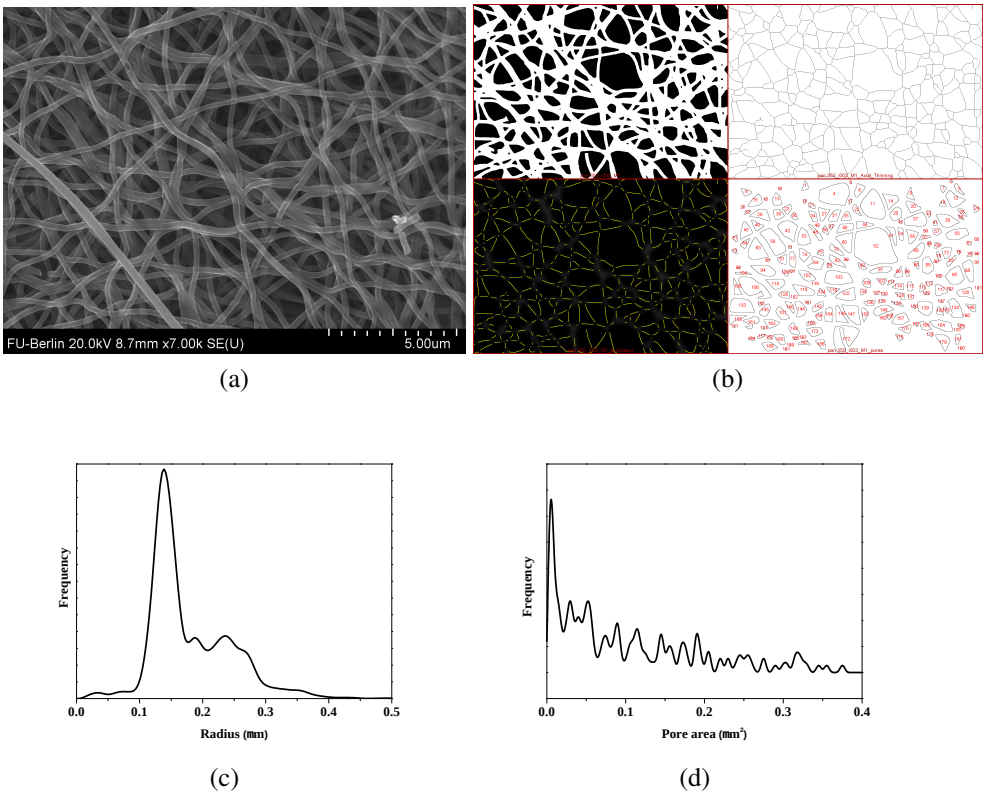

Figure 3.2: Overview of DiameterJ analysis flow (a) SEM image (b) image processing (c) histogram of radius (d) histogram of pore area.

3.2.3 Transmission electron microscopy

Transmission electron microscopy (TEM) is capable of higher magnifications than SEM, and it is used to study the size, shape and arrangement of the particles in atomic scales. Here, unlike SEM, electrons transmit through a very thin layer of sample, resolving the image further. Maximum theoretical resolution d can be given by

$$d = \frac{\lambda}{2NA} \tag{3.3}$$

where, λ is the wavelength of the electron after correcting for relativistic effect and NA is the numerical aperture of the system.

Analysis of the samples was carried out using transmission electron microscope (TEM) FEI Tecnai G^2 20 S-TWIN with an acceleration voltage of 200 kV produced by a LaB_6 cathode filament. The electron beam is focused on a thin specimen (less than 200 nm) by means of the condenser lens system, and it penetrates the sample thickness either undeflected or deflected to produce the image. For preparation of the thin specimen for TEM measurements, a very small amount of catalyst powder was ultrasonicated in isopropanol. A drop of this dispersion was applied to a fine copper grid with carbon film and was allowed to dry. In case of electrospun fibres, a thin batch of the fibre strands was pricked and placed on the copper grid to view the sample.

3.2.4 Raman spectroscopy

Raman spectrum analysis was carried out on the carbon fibers to understand their degree of graphitization. Raman spectroscopy is based on the inelastic scattering of the monochromatic light and is sensitive to the symmetric covalent bonds with little or no natural dipole moment which makes it ideal to study the carbon-carbon bonds. Raman spectroscopy gives an understanding of degree of graphitization in a carbon sample with the presence of purely graphitic G band and disordered D bands in the spectra. Raman spectra were recorded by using an Evolution Raman spectrometer (Horiba). For the purpose of analysing the black carbon sample, a 532 nm laser torus from Laser Quantum was used. The Rayleigh scattering component was removed by a Notch filter. A gray filter was used to reduce the intensity of the laser beam exposed on to the sample, in order to avoid the high energy-flux that could heat the sample. A thin layer of the sample of about one millimeter thickness was pressed with a steel spatula onto a glass slide and placed on the microscope sample holder. Deconvolution of the obtained spectra consisting of stokes and anti-stokes regions were carried out using PeakFit program.

3.2.5 Thermogravimetric analysis

Thermogravimetric analysis (TGA) of the Pt/C catalysts was carried out in air to get an accurate loading of Pt as carbon burns in air leaving no residue. In TGA, change in mass is measured with change in temperature which in this case is due to oxidation of carbon. The rate of weight loss can give an understanding of corrosion rate. TGA was carried out using Netzsch STA429 using synthetic air at 75 ml min^{-1} and temperature ramped at 5 K min^{-1} from 22 °C to 1000 °C. Between 5 mg to 20 mg of the sample was dried in an oven and later transferred to a ceramic sample holder for analysis.

3.2.6 Fourier transform infrared spectroscopy

Fourier transform infrared spectroscopy (FTIR) is a technique which is used to obtain an infrared spectrum of absorption (mostly) or emission of a solid, liquid or gas. Infrared radiation (IR) can interact with a molecule resulting in molecular vibrations and molecular rotations. When the applied infrared frequency matches the natural frequency of vibration of the molecule/functional group, due to the adsorption of the radiation, a peak is observed. Different functional groups absorb characteristic frequencies of IR radiation. Therefore, IR spectrum of a chemical substance is a fingerprint of a molecule for its identification. FTIR, therefore can be used to identify different organic entities present in the polymer or unknown compound. In this work, FTIR was used to identify any possible interactions between Nafion and polyacrylic acid.

For the sample preparation, a small amount of the compound to be analyzed was taken and was mixed with KBr powder. The product was pressed using a hydrothermal press to form a pellet and was placed in the sample holder. For KBr background correction, a pellet with pure KBr was also prepared.

IR measurements were carried out using Bruker Vertex 70 with a range between 4000-400 wavenumber (cm^{-1}) with a spectral resolution of 2 cm^{-1}. The obtained spectrum was background corrected and analyzed using Bruker OPUS 7.2 software.

3.3 Electrochemical characterization

Cyclic voltammetry was one of the main electrochemical techniques used to characterize the samples. It can be carried out in a liquid electrochemical cell, but also in-situ in the fuel cell test bench.

3.3.1 Cyclic voltammetry

Cyclic voltammetry (CV) is a potentiodynamic electrochemical measurement technique. It is used to carry out half cell studies, to see catalyst activity, to find out the onset potential, and to determine the electrochemical active surface area (ECSA).

A typical cyclic voltammogram of a platinum electrode in an aqueous, basic electrolyte is shown in Figure 3.3 . The cyclic voltammogram is typically divided into three regions : the region of hydrogen adsorption or desorption at low potentials, the region of the double layer capacitance at intermediate potentials and the region of oxygen adsorption or desorption at

high potentials. The area under the curve in the hydrogen region (shaded area in Figure 3.3) refers to the catalytically active surface with supported Pt nanoparticles, it corresponds to the Q_{Pt} charge necessary for releasing the adsorbed hydrogen atoms. (The current corresponding to double - layer current should be subtracted out). The ECSA can be calculated using Equation 3.4, where L is the Pt loading used and Γ_{Pt} is the charge correspond to that needed to oxidize a monolayer of H_2 on platinum which is taken as 210 μC cm^{-2}.

$$ECSA\ (m^2_{Pt}/g_{Pt}) = \frac{Q_{Pt}}{\Gamma_{Pt} L} \tag{3.4}$$

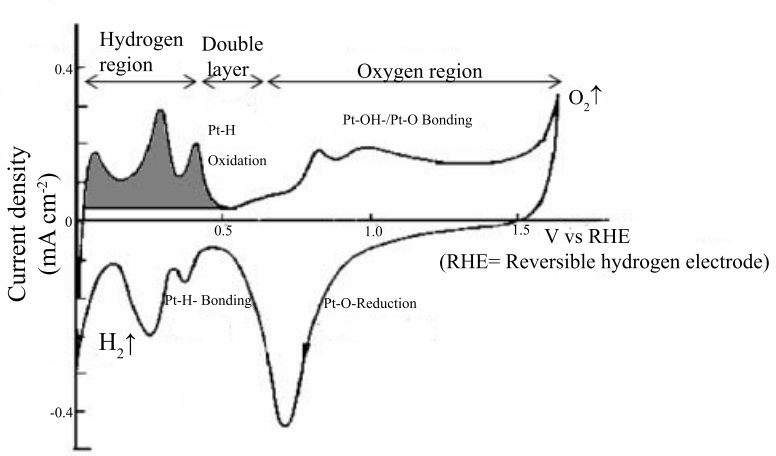

Figure 3.3: Cyclic voltammogram of poly-crystalline Pt in 1 N KOH at 20°C, in a N_2 atmosphere, scan rate: 100 mV s^{-1}, the gray-shaded area represents the amount of hydrogen desorbed.

The measurements were performed in a three-electrode configuration using Reference-600™ or Reference-3000™ from the Gamry Instuments Inc in an electrochemical cell as shown in Figure 3.4. Working electrode consisted of a very small amount of catalyst (ink preparation differed with samples, and mentioned there in) on the glassy carbon electrode. Counter electrode consisted of platinum wire and as reference electrode, either silver chloride electrode or saturated calomel electrode, whose potentials were periodically checked, was used. 0.1 M $HClO_4$ was used as electrolyte, which was purged with N_2 for several minutes to displace dissolved oxygen molecules from the electrolyte, which can affect the measurement. All electrochemical measurements are reported against the standard hydrogen electrode (SHE) potential.

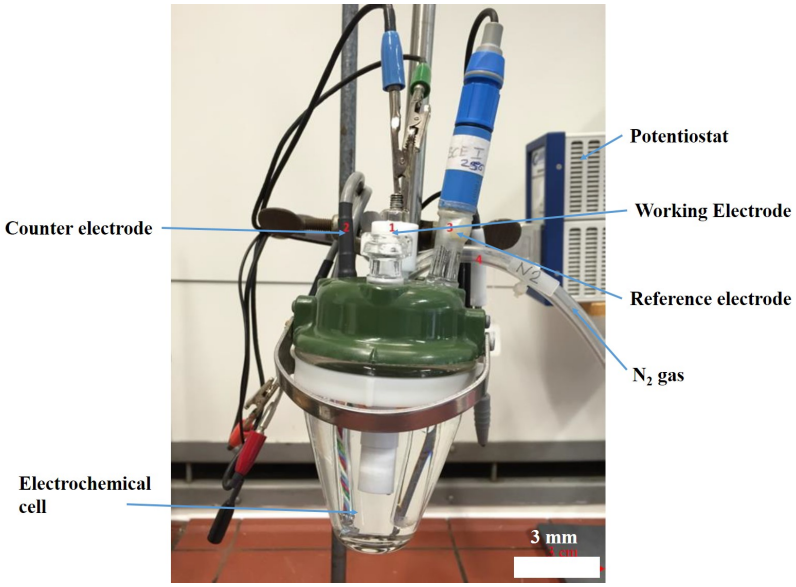

Figure 3.4: Picture of an electrochemical cell showing different parts.

3.3.2 Ex-situ potential cycling

Potential cycling plays an important role in the characterization of the support. Initial cycling oxidizes the organic impurities attached to the catalyst. Potential cycling for a longer duration is helpful in studying the stability of the catalyst. The potential cycling was carried out at a scan rate of 50 mV s^{-1} between 0.05 V to 1 V (vs. SHE). The first ECSA reported is from the cyclic voltammogram obtained after 20 cycles of activation. For the purpose of stability study, the catalysts were cycled for 1000 cycles.

3.4 Fuel cell testing

Fuel cell polarization curves were measured using a Scribner Series 850e test station with both anode and cathode humidification, and manual back-pressure control. The setup is shown in Figure 3.5a. The cells used in this system are made to harbour a 3.3 cm diameter round membrane-electrode-assembly (Figure 3.5b). The serpentine flow channels were used for both anode and cathode to fit the cell as shown in Figure 3.5c. Experiments in H_2/O_2 setups were performed at different temperatures from room temperature to 80 °C with fully humidified gases at a range of pressures from atmospheric (ambient) pressure to 100 kPa atmospheres with flow rates 125 sccm H_2/ 100 sccm O_2. The MEAs were activated by holding the potential at 0.6 V overnight and gradually increasing the temperature to 80 °C until steady power output from the MEAs was achieved. Polarization curves were generated by collecting the current at a given voltage after waiting 60-120 seconds for the system to stabilize by taking values linearly or logarithmically.

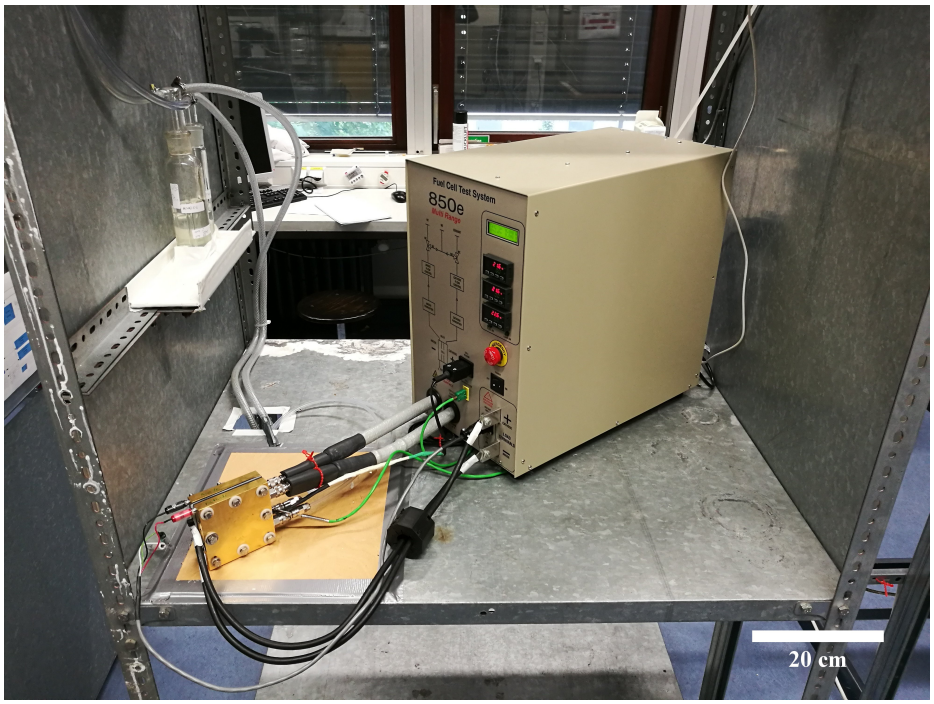

(a)

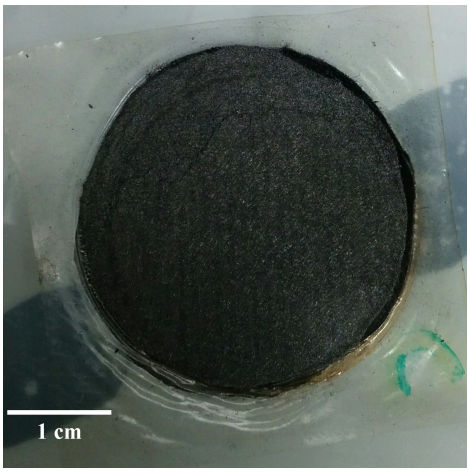

(b)

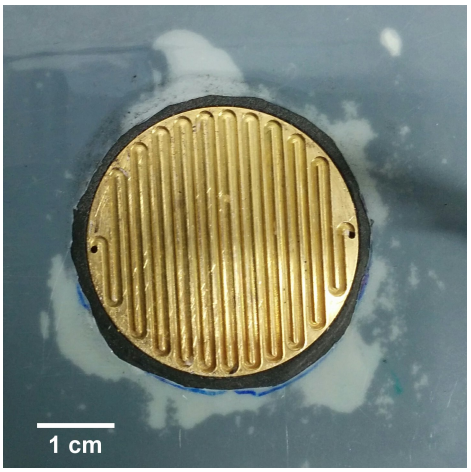

(c)

Figure 3.5: Photographs of (a) fuel cell setup (Scribner 850e) (b) MEA (c) current collector containing flow fields.

3.4.1 In-situ cyclic voltammetry and accelerated aging studies

In-situ CV measurements were performed on the round 8.7 cm^2 MEAs at 50 mV s^{-1} between 0.05 V to 1 V , where a H_2-purged anode served as both the counter and reference electrodes and the N_2-fed cathode was the working electrode. The fuel cell fixture was operated at room temperature with fully humidified gas streams.

Potential cycling test was performed to accelerate the degradation of support (mainly carbon) as a durability evaluation of catalyst material used in MEAs. The test method is based on a Fuel Cell Commercialization Conference of Japan (FCCJ) recommended protocol [98]. Initial ECSA of the conditioned MEA was calculated by performing in-situ CV measurements at 80 °C with fully humidified conditions. In second step, potential cycling was carried out at 500 mV s^{-1} between 1 V to 1.5 V as shown in Figure 3.6. After every 500 cycles, ECSA was calculated till 50% of the initial ECSA was reached.

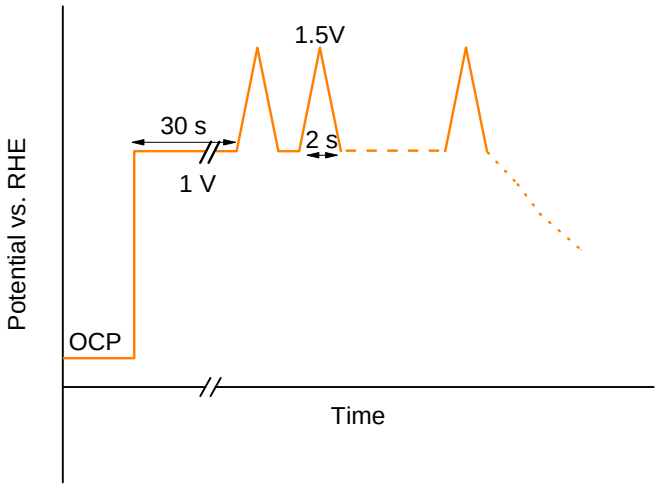

Figure 3.6: Potential cycle (start-stop) test conditions.

3.4.2 In-situ impedance studies

Electrochemical impedance spectroscopy can play a vital role in understanding the interplay of many factors that include structural and operating characteristics of the cell. In our work, it is carried out mainly to determine proton resistance of the electrodes. A number of experimental and modelling papers using AC impedance describe procedures for determining electrode ohmic resistance [99–101].

For the study, both the fuel cell anode and cathode were purged with H_2 and N_2 gases respectively with 33% relative humidity for proton conductivity. The cell was operated

at 80 ° C and was equilibrated for at least 60 minutes at the open circuit voltage (0.1 V) after which the working electrode (cathode) was scanned from 65 kHz to 0.1 Hz at an AC perturbation of 15 mV.

The measurements were performed using Reference-3000^{TM} from the Gamry Instuments Inc and analyzed using Echem-Analyst.

3.5 Electrospinning

Electrospinning was carried out using an electrospinner from IME technologies, Netherlands. A homogeneous solution was taken in a syringe and fed to the electrospinning chamber at different flow rates (normally 2.5 µl min^{-1}) using a pump. The distance between the collector and the needle can be varied (normally was set to approximately 12 cm and a voltage between 0 - 20 kV was applied to the needle (positive side) and an additional -2 kV was applied to the collector (negative side) to direct the fibers to the collector. The control of the flow of the solution, and the potential applied was carried out using the computer control of the system. Electrospinning was carried out for different times to get felts of varying thickness. Fibers are collected either on a Molybdenum plate or GDL or aluminum foil clamped on to the collector plate. Photograph of the electrospinning setup is shown in Figure 3.7. This apparatus can also be used for electrospraying, by using a dilute solution with a higher potential range ($\approx$ 20 kV).

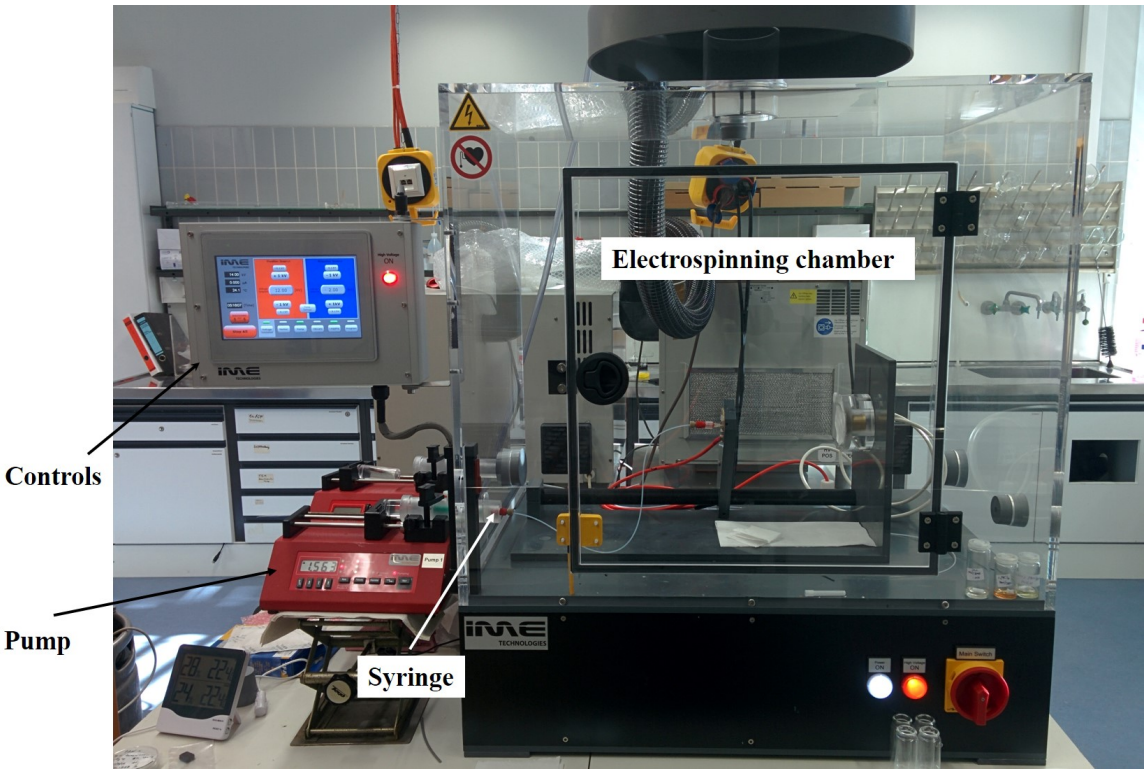

(a) Photograph of electrospinning chamber showing controls, pump etc.

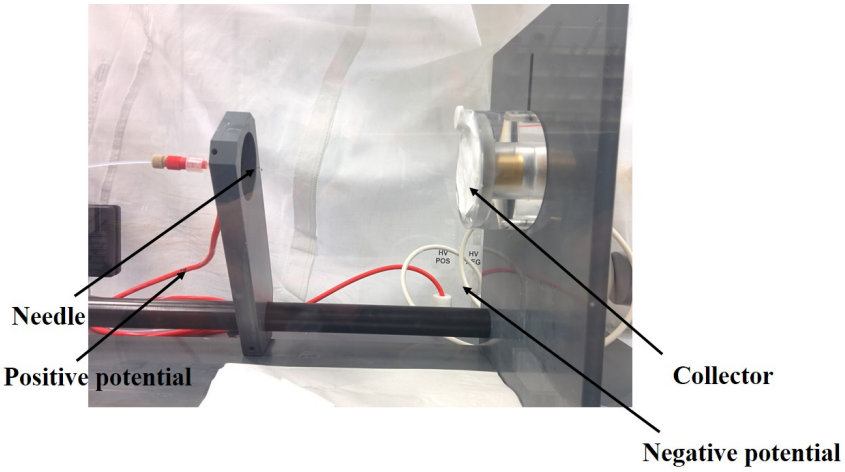

(b) Closeup of the electrospinning chamber showing needle, collector etc.

Figure 3.7: Photographs of electrospinning setup showing different parts.

Chapter 1

Freestanding Catalyst Layers: A novel electrode fabrication technique for PEM Fuel Cells via Electrospinning

This chapter has been submitted as a journal article to *ChemElectroChem* under the same title (DOI: 10.1002/celc.201600530) and reproduced as it is here.

In this chapter, a novel MEA fabrication technique for PEM fuel cells using the technique of electrospinning is presented. The structure is freestanding and contains carbon nanotubes enforced carbon nanofibers (eCNF-NTs) which give the electrode its structure. eCNF-NTs are prepared by carbonization of electrospun polyacrylonitrile containing CNTs. The structure is maintained throughout the process. Pt is decorated on the surface of the fiber structures via impregnation of Pt precursor and successive reduction. The electrode structure is hot-pressed by inserting it between gas diffusion layer (GDL) and membrane to form the cathode. The novel fabrication technique is versatile and can be used to prepare electrodes of different morphologies. In this work, we demonstrate the potential of the technique by preparing a highly porous network which shows a very high Pt utilization of approx. 90% for a loading of 0.3 mg_{Pt} cm^{-2}. In comparison, a standard electrode prepared via hot-spray technique has a catalyst utilization of 60% for the same loading.

Contents of this chapter is published in ChemElectroChem
DOI: 10.1002/celc.201600530

Contents of this chapter is published in ChemElectroChem
DOI: 10.1002/celc.201600530

Contents of this chapter is published in ChemElectroChem
DOI: 10.1002/celc.201600530

Contents of this chapter is published in ChemElectroChem
DOI: 10.1002/celc.201600530

Contents of this chapter is published in ChemElectroChem
DOI: 10.1002/celc.201600530

Contents of this chapter is published in ChemElectroChem
DOI: 10.1002/celc.201600530

Contents of this chapter is published in ChemElectroChem
DOI: 10.1002/celc.201600530

Contents of this chapter is published in ChemElectroChem
DOI: 10.1002/celc.201600530

Contents of this chapter is published in ChemElectroChem
DOI: 10.1002/celc.201600530

Contents of this chapter is published in ChemElectroChem
DOI: 10.1002/celc.201600530

Contents of this chapter is published in ChemElectroChem
DOI: 10.1002/celc.201600530

Contents of this chapter is published in ChemElectroChem
DOI: 10.1002/celc.201600530

Contents of this chapter is published in ChemElectroChem
DOI: 10.1002/celc.201600530

Contents of this chapter is published in ChemElectroChem
DOI: 10.1002/celc.201600530

Contents of this chapter is published in ChemElectroChem
DOI: 10.1002/celc.201600530

Contents of this chapter is published in ChemElectroChem
DOI: 10.1002/celc.201600530

Contents of this chapter is published in ChemElectroChem
DOI: 10.1002/celc.201600530

Contents of this chapter is published in ChemElectroChem
DOI: 10.1002/celc.201600530

Contents of this chapter is published in ChemElectroChem
DOI: 10.1002/celc.201600530

Contents of this chapter is published in ChemElectroChem
DOI: 10.1002/celc.201600530

Contents of this chapter is published in ChemElectroChem
DOI: 10.1002/celc.201600530

Contents of this chapter is published in ChemElectroChem
DOI: 10.1002/celc.201600530

Contents of this chapter is published in ChemElectroChem
DOI: 10.1002/celc.201600530

Chapter 5

Evaluating polyacrylic acid-Nafion composite as stable catalyst support for PEM fuel cell electrodes

Recently, high-performance fuel cell electrodes were obtained by electrospinning a suspension containing proton conducting Nafion and commercial platinum catalyst powder [88, 112]. Electrospinning of the catalyst together with Nafion ionomer enhances the triple phase boundary density, which resulted in improved fuel cell performance. To electrospin the suspension, a small addition of a polymer such as polyacrylic acid (PAA), polyethylene oxide (PEO) is necessary. It was found that the stability of the electrodes was significantly higher than the electrodes prepared from the same catalyst by conventional methods [90]. It was hypothesized that PAA played a critical role in improving the stability of the electrode.

In this work, we study polyacrylic acid-Nafion composite as a possible catalyst support for PEM fuel cell electrodes. The binding property of PAA-Nafion permits the masking of freshly prepared Pt nanoparticles, which are produced by the photochemical reaction of the Pt precursor induced by UV light. A small amount of Nafion acts as surfactant for the reaction. Carbon is added in a later stage for electrical conductivity. PAA-Nafion, being a stable polymer compound with strong binding properties separated Pt from carbon, thus stopping Pt enhanced carbon corrosion. This was studied by potential cycling in aqueous solution wherein there was no change in crystallite sizes of Pt before and after cycling. This was also confirmed by accelerated degradation studies in a fuel cell test-bench which showed that 52% of the ECSA was retained after 5000 cycles whereas commercial catalyst lost most of the activity in the first 2000 cycles.

The prepared catalyst suspension had a recipe suitable for electrospinning.

5.1 Experimental

5.1.1 Preparation of catalyst

For the preparation of Pt/PAA-Nafion, first 121 mg of $H_2PtCl_6 \cdot 6\,H_2O$ was dissolved in 4 ml of 1:1 H_2O/isopropanol (IPA) mixture in a thermostated glass cell. 90 µl of 5 wt.% Nafion was added to the solution as surfactant and was continuously stirred using a magnetic stirrer. The cell was illuminated by a 300 W bulb comprising a large spectrum in the UV range (Osram Ultra Vitalux). The temperature was regulated by connecting the cell to the circulating water at room temperature. A photograph of the setup is shown in Figure 5.1. The sample was irradiated with the UV light for 8-16 hours till the sample turned completely black [124, 125] indicating the formation of Pt nanoparticles.

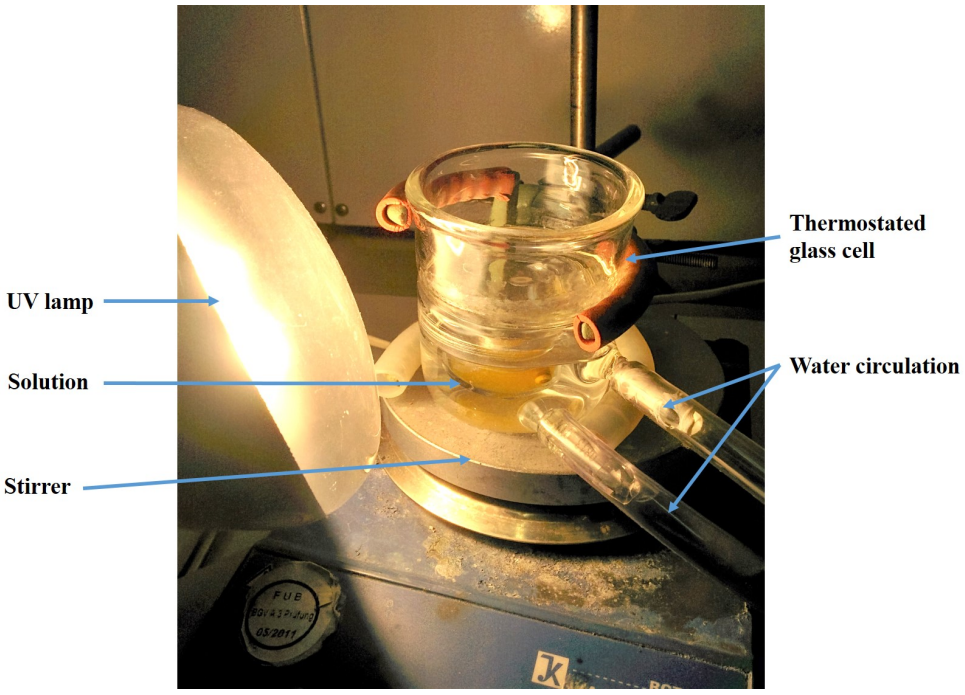

Figure 5.1: Setup of photochemical reduction of Pt precursor into Pt nanoparticles.

To the obtained suspension, 40 mg PAA (average $M_w \approx 450{,}000$) and 240 µl of 5 wt.% Nafion solution was added and stirred for a day to obtain a uniform suspension. Carbon (Vulcan XC-72) was added for the purpose of electrical conductivity. The suspension was ultrasonicated and kept for stirring for one more day.

The obtained suspension can be electrospun with varying success (See Figure 5.5a). However this is not done for most of the following experiments.

5.1.2 Fuel cell testing

The MEAs were prepared by hand-brushing the catalyst onto the GDL. For this purpose, the catalyst solution was diluted four times. The catalyst was hand-brushed with simultaneous drying using a heat gun at low power similar to as the procedure described in chapter 4 section 1.3. At the anode, the electrodes were prepared by hand-brushing 20 wt.% Pt/C commercial catalyst (HiSpec 3000). The anode loading was kept constant at approx. 0.31 mg_{Pt} cm^{-2}. The Pt loading was always kept high enough to discard any overpotentials arising in the anode. The materials were held together by hot-pressing at 140 °C and 2.5 MPa for 4 minutes to form the MEA.

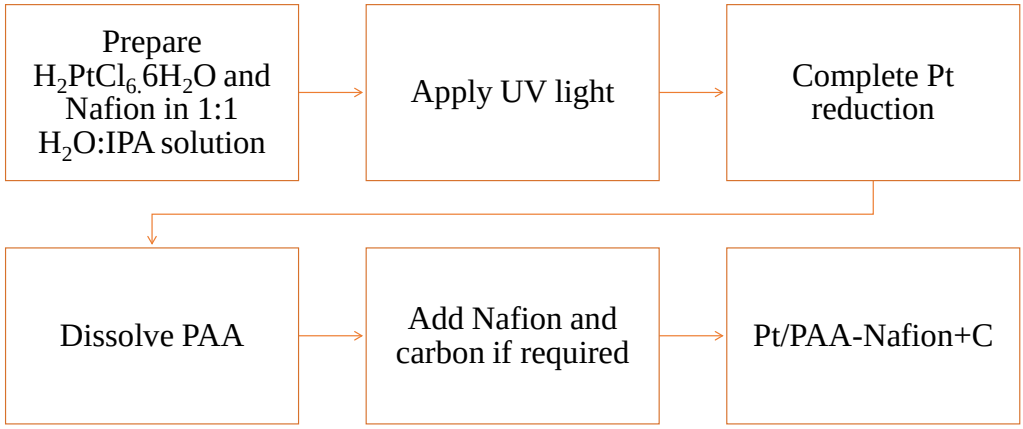

Figure 5.2: Procedure for preparation of Pt/PAA-Nafion electrodes.

5.2 Results and Discussions

5.2.1 PAA and Nafion

Polyacrylic acid is a simple polymer consisting of the homopolymer of acrylic acid as shown in Figure 5.3, which is stable in strong acids and bases. Polyacrylic acid, being a weak anionic polyelectrolyte, can associate with various non-ionic polymers (such as polyethylene oxide, polyacrylamide, etc) via hydrogen-bonded inter-polymer complexes or with oppositely charged polymers (like chitosan, streptomycin) to form poly-complexes. PAA is an atactic polymer which dissolves easily in water and alcohol. PAA has a glass transition temperature (T_g) of 106 °C.

Nafion is a sulfonated tetrafluoroethylene based fluoropolymer-copolymer which is also highly stable against chemical attacks. Nafion is used not only as proton conducting ionomer, but also as a superacid catalyst, and as a surfactant in the preparation of nanoparticles. Nafion has a T_g between 120 °C - 140 °C.

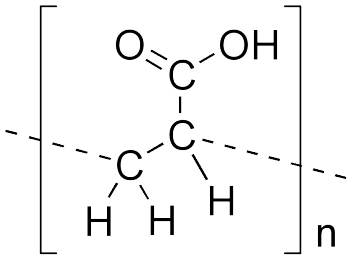

Figure 5.3: Structure of polyacrylic acid.

Electrospinning of Nafion was found to produce interesting properties. Dong et. al [126] reported the conductivity of Nafion nanofibers to be 1.5 S cm^{-1}, bulk Nafion on the other hand, has a proton conductivity of just ~ 0.1 S cm^{-1}. They link this phenomenon to a change in orientation of ionic group in the nanofibers in contrast to the isotropic morphology in the bulk film. Electrospinning of Nafion alone is not possible owing to an insufficient entanglement. So a small amount of PAA is mixed into the Nafion. The minimum amount of PAA that is needed for a bead free electrospinning with an inconsequential loss in conductivity was reported to be around 25% by weight [69].

To study the interactions of PAA with Nafion and to understand the type of bonding that might be present, Fourier transform infrared (FTIR) spectroscopy was used. Five different samples were studied i.e (a) PAA, (b) Nafion (c) uniform solution of 1:2 PAA-Nafion mixture, (d) PAA-Nafion heated mixture (heating the 1:2 solution of PAA-Nafion solution up to 140 °C) and (e) electrospun PAA- Nafion (prepared by electrospinning). The characteristic vibrations of the pure samples of PAA (Figure 5.4 a) and Nafion (Figure 5.4 b) were observed and each band can be assigned to vibrations of different functional groups which are listed in Table 5.1. The PAA-Nafion mixture (Figure 5.4 c) as such did not show any characteristic interaction, the individual characteristic bands of Nafion and PAA are clearly seen in the mixture. There is no detectable shift in the bands suggesting only minimal interaction. PAA has a T_g at 106 °C, Nafion has a T_g at 140 °C. For the sample heated up to 140 °C (Figure 5.4 d), both PAA and Nafion are expected to associate strongly with each other due to dissolution of micro crystals formed in the polymer. For the bands other than the broad OH band ($\sim$3101 cm^{-1}), there is no change in the vibrational bands, the bands associated with Nafion molecule, - C-F related stretching bands (1221.1 cm^{-1}, 1154 cm^{-1}, 982 cm^{-1}) as well as the S=O (1060 cm^{-1}) stretching bands are not affected by the addition of PAA. This holds true for the electrospun fibers too (Figure 5.4 e). The proton conducting property of Nafion, as the sulfonic group is not affected, is also not hindered. The only change observed is in the hydrogen bonding region. The broad band intensity shifts from the wavenumber region 3101 cm^{-1} to 3456 cm^{-1} for the heated sample and a bit more intensely for the electrospun sample, suggesting that the average strength of the hydrogen-bonds has decreased. This may be due to formation of weak hydrogen bonds with the Nafion chain. From this analysis, it can be assumed that the addition of

Table 5.1: Designated frequencies and assignments of infrared bands of PAA and Nafion [127, 128].

IR (υ cm^{-1})	Assignments	IR (υ cm^{-1})	Assignments
PAA		**Nafion**	
3101	O-H stretching	1221.1	CF_2 stretching asymmetric
2947	CH_2-CH stretching	1154.2	CF_2 symmetric stretching
1711	strong C=O stretching	1060	S=O stretching
1451	CH_2 deformation	982	C-F stretching ($CF_2-CF(CF_3)$)
1413	C-O stretching coupled with OH in plane bending		
1178	C-O stretching coupled with OH in plane bending		
1112	C-CH_2 stretching		
804	CH_2 twisting and C-COOH stretching		

PAA to the Nafion does not reduce its proton conductivity. It was initially assumed that thermal treatment above the glass transition temperature of PAA (T_g 106 °C) can induce a dehydration reaction of the carboxylic acid groups, resulting in covalent cross-links among the PAA chains. Unfortunately, no characteristic anhydride group peaks near 1803 cm^{-1} and 1030 cm^{-1} were observed. This may be due to the fact that the process of anhydride formation and crosslinking is very slow for pure PAA and so may be the case with addition of Nafion.

It can also be observed that the FTIR spectrum of PAA-Nafion heated up to 140 °C has a spectrum similar to the properties of electrospun sample. PAA-Nafion composite was used as a replacement to mimick the chemical properties, in places where electrospinning was not possible.

5.2.2 Synthesis of Pt/PAA-Nafion

For the preparation of metal nanoparticles, metal ions have often been reduced in various polymers and surfactants. These materials can act as capping agent which can bring control

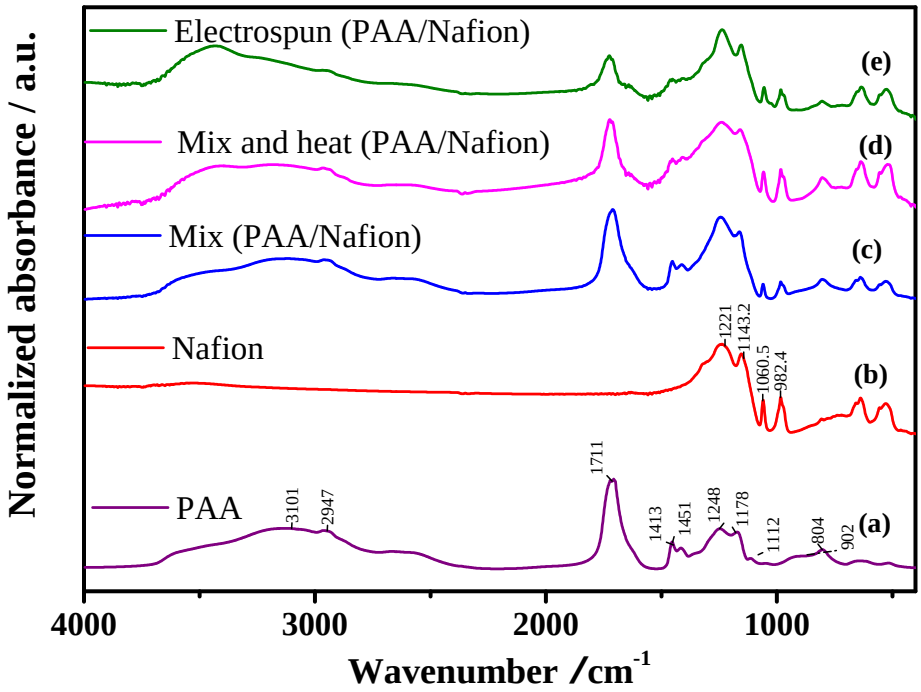

Figure 5.4: FT-IR spectra of (a) PAA, (b) Nafion, (c) PAA-Nafion mixture, (d) PAA-Nafion mixture after heating to 140 °C, and (e) electrospun PAA-Nafion.

on shape and size of the Pt particles often determining the activity of the Pt nanoparticles.

Photoirradiation of UV light for $PtCl_6^{2-}$ is a well known reduction technique. Harada and Eniga [124] studied the formation mechanism of the Pt particles by photo-reduction.

$$PtCl_6^{2-} \rightarrow PtCl_4^{2-} \rightarrow Pt^0 \tag{5.1}$$

The reduction of $PtCl_6^{2-}$ to $PtCl_4^{2-}$ is fast and can be observed with a colour change from yellow to orange within 2 hours of the reaction. The reduction of $PtCl_4^{2-}$ to Pt^0 is slow and takes between 8- 16 hours to complete. It was observed that the reaction is accelerated by the availability of Pt and slowed by the presence of the polymer. In final stages, the reaction goes to completion, even in the absence of light, suggesting that the freshly prepared Pt nuclei catalyze the reaction.

Both Nafion and PAA can act as a stabilizing agent for the freshly formed Pt nanoparticles in a 1:1 water isopropanol solution. (Described in chapter 6, section 2.2 - Figure 6.11). Even though both PAA and Nafion controlled Pt nanoparticle growth, the Pt nanoparticles were seen to form agglomerations. It is assumed that PAA being an anionic polymer, repelled the $PtCl_6^{2-}$ resulting in agglomeration of the synthesized Pt nanoparticles. Nafion on the other hand, acts as micelle above the critical micelle concentration (cmc), driving the synthesized

Pt nuclei together. However, when the synthesis is carried out below cmc (0.01% w/w), there is still a capping effect and no agglomeration of Pt nanoparticles is seen in the TEM image of electrospun 40 wt.% PAA-Nafion catalysts (Figure 5.5).

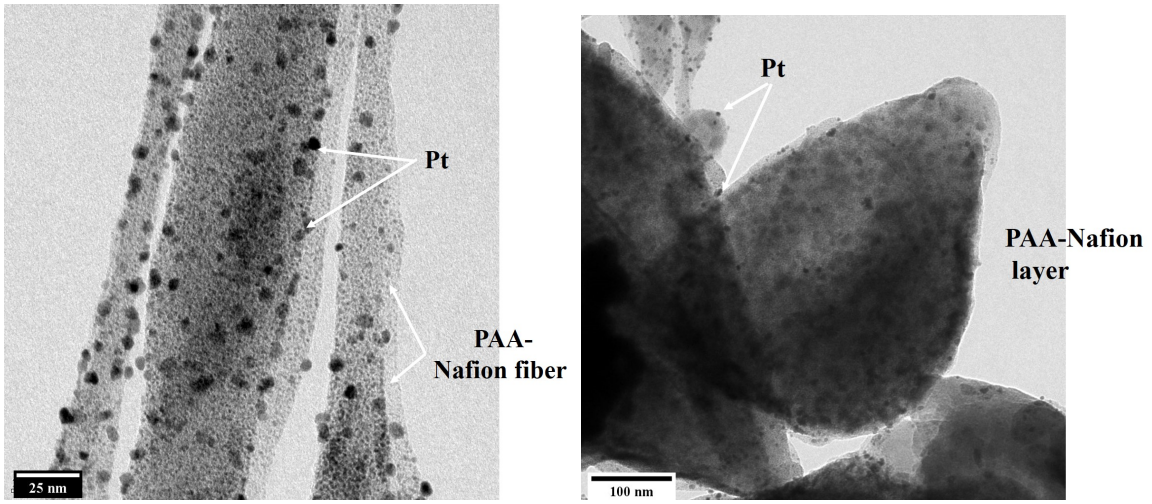

(a) (b)

Figure 5.5: TEM images of Pt/PAA-Nafion electrospun fiber strands.

As mentioned before, it is possible to electrospin the suspension with varying amount of success. Figure 5.5 shows the TEM images of the electrospun Pt/PAA-Nafion solution. Figure 5.5a shows the formation of thinner electrospun split- fibers, and in Figure 5.5b, these thin streams combine together to form a layer. A further optimization of the ink recipe and electrospinning setup is required for smooth uninterrupted electrospinning. In this study, the stability of Pt/PAA-Nafion is evaluated rather than electrospinning parameter optimization is carried out.

5.2.3 Addition of carbon

Carbon is added as an additional component to provide the required electrical conductivity. A thin layer of PAA-Nafion separates Pt nanoparticles from the carbon as seen in Figure 5.6. This should stop Pt enhanced corrosion as carbon corrosion is favored when Pt is supported on it [26].

Potential cycling gives an overall idea of the stability of the electrode. Potential cycling leads to sintering and migration of Pt resulting in loss in Pt nanoparticles surface area which can be due to both Pt dissolution and carbon corrosion [116].

Two sets of samples were analyzed by potential cycling. In the first set, Pt nanoparticles are supported only on PAA and Nafion (Pt/PAA-Nafion) without any carbon addition. Here,

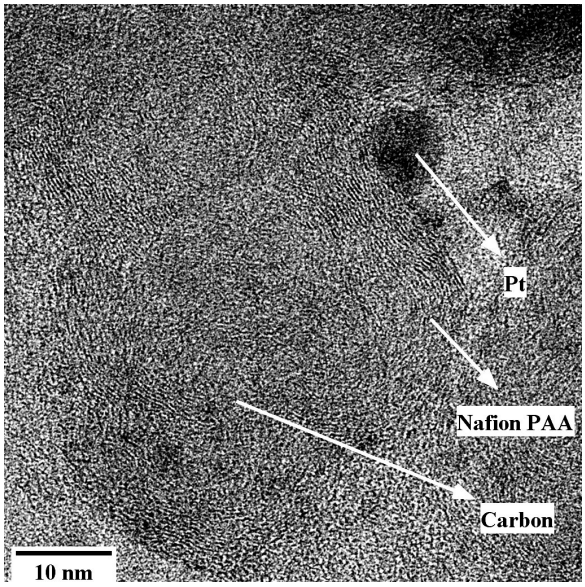

Figure 5.6: Transmission electron micrograph of electrospun Pt/PAA-Nafion+C.

the electrical conductivity is taken care by Pt nanoparticles, due to which loading of Pt needs to be kept high, i.e. 60 wt.% [57]. In the second set of samples, Vulcan carbon was added to the solution to have a final composition of 20 mg Pt, 30 mg C, 16.4 mg PAA and 32.8 mg Nafion and is called Pt/PAA-Nafion+C.

For the purpose of potential cycling, from the colloidal solution 10 µl solution is pipetted out and dropped on a glassy carbon strip. The strip was kept in an oven at 140 °C for the cross-linking. Potential cycling was carried out for 1000 cycles in a three electrode setup. Figure 5.7 shows the cyclic voltammograms of Pt/PAA-Nafion and Pt/PAA-Nafion+C in different potential cycles. Corresponding ECSA is plotted in the inset and tabulated in Table 5.2.

The catalyst containing PAA-Nafion+C has a better ECSA (≥ 80 m^2 g^{-1}), in comparison to PAA-Nafion (≤ 50 m^2 g^{-1}) which suggests that the insufficient electrical conductivity of PAA-Nafion leads to low Pt utilization.

For both samples, the ECSA can be divided into three regions as shown in the inset of Figure 5.7.

- Region 1: Between cycles 0-50 for Pt/PAA-Nafion and 0-100 for Pt/PAA-Nafion+C, the region is characterized by the activation of the Pt nanoparticles which results in an increase in the electrochemical surface area. For Pt/PAA-Nafion, ECSA increased by 10% and for Pt/PAA-Nafion+C it nearly doubled.
- Region 2: Between cycles 50-200 for Pt/PAA-Nafion and 100-300 for Pt/PAA-Nafion+C, a rapid decrease in ECSA is observed. For Pt/PAA-Nafion, the ECSA falls

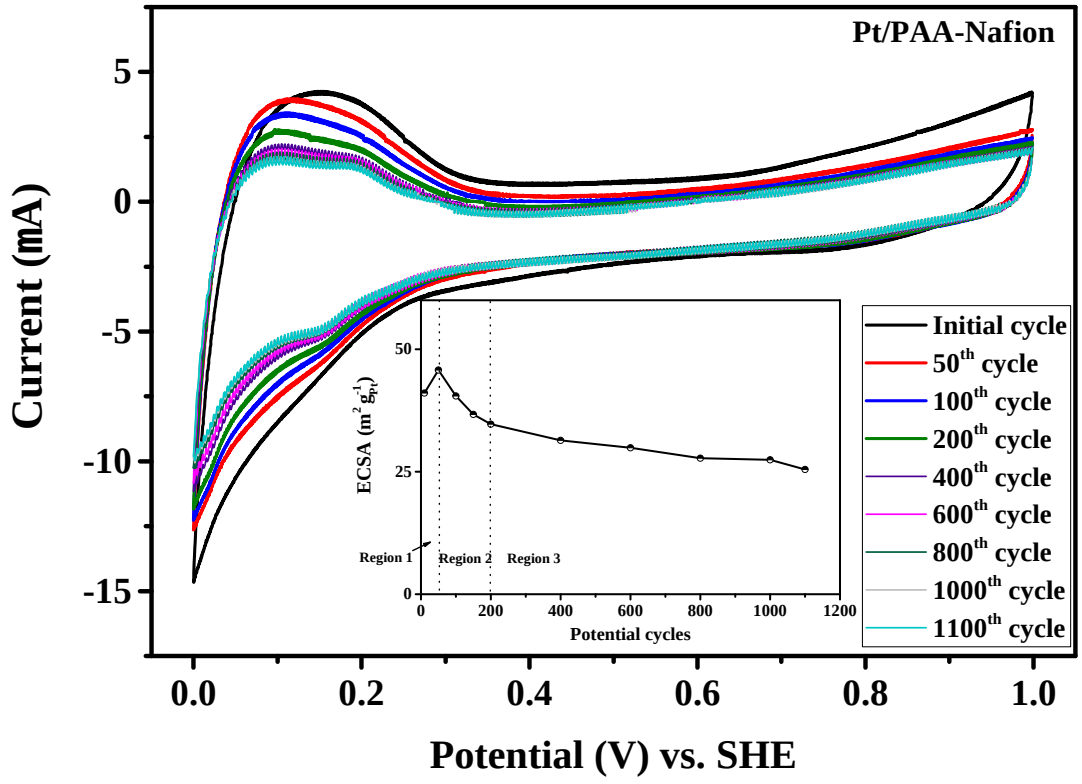

(a)

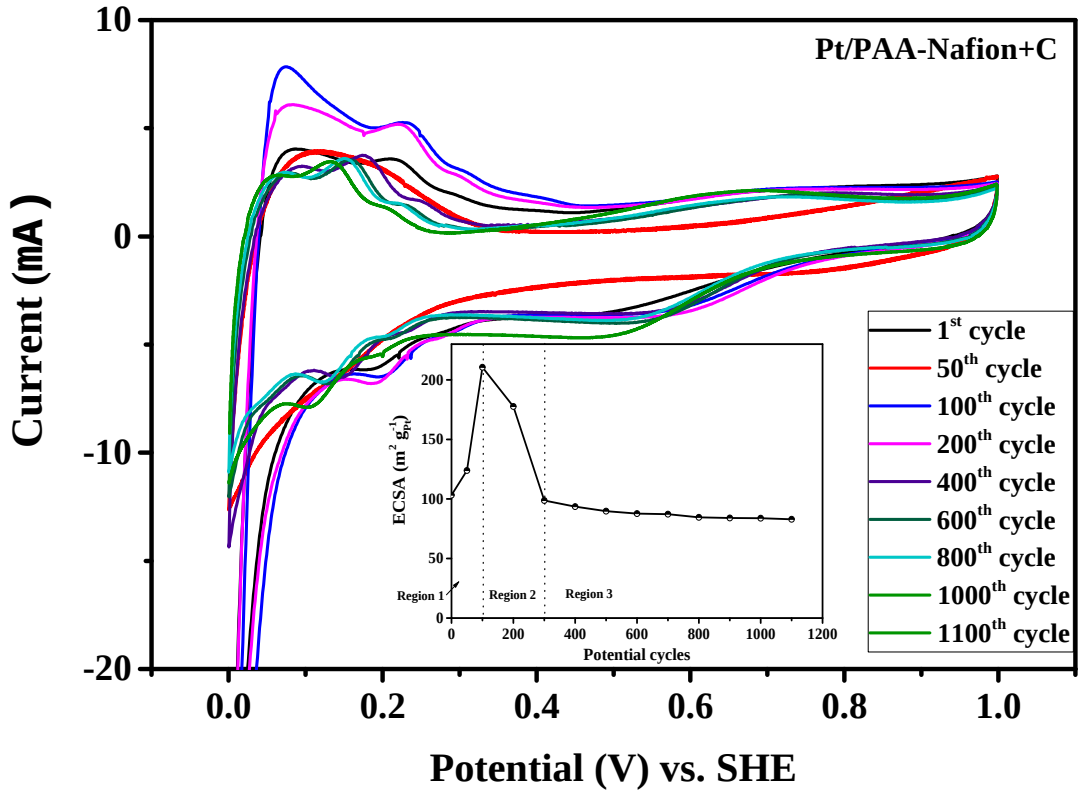

(b)

Figure 5.7: Potential cycling of (a) Pt/PAA-Nafion and (b) Pt/PAA-Nafion+C.

from 46 $m^2\ g^{-1}$ to 35 $m^2\ g^{-1}$. For Pt/PAA-Nafion+C on the other hand, the activity also decreased from 210 $m^2\ g^{-1}$ to 98 $m^2\ g^{-1}$. The reason for the decrease can be attributed to the fact that in the preparation of the Pt colloid, a small amount of tiny Pt ($\approx$ 1 nm) particles are also formed resulting in high ECSA, more than the geometrical surface area of the Pt catalysts which is 93 $m^2\ g^{-1}$ (considering Pt crystal size 3 nm from XRD). These Pt nanoparticles are very active, however unstable. They sinter or dissolve rapidly, which is seen as steep initial fall in ECSA. Since this has arisen from the preparation, both the samples show this characteristic.

- Region 3: Between cycles 200-1000, there is a stable region with only a slow change which can be related to the slow degradation of carbon particles with associated sintering and Pt agglomeration. For Pt/PAA-Nafion catalysts, there is a more severe decrease by 30% is observed suggesting Pt agglomeration, whereas for Pt/PAA-Nafion+C the decrease is smaller around 19%.

Table 5.2: No. of cycles and corresponding ECSA

Pt/PAA-Nafion			**Pt/PAA-Nafion+C**		
Cycles	ECSA ($m^2\ g_{Pt}^{-1}$)		Cycles	ECSA ($m^2\ g_{Pt}^{-1}$)	
10	41	} +11.4%	0	103	} +104%
50	46		50	124	
100	40	} -20.1%	100	210	} -53.6%
200	35		200	177	
400	31		300	98	
600	29	} -30%	400	94	
800	28		600	88	} -19%
1000	27		800	85	
			1000	83	

The stability of the particles can be further studied taking XRD before and after of the samples and their x-ray patterns are shown in Figure 5.8. The particle size of the freshly synthesized Pt nanoparticles was 3 nm. After subjecting them to potential cycling, the crystal size of Pt increased to 3.8 nm for Pt/PAA-Nafion and no increase in the Pt size was observed for the catalysts prepared with the addition of carbon (Pt/PAA-Nafion+C). From the results obtained by potential cycling combined with XRD, these two points can be inferred:

- Coating PAA-Nafion on the Pt catalyst does not hinder Pt agglomeration. In some stable support, like ceramic oxides, Pt agglomeration is controlled due to the support

interactions. [14]. In the case of PAA-Nafion this is not the case, as there was an increase in crystal size of the Pt nanoparticles upon potential cycling from 3 nm to 3.8 nm,

- Physical addition of carbon to PAA-Nafion increases the surface area, increases the dispersion of the Pt nanoparticles and at the same time slows down Pt agglomeration, which resulted in no increase in Pt size for Pt/PAA-Nafion+C catalysts.

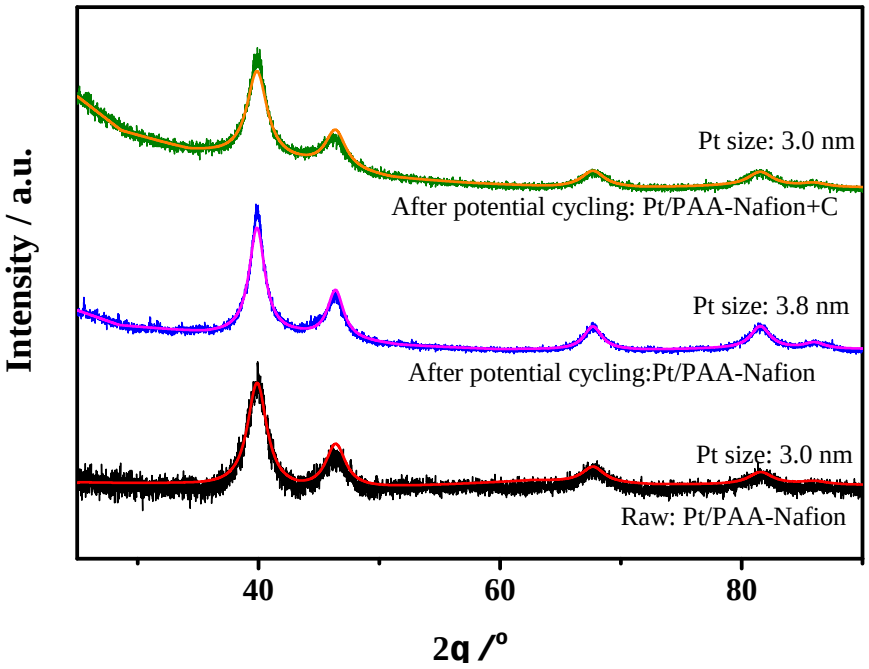

Figure 5.8: X-ray diffraction patterns of Pt/PAA-Nafion before and after potential cycling with and without carbon.

5.2.4 In-situ durability test

In-situ fuel cell potential cycling was performed targeting an accelerated degradation of the carbon support. The tests were performed at 80 °C with potential cycling carried out between 1 V and 1.5 V at 0.5 V s^{-1}, according to 'Fuel cell corporation Japan' (FCCJ) testing protocol as described in chapter 3, section 5.1.

Figure 5.9 shows the normalized ECSA of the Pt/PAA-Nafion+C and of commercial Pt/C (HiSPEC 3000) calculated at different intervals (0, 500th, 1000th, 2000 th, 3000th and 4000th). ECSA was calculated by stopping the degradation protocol and then carrying out cycling between 0.05 V -1 V. The hydrogen-adsorption region was used to calculate the ECSA of the catalyst layer.

For the commercial Pt/C catalysts, degradation is fast. A rapid fall in ECSA was observed, only 10 wt.% of the initial ECSA was retained, afterwards fluctuating by 4 wt.%. For Pt/PAA-Nafion+C, in the first 1000 cycles, the activity falls by 22.5%, then it slowly degrades and retains 52% of the activity even after 5000 cycles. As a downside, there is a structural change in the carbon as a result of partial oxidation characterized by a large increase in capacitance. This can be observed in Figure 5.9 by comparing the voltammograms before and after degradation.

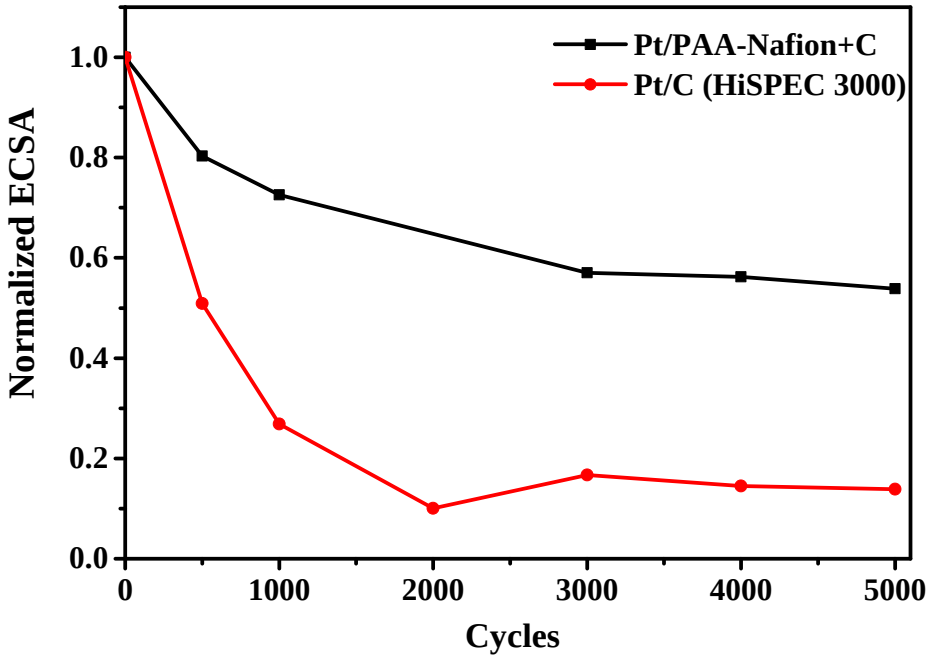

Figure 5.9: Normalized ECSA of Pt/PAA-Nafion+C and commercial Pt/C (HiSPEC 3000) at different potential cycles.

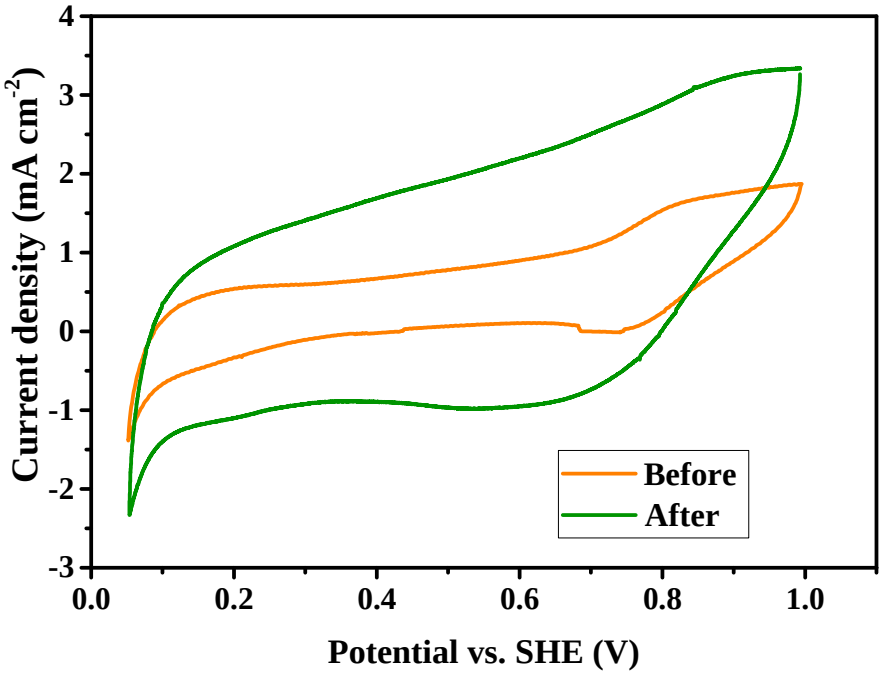

Figure 5.10: In-situ cyclic voltammograms taken before and after the degradation study of Pt/PAA-Nafion+C at 80 °C.

5.3 Conclusion

In this work, at first a Pt salt was reduced via photocatalytic reduction using Nafion as a surfactant. Addition of PAA-Nafion to the obtained solution coats a thin layer over Pt nanoparticles to obtain Pt/PAA-Nafion electrocatalysts having crystal sizes of 3.0 nm. Addition of carbon as a physical mixture played an important role in increasing electrical conductivity and improving Pt nanoparticle dispersion. In-situ accelerated degradation tests showed that PAA-Nafion successfully separated Pt from carbon resulting in slower degradation of the catalyst.

In this work, Vulcan carbon is added as a physical mixture for easier comparison with commercial Pt/C (HiSPEC 3000). However, use of highly stable carbons like non-functionalized CNT can also be envisioned with minimal changes to the synthesis protocol which might further enhance the stability of the catalysts.

Chapter 6

Additional Topics

Two additional topics are discussed here. Even though these ideas were a bit adventurous and we were not able to test them to their full potential in a real fuel cell set-up, they were the milestones for initiating the work carried out in the previous two chapters.

Previously, in our group Peter et al. [129] prepared stable Pt nanoparticles on a carbonized PANI electrode. Pt nanoparticles in general start sintering and increase in size with increasing temperature [56]. But in the case of nitrogen doped carbons such as PANI, Pt can get anchored to the nitrogen groups resulting in reduced or even no Pt nanoparticle growth [129]. Further, the presence of Pt might also enhance graphitization of the carbon. An attempt was made to extend this concept to electrospun Pt/PAN fibers. Here, Pt salt containing PAN solutions were electrospun and reduced at different stages of carbonization process, 1) after spinning, 2) after stabilization and 3) after carbonization. The obtained samples were studied for Pt sintering, agglomeration and activity.

In another attempt, TiO_2 was used as catalyst support for the fuel cells. As discussed before
except for the stability aspects. Carbon corrodes slowly in fuel cell operation conditions forming CO_2, and thereby leads to a "thinning" of the porous electrode. The more stable titania is reported to show better support characteristics [14, 57]. Moreover, Pt with TiO_2 forms much stronger bonds than carbon via a so-called strong metal support interaction (SMSI). To outperform carbon based supports, the catalyst activity with the metal oxide supports needs to be improved. Metal oxides including TiO_2 tend to form dense structures yielding low porosity in the electrodes. Moreover, they are electrically non-conducting. For these reasons, it is important to mimic the qualities that carbon support bestows on Pt catalyst. To address these issues, the electrospinning technique can be used by which a porous structure can be prepared. Pt plays the dual role of catalysis and electron conduction. In this work, a "potpourri" containing Pt precursor, PAA, Nafion and TiO_2 was prepared. Pt salt was reduced using a photoreduction technique like the one used in chapter 5 and subsequently electrospun. Physical and electrochemical characterization was carried out to evaluate the feasibility of this new preparation technique for fuel cell electrodes.

6.1 Electrospun Pt on carbon nanofiber

6.1.1 Experimental

First $H_2PtCl_6 \cdot 6\,H_2O$ (10 wt. % equivalent Pt/eCNF) was dissolved in a 10% PAN in DMF solution. The solution was electrospun with electrospinning conditions similar to the ones discussed in schematic in chapter 4, Figure 4.1. After electrospinning, carbonization of the fibers is a two step process as discussed before in chapter 4, i.e stabilization in air at 300 °C and carbonization in 1000 °C in N_2 atmosphere.

Here, Pt salt containing electrospun fibers can be reduced in three different ways as shown in Figure 6.1.

1. Pt precursor is reduced after electrospinning of fibers (Pt/eCNF-R1)
2. Pt precursor is reduced after stabilization of fibers (Pt/eCNF-R2)
3. Pt precursor is reduced after carbonization of fibers (Pt/eCNF-R3)

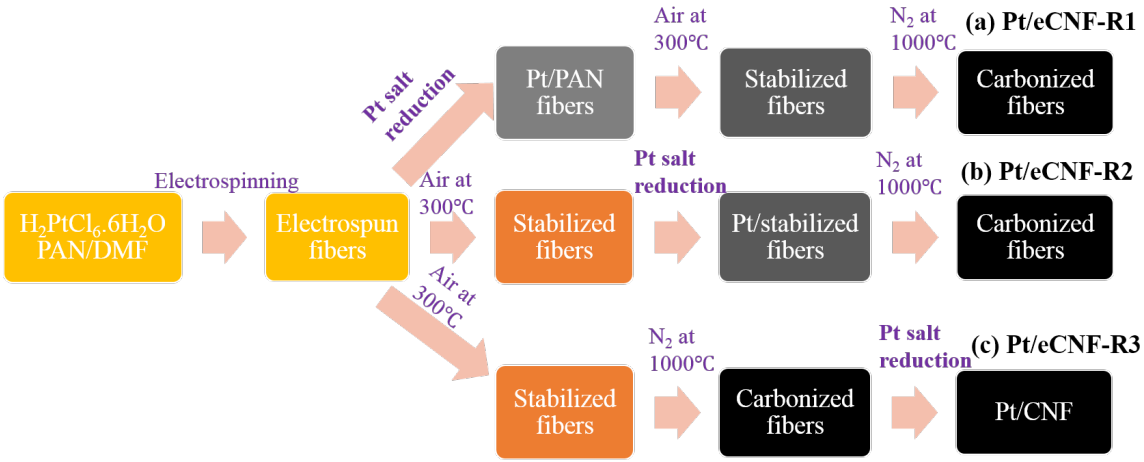

Figure 6.1: A schematic of Pt reduction at different stages of carbonization procedure.

Reduction of Pt salt was carried out using a simple polyol process [130, 131]. The Pt precursor containing fiber network was dipped in an ethylene glycol solution and was heated using a microwave at 130 °C with a heating rate of 1 °C per minute and maintaining the temperature for 1 minute for reduction of the salt to Pt. The samples were taken out from the solution and cleaned by washing in water and dilute hydrochloric acid.

6.1.2 Results and discussion

In the case 1, i.e. (Pt/eCNF-R1), the Pt precursor is reduced just after electrospinning Pt-salt-PAN fibers using the polyol method. In a later step, stabilization and carbonization of the fibers were carried out. Figure 6.2 shows the SEM image of the sample after the carbonization. The spaghetti like structure is clearly seen. Presence of Pt can be seen as huge agglomerated chunks outside the fibers. The fibers are slightly rough. The uniformity of Pt deposition is lost in this process.

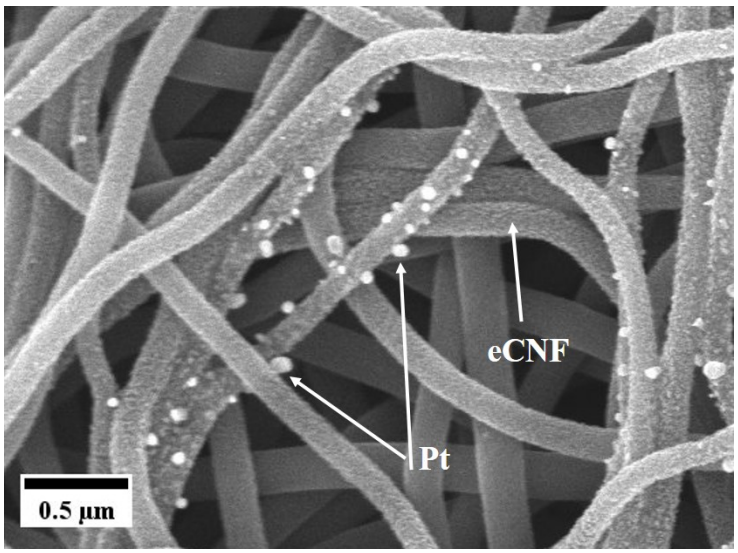

Figure 6.2: Scanning electron micrograph of Pt/eCNF-R1 (reduction after spinning) after carbonization,

In the case 2, i.e. Pt/eCNF-R2, Pt salt is reduced after stabilization of electrospun fibers, and before carbonization of fibers. Figure 6.3 shows the SEM image after the carbonization of the reduced sample. Pt is seen as white spots in the fiber network. Near to that small lines/markings on the fibers are also seen. This is believed to be caused by the Pt sintering when the temperature was gradually raised to 1000 °C during carbonization, leaving a trail of the Pt movement on the fiber structure.

In the case 3, the Pt salt is reduced in the final stage, i.e. after carbonization of the electrospun fibers. Figure 6.3 shows the SEM image of the sample. Small Pt particles are seen uniformly distributed and engraved in the fiber sample. The electrospinning of the solution with the Pt salts results in preferential deposition of Pt ions on the outer side of the fiber structure, which could be easily reduced. The obtained materials were further studied using XRD for determining the crystal size and cyclic voltammetry for the Pt activity. Figure 6.5 shows the XRD pattern for the Pt/eCNF-R3 sample which confirmed the complete conversion of the Pt precursor to pure Pt. Particle sizes calculated by refinement gave 10.1 nm as an average value. Figure 6.6 shows the cyclic voltammogram of the sample cycled between 0 V

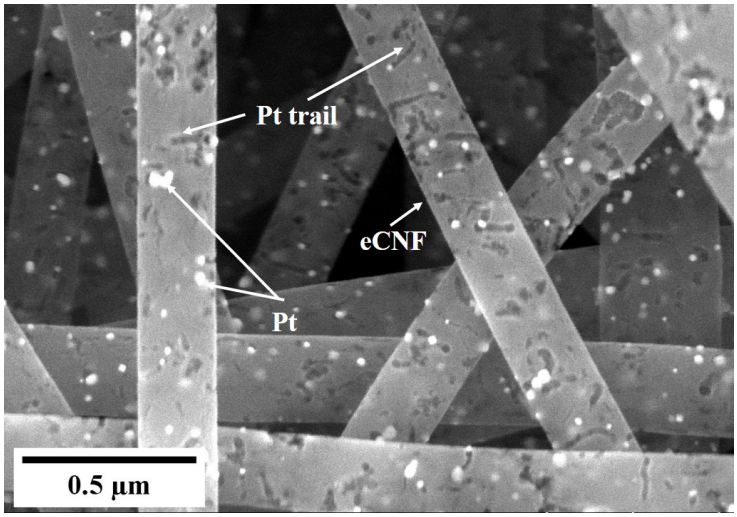

Figure 6.3: Scanning electron micrograph of Pt/eCNF-R2 (reduction after stabilization) after carbonization.

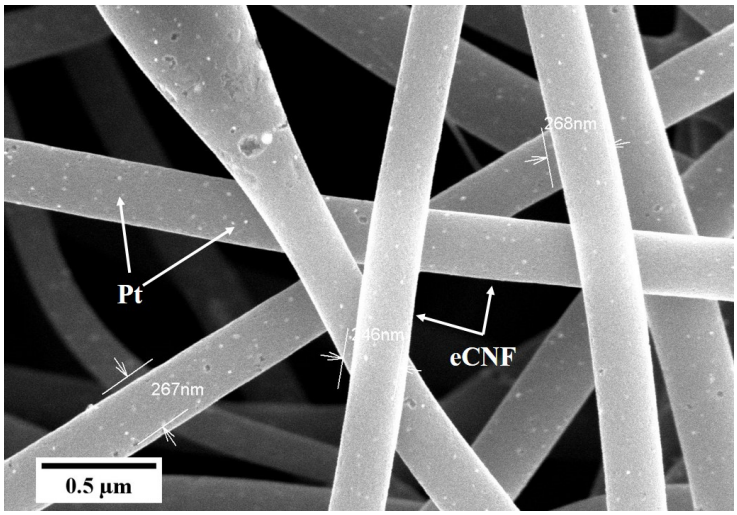

Figure 6.4: Scanning electron micrograph of Pt/eCNF-R3 (reduction after carbonization).

to 1.2 V in 0.1 M $HClO_4$ solution, with an inset of the commercial Pt/C (Hispec 3000) for comparison. The cyclic voltammogram shows some unique characteristics and is distinctly different from the commercial catalysts shown in the inset. The polycrystalline Pt peaks (between 0.05 V - 0.4 V) associated with the hydrogen desorption process are seen as a single hump. There is also a shift in the onset potential of the hydrogen adsorption-desorption region, which does not typically go higher than ≈0.4 V. Here, it goes beyond and seems to coincide with the quinone-hydroquinone redox peak at approx. 0.43 V. This can also lead to errors for the ECSA determination. ECSA was calculated to be 43 $m^2\ g^{-1}$.

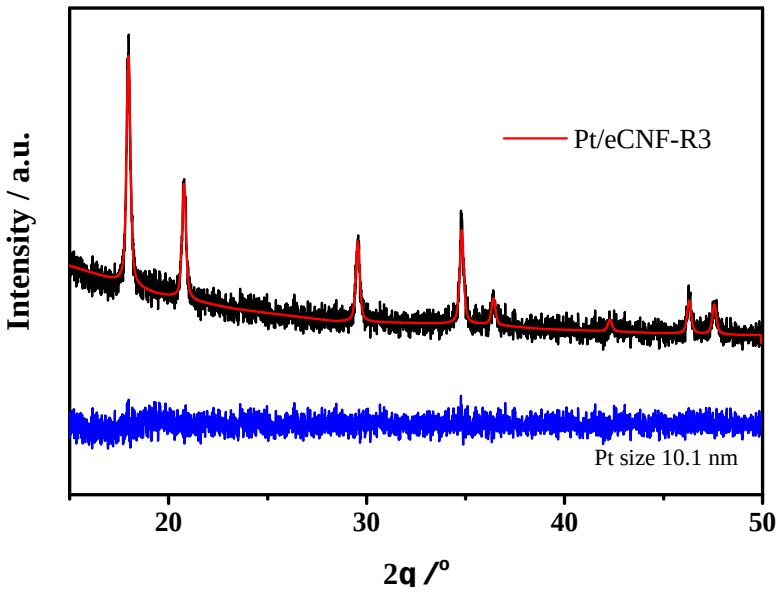

Figure 6.5: X-ray diffractogram of Pt/eCNF-R3. Mo ($K_{\alpha 1}$ 0.709 Å) anode was used instead of Cu. Here, — is the measured diffraction, — is the calculated pattern, and — is the difference curve between the measured and the calculated pattern.

6.1.3 Conclusion

Out of the three different samples, the reduction of the Pt precursor after carbonization showed some catalytic activity (Pt/eCNF-R3). However, in our case, the nitrogen in the PAN fibers did not play any significant role in hindering the Pt sintering as described by Peter et al. [129]. Pt/eCNF-R3 exhibits a uniform deposition of the Pt nanoparticles on the surface. Some treatment like chemical or electrochemical etching of the sample may be able to activate the Pt for further fuel cell cathodes. In chapter four, this issue was overcome by depositing Pt salt only after carbonization of the eCNF layer and not already as a component in the spinning solution.

The idea described herein may be deemed not suitable for fuel cell applications owing to the slightly high Pt size (approx. 10 nm instead of 2-5 nm) and low electrochemical

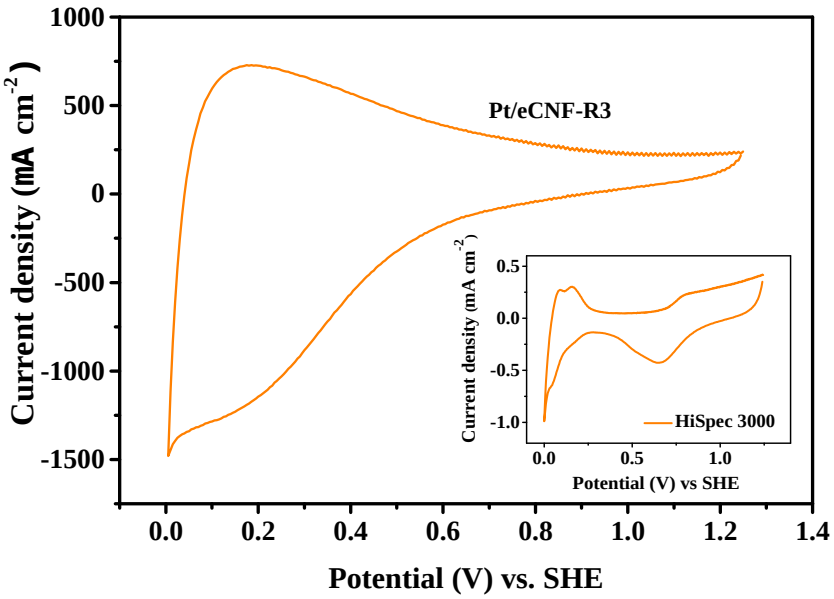

Figure 6.6: Cyclic voltammogram of Pt/eCNF-R3 in 0.1 M $HClO_4$ solution at 50 mV s^{-1} scan rate. The voltammogram is obtained after 50 cycles. Inset: commercial Pt/C (Hispec 3000).

activity. However, this technique can be useful in improving the performance of carbon based catalysts wherein inclusion of metal nanoparticles has shown to have a secondary effect, like Fe or Ni in the case of non-PGM type catalysts, and Pb or Sb in case of carbon felts for redox flow batteries.

6.2 Integrating stable oxide support material in electrodes via electrospinning

6.2.1 Experimental

Preparation of the electrospinning mixture

First, 40 mg of polyacrylic acid having a molecular weight of 450,000 is dissolved in 400 µl of an isopropanol-water solution and stirred overnight to obtain a viscous polymer solution. In the next step, 118 mg of TiO_2 and $H_2PtCl_6 \cdot 6\,H_2O$ are added in 1.846 ml of Nafion and homogenized for 5 min by means of an ultrasonic dispersion finger. This solution is then added to the polymer paste and stirred again overnight.

Reduction of Platinum precursor

The obtained yellowish solution is photochemically reduced with constant stirring. For this purpose, as shown in Figure 6.7, a 300 W lamp (Osram Ultra Vitalux) is used as the UV light source. The course of the reduction can be observed with the color change from yellow to light gray to dark gray / black. The photo-reduction serves the purpose to predominantly deposit the Pt nanoparticles on the oxide due to an light induced interaction.

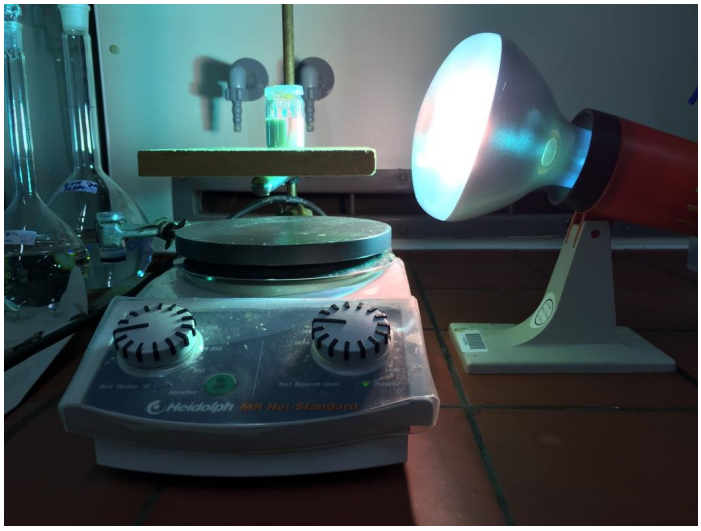

Figure 6.7: Photochemical reduction of platinum using 300 W UV light.

Electrospinning

The prepared solution is taken in a syringe and placed in the syringe pump. The solution reaches the needle tip through a plastic hose, where a high voltage (positive 20 kV, negative 2 kV) is applied to form the taylor cone. At the collector, carbon paper with an area of 8.72 cm^2 is mounted to collect the fibers (cathode). The distance between needle tip and collector is kept at 13 cm and a flow rate of 2 µl min^{-1} is used. A dilution of the polymer solution with 1600 µl of an isopropanol-water solution favors the electrospray method, which leads to the formation of particles. A schematic of the photo-reduction of Pt salts and subsequent electrospinning is shown in Figure 6.8.

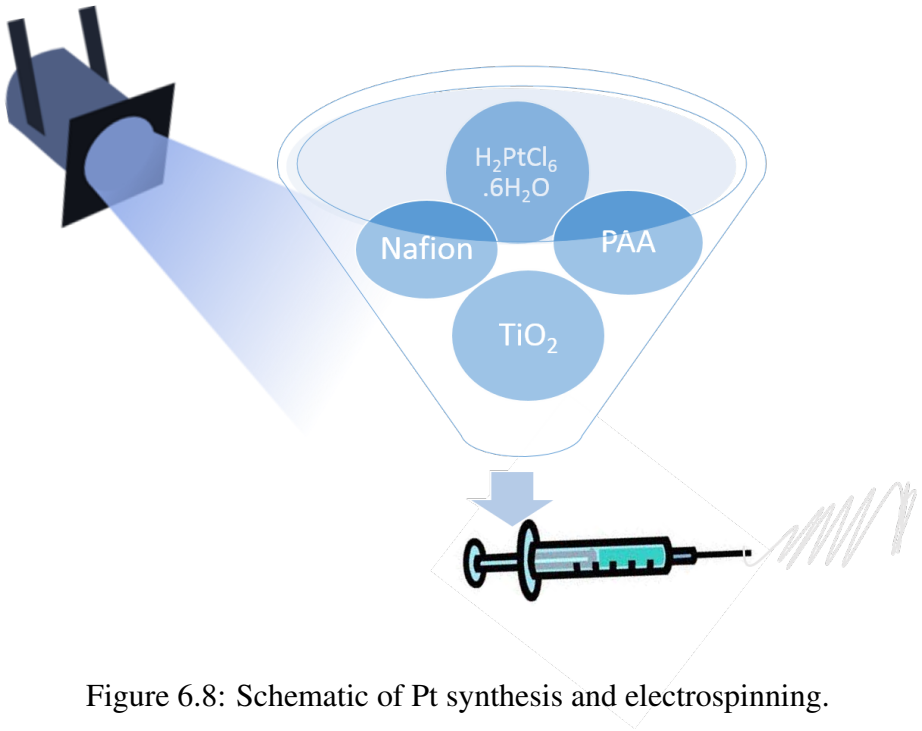

Figure 6.8: Schematic of Pt synthesis and electrospinning.

6.2.2 Results and discussion

The electrospinnability of PAA-Nafion solution is first checked by dissolving PAA and Nafion polymers alone in isopropanol-water to form the electrospinning solution. The solution is spun and was viewed using SEM. The nanofibers shown in Figure 6.9a have the typical spaghetti form with uniform fibers. In the next set of electrospinning experiments, TiO_2 was added to the existing PAA/Nafion polymer solution and was dispersed using ultrasonication and was afterwards electrospun. SEM images of the fibers are shown in Figure 6.9b.

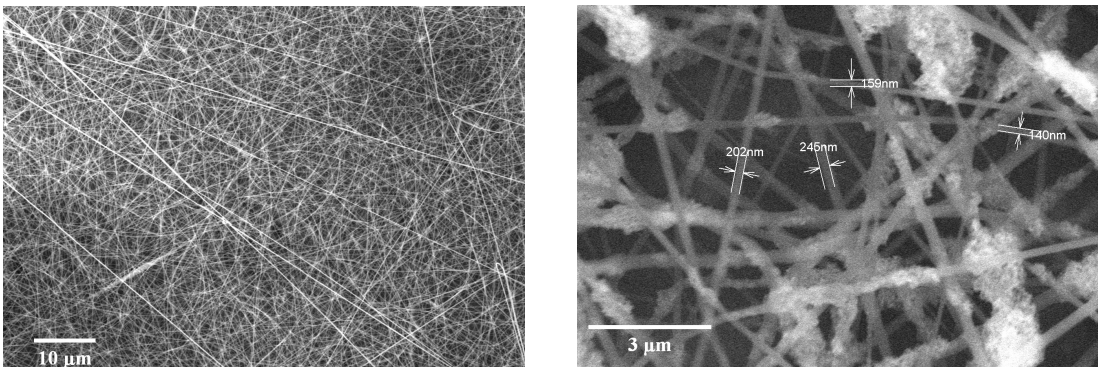

(a) (b)

Figure 6.9: SEM image of (a) electrospun PAA-Nafion fibers, (b) electrospun fibers of PAA-Nafion with TiO_2 particles.

The following five components: $H_2PtCl_6 \cdot 6\,H_2O$ (Pt), TiO_2, PAA, Nafion and solvent (1:1 isopropanol:water) are the components used for the preparation of the composite electrode.

Preparation of supported Pt nanoparticles in a solution in general consists of three steps:

1. Preparation of colloidal solution to stabilize the nanoparticles
2. Reduction of Pt salt to Pt nanoparticles.
3. Subsequent deposition on the support

Depending on the type, ratio and order of component addition, these have a significant effect on the spinnability and performance of the final electrode. The roles played by the individual components in the process is shown in Table 6.1.

It has been showed that ${PtCl_6}^{2-}$ could be reduced under UV light in isopropanol solution.

$$\mathrm{{PtCl_6}^{2-} + h\nu \rightarrow {PtCl_4}^{2-} + R{-}CH_2{-}OH \rightarrow Pt^0 + intermediates} \tag{6.1}$$

TiO_2 tends to enhance this reaction [132].

$$\mathrm{TiO_2 + h\nu \rightarrow e^- + h^+} \tag{6.2}$$

Figure 6.10 shows the solution before and after the reduction of the Pt precursor. The change in colour from yellow to black indicates formation of Pt nanoparticles.

Colloidal solutions were prepared using the different polymer constituents, i.e with PAA alone, with Nafion alone, with PAA and Nafion, and one without any Nafion or PAA.

Table 6.1: Role of different components used in the process.

Component	**Role in synthesis**	**Role in electrospinning**	**Role in fuel cells**
$H_2PtCl_6 \cdot 6\,H_2O$	Pt precursor	No major role	Catalysis
TiO_2	Enhance photocatalysis	No major role	Catalyst support
PAA	Colloidal agent	Electrospinning polymer	No major role
Nafion	Colloidal agent	No major role	Proton conduction
Solvent	Reducing agent	Solvent for electrospinning	Evaporated, not present

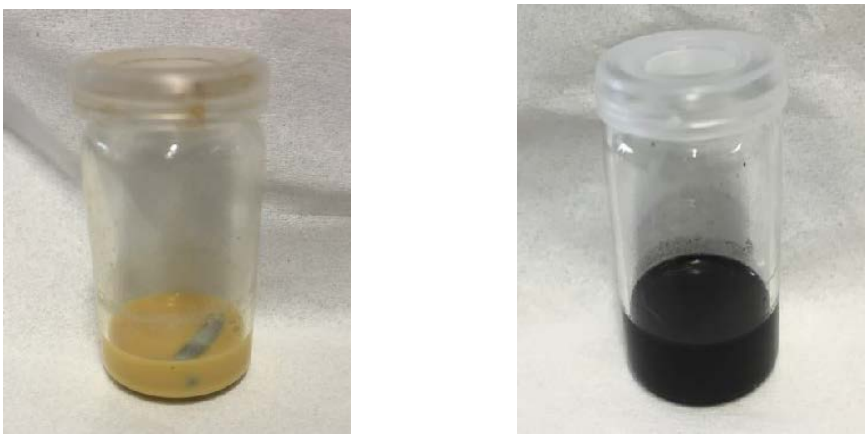

(a) (b)

Figure 6.10: Sample before and after photochemical reduction of Pt salt

Figure 6.11 shows the XRD patterns for these samples after reduction of the Pt salt. The reflections of Pt and TiO_2 are clearly seen and important reflections are indexed. TiO_2 is present in both anatase and rutile form with crystallite sizes of 18 nm for anatase and of 30 nm for rutile. The crystallite sizes of the Pt particles in the samples are tabulated in Table 6.2. From XRD alone, the crystallite sizes of the Pt nanoparticles obtained were 2.1 nm and 2.2 nm for Nafion and PAA, respectively. It can be thus inferred that both Nafion and PAA stabilize the newly formed Pt nanoparticles from crystal growth. When used together, the crystallite size is calculated to be 3.0 nm. Use of polymers play a decisive role in Pt synthesis, as without these polymers as a surfactant controlling particle size, Pt particles have a crystallite size of 5.5 nm.

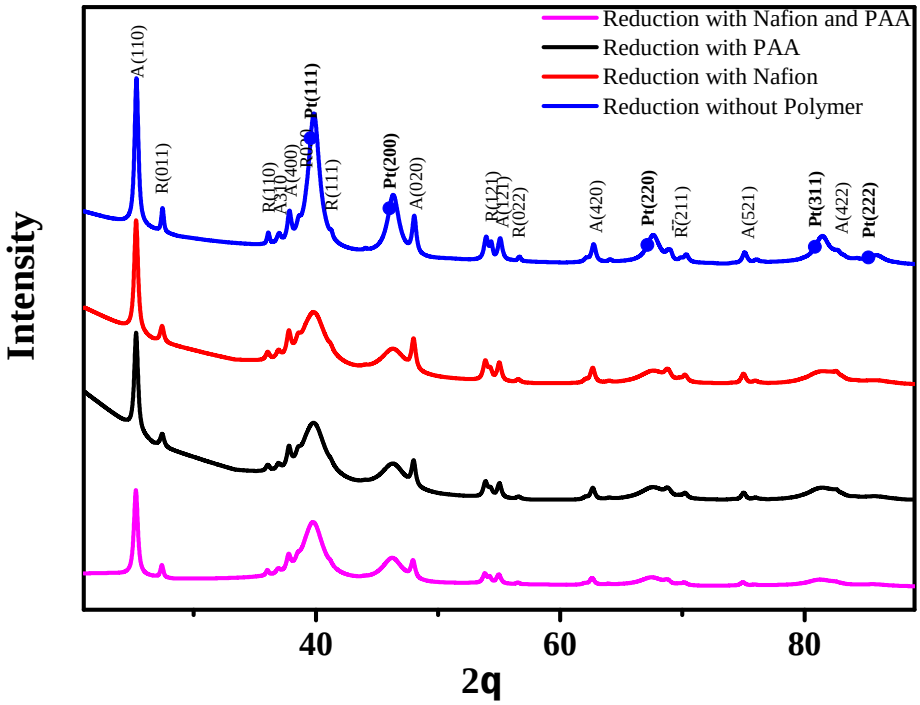

Figure 6.11: UV illumination induced reduction of $PtCl_6^{2-}$ with (—) polymer, (—) Nafion, (—) PAA and (—) without any polymer in a 1:1 water:isopropanol solution. A = Antase TiO_2, R = Rutile TiO_2 and Pt = Platinum.

The measured cyclic voltammograms of two differently synthesized 40 wt% Pt/TiO_2 samples are shown in Figure 6.12 and were recorded in a range between 0 V to 1.2 V. From the voltammograms, it can be seen that the hydrogen adsorption/desorption region (0 V - 0.4 V) which is used to determine the electrochemically active surface (ECSA) is significantly lower for Pt reduction without polymer than for the Pt reduced with PAA/Nafion. The ECSA is approximately 4 times higher for Pt reduced with polymers. A clear determination of the ECSA is not possible here, since the PAA swells in the solution.

Table 6.2: Crystallite size of platinum obtained from XRD analysis.

Preparation technique	Crystallite size of Pt
Reduction without polymer	5.5 nm
Reduction with PAA	2.1 nm
Reduction with Nafion	2.2 nm
Reduction with Nafion and PAA	3.0 nm

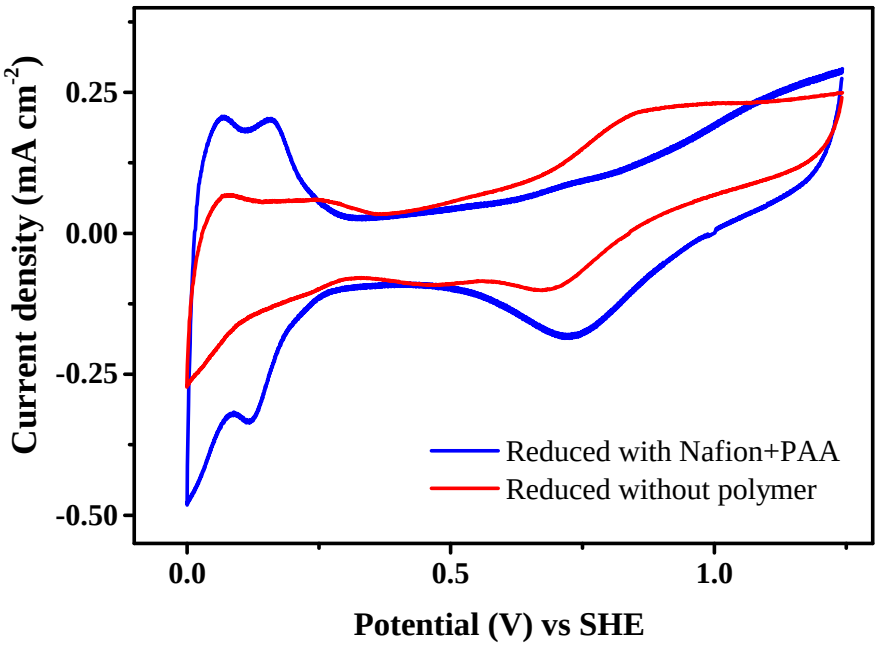

Figure 6.12: Cyclic voltammogram of Pt reduced with and without Nafion/PAA.

6.2.3 Fuel cell testing

To further study the sample obtained, fuel cell testing was carried out. However, repeated tests either produced dead cells or showed only marginal activity, which forced us to carry out some more investigations.

The electrospinning process has to be optimized in such a way that an electrode is obtained with the best possible composition for the latter application. However, after mixing all five composite components in the desired concentrations, it was found that no continuous spinning was possible. Figure 6.13a shows an SEM image of one of such electrodes. The typical spaghetti-like structure is seen along with spattering of the material. We encountered severe problems with the reproducibility of the electrospun electrodes.

Wang et al. [12, 92] recently obtained good results with the simultaneous use of electrospraying and electrospinning. In an alternating spraying and spinning process, they were able to demonstrate that there is a higher degree of control over fiber diameters and Pt/C agglomerations, which leads to 10 times higher performance. For this reason, the electrospinning solution in our attempts was diluted to favor electrospraying instead of electrospinning.

Figure 6.13b shows an SEM image of the electrosprayed catalyst. Electrospraying gives porous rough electrodes, which are similar to the airbrushed electrodes. Fuel cell testing was carried out for a 40 wt.% Pt catalyst which was electrosprayed on the GDL to achieve a loading of 0.19 mg_{Pt} cm^{-2}. Figure 6.13 shows the obtained polarization and power density curve for a H_2 - O_2 system at 70 °C. With this, a power density of 100 mA cm^{-2} at 0.6 V could be obtained, which is between 2 to 3 times below par compared to a commercial catalyst obtained in our test-bench single cell setup.

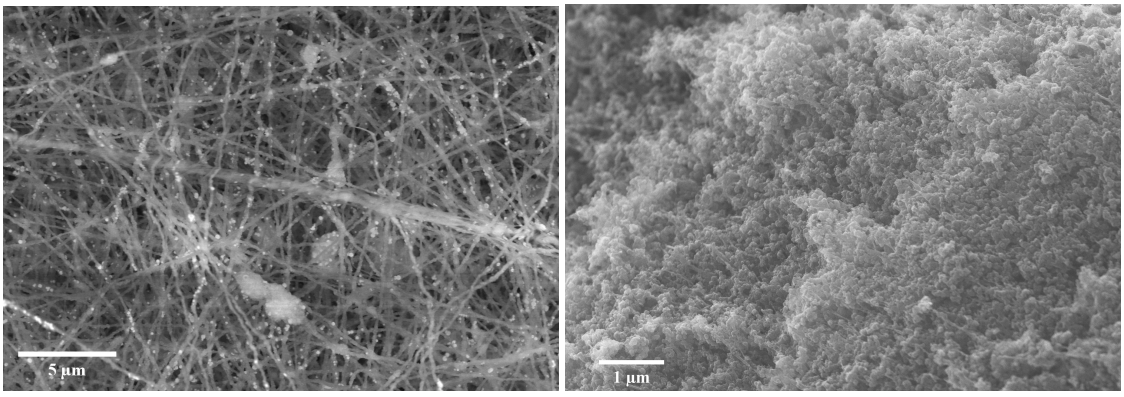

(a) (b)

Figure 6.13: SEM images of (a) electrospun and (b) electrosprayed electrodes.

TEM analysis gave a clear understanding of the issues persisting with the fabrication of MEAs. Figure 6.15 shows the TEM image of a single strand of the electrospun network. From the images obtained, the following observations were made:

1. Fibers consisted of long (not shown) as well as short fiber chains (shown in Figure 6.15 (a)) with variable diameters.

2. The solid materials, i.e TiO_2 and Pt nanoparticles, do not blend with the PAA-Nafion polymer uniformly. There are distinct parts in the fiber network, which do not contain any titania or Pt. In a Pt/TiO_2 electrode, Pt also plays the dual role of electrical conductivity apart from catalysis. Severe Agglomeration of Pt results in the discontinuity in electrical conductivity.

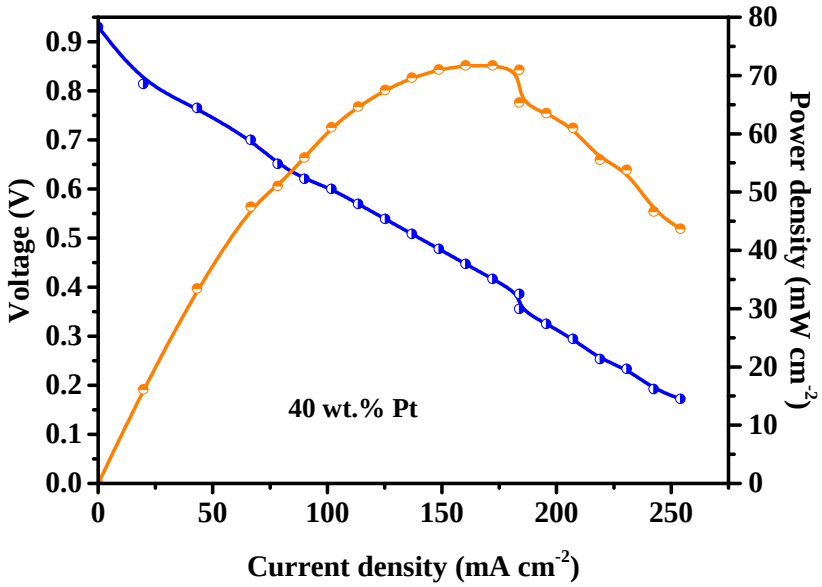

Figure 6.14: Polarization (—) and power density curve (—) of 0.19 mg_{Pt} cm^{-2} of an electrosprayed GDL (cathode) and 0.42 mg_{Pt} cm^{-2} commercial Pt/C catalyst (anode) for a H_2 - O_2 system at 70 °C.

3. The Pt particles do not deposit on the catalyst support, instead they agglomerate. The Pt agglomerates consist of really small individual particles, which has been confirmed by XRD. This might also be the reason of their high activity in cyclic voltammetry.

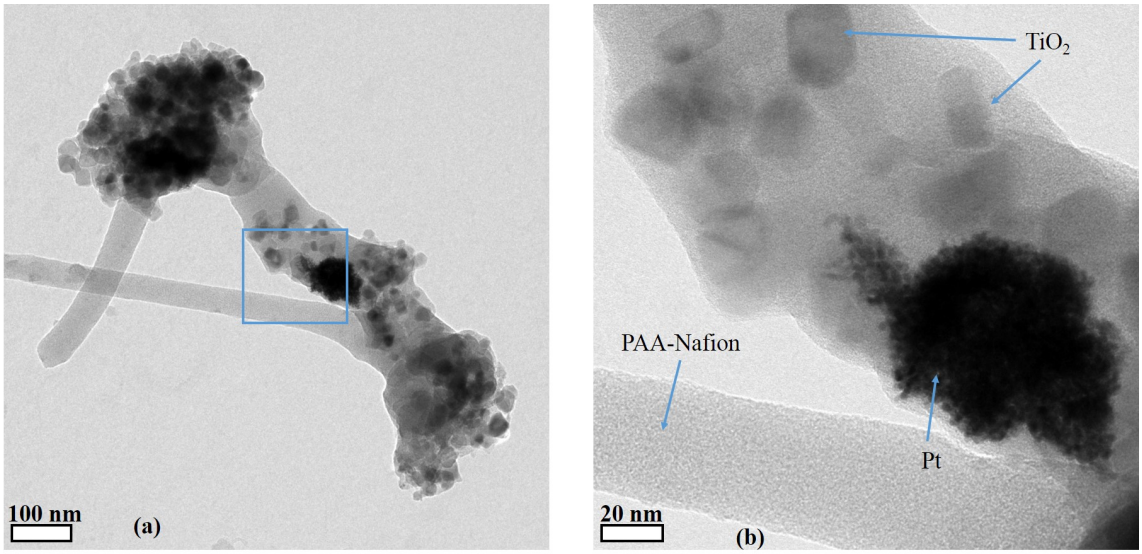

Figure 6.15: TEM images of electrospun fibers at different magnifications.

It was initially assumed that Pt, due to strong support interactions with TiO_2, would favorably deposit on it. This was found out later not to be the case, as seen from the TEM

images. Polymers played an influential role in the deposition of Pt. It is believed that the following properties of Nafion and PAA might have played a role in Pt deposition.

1. Nafion has been used previously for deposition of Pt as surfactant in low concentrations [133]. However, in our case, the concentrations used were much higher in order to be suitable for electrospinning and electrode preparation. This concentration is far higher than the critical micelle concentration [117] and this may play a vital role inducing the agglomeration of newly formed Pt nanoparticles.

2. Till to date, PAA has not been used in Pt or metal nanoparticle synthesis. PAA does not form micelles or inverse-micelle like structures. Further studies are required to study the influence of PAA on the deposition. We believe the polyacrylic acid, being an anionic polymer, has the ability to lose its proton and acquire a negative charge, and influence Pt ion and hence the Pt deposition.

6.2.4 Conclusion

An attempt, made to prepare electrospun Pt/TiO_2 catalysts which can provide a porous electrode, was met with limited success. The challenge was to create an optimal electrode with the best possible composition in line with the simultaneous optimization of the spinning process.This posed a complex problem, since different requirements were to be met.

Different loadings of Pt/TiO_2 were synthesized in-situ by reduction of Pt precursor by subjecting the electrospinning solution to UV illumination. In this reaction, both Nafion and PAA seem to act as stabilizers to synthesize Pt of 2-3 nm particle size. Correspondingly, cyclic voltammograms show high activity. MEA tests failed however, and TEM images revealed electrospun fibers with severe Pt agglomeration.

The chapter 5 was initiated after understanding and overcoming the difficulties faced in this project.

Chapter 7

Conclusion and Future outlook

In this thesis, application of the electrospinning technique in the preparation of porous fuel cell electrodes is presented. Two different concepts of using electrospinning were presented, which should help to improve their performance and stability. These tackled activity as well as durability of the electrodes and successful efforts were made to reduce Pt loading and accessibility.

Concept 1:
Electrospinning is a technique for the preparation of polymer nanofibers. Polymer fibers like polyacrylonitrile form carbon nanofibers under two step pyrolysis. Carbon nanofibers can themselves act as catalyst supports. However, addition of a small amount (2.5%) of carbon nanotubes strengthens the structure to become freestanding. These structures were highly porous with a volumetric porosity of $\approx 96\%$. The electrospinning resulted in layered networks which can be compressed by 35%. Pt salt was impregnated and reduced by a simple sodium borohydride solution reduction to get a uniform deposition of Pt nanoparticles with a crystallite size 5.3 nm and ECSA of 30.1 $m^2\ g_{Pt}{}^{-1}$. These catalysts when tested in fuel cells showed remarkably high Pt utilization of approx. 90% for a loading of 0.3 mg_{Pt} cm^2. In comparison, standard electrodes prepared via the hot-spray technique had a catalyst utilization of 60% only for the same loading. Morphology of the electrospun fibers was maintained throughout the process.

A novel electrode for fabrication of MEAs was thus developed which was independent of ink formulations promising a better electrode performance. The work presented in this part can be further developed and optimized. The future scope of the work is listed below:

1. Catalyst layer optimization: Porosity in the electrode allows for rapid transport of both fuel and water as well as protons and electrons to and from the electrodes. However, increasing the porosity results in disconnections in the catalyst - particle based electrode resulting in ohmic losses. For connected fiber structures, as found in this work, this needs not to be true. The electrospinning opens up a new class of electrodes consisting of fibers whose conductivity does not substantially decrease with high porosity. Most of the previous work done was optimized for powder catalyst. The ratio of preferred microporosity:mesoporosity:macroporosity is also optimized

for the powder catalyst. As a future outlook, catalyst layer optimization needs to be done for electrospun samples.

2. In this work, Pt nanoparticles had a size range of 5.3 nm which is comparatively high. An alternative deposition method should be tried to prepare smaller Pt nanoparticles (≈2 nm - 3 nm), which might be more active towards hydrogen oxidation and oxygen reduction.

3. A preliminary study on the stability of the electrode has shown positive results, but a full fuel cell electrode testing protocol with accelerated stability study needs to be carried out.

Concept 2:

Another concept which was covered in this thesis was to study the potential of a new group of polymers which are added to make Nafion electrospinnable. One such polymer, i.e polyacrylic acid (PAA), was chosen for the study. PAA-Nafion forms a highly stable composite which was studied as a potential Pt support . Using a novel preparation technique via photochemical reduction of Pt precursor, Pt nanoparticles were coated with PAA-Nafion polymer which separated carbon from Pt nanoparticles. This decreased Pt enhanced carbon corrosion which was tested with the potential cycling experiment and with the accelerated degradation studies on a fuel cell test-bench.

The future scope of this work is listed below:

1. The focus of the work was mainly on the stability of the electrodes. A further study and optimization of electrospinning needs to be carried out to further enhance their performance.

2. This material allows for the use of different carbons as physical mixtures. As an outlook mainly highly graphitic and stable carbon materials need to be studied.

There are definitely benefits of using electrospinning in the preparation of fuel cell electrodes, but there exist certain complications that need to be addressed.

1. Reproducibilty: There are a number of external factors like temperature, humidity, etc. that play a vital role in determining the size of the electrospun fibers. In case of addition of nanoparticles/fillers in electrospinning solution, dispersion of the particles should be uniform. A small unevenness in dispersion, which is often hard to detect, can affect the electrospinning process by an unprecedented manner like blocking of electrospinning

solution, spitting of the electrospun polymers etc. This can result in restarting the whole electrospinning process. The right recipes for an unknown fillers are difficult to foresee as most of the parameters are difficult to evaluate. Electrospinning solution recipes depend more on thumb rules than on exact equations.

2. Uniformity: It is not possible to determine the exact location in the collector where the electrospun fiber will deposit. This makes it difficult to prepare very thin uniform electrodes, often consisting of only 3 or 4 layers of the electrospun material. The issue can become further complicated, when preparing larger electrodes. This calls for further automation.

3. Versatility: Electrospinning is great for preparing highly porous electrodes, but for cases in which porosity needs to be reduced, it becomes complicated. A hybrid method involving simultaneous electrospinning and electrospraying may be used to overcome the issues of reproducibility, uniformity and versatility.

The use of electrospinning in fuel cell electrodes is relatively new, and there is not sufficient work regarding the preparation of bead-free nanofibers of very small size ranges (10 nm - 100 nm). Most of the focus so far was set on electrospinning for medical appliances which required a larger particle range (500 nm to 5 μm).

Finally to summarize, the application of the electrospinning technology puts a fresh perspective in fuel cell electrodes development, which brings in novel and promising ideas and concepts.

Bibliography

[1] Birol, F. Key World Energy Statistics 2016. 2016; http://www.iea.org/statistics/.

[2] NASA, NASA: Climate Change and Global Warming. 2016; http://climate.nasa.gov/.

[3] Stamenkovic, V.; Mun, B. S.; Mayrhofer, K. J. J.; Ross, P. N.; Markovic, N. M.; Rossmeisl, J.; Greeley, J.; Nørskov, J. K. *Angew. Chemie - Int. Ed.* **2006**, *45*, 2897–2901.

[4] Zhang, J.; Lima, F. H. B.; Shao, M. H.; Sasaki, K.; Wang, J. X.; Hanson, J.; Adzic, R. R. *J. Phys. Chem. B* **2005**, *109*, 11973.

[5] Yang, L.; Larouche, N.; Chenitz, R.; Zhang, G.; Lefèvre, M.; Dodelet, J.-P. *Electrochim. Acta* **2015**, *159*, 184–197.

[6] Wilson, M. S.; Gottesfeld, S.; Wilson, Mahlon S. Gottesfeld, S. *J. Electrochem. Soc.* **1992**, *139*, L28.

[7] Zhang, J.; Yin, G.; Wang, Z.; Shao, Y. *J. Power Sources* **2006**, *160*, 1035–1040.

[8] Wilson, M. S.; Gottesfeld, S. *J. Appl. Electrochem.* **1992**, *22*, 1–7.

[9] Rabat, H.; Brault, P. *Fuel Cells* **2008**, *8*, 81–86.

[10] Ramaswamy, N.; Arruda, T.; Wen, W.; Hakim, N.; Saha, M.; Gullá, A.; Mukerjee, S. *Electrochim. Acta* **2009**, *54*, 6756–6766.

[11] Thompson, S. D.; Jordan, L. R.; Forsyth, M. *Electrochim. Acta* **2001**, *46*, 1657–1663.

[12] Wang, X.; Richey, F. W.; Wujcik, K. H.; Ventura, R.; Mattson, K.; Elabd, Y. A. *Electrochim. Acta* **2014**, *139*, 217–224.

[13] Towne, S.; Viswanathan, V.; Holbery, J.; Rieke, P. *J. Power Sources* **2007**, *171*, 575–584.

[14] Antolini, E.; Gonzalez, E. R. *Solid State Ionics* **2009**, *180*, 746–763.

[15] Antolini, E.; Gonzalez, E. R. *Appl. Catal. A Gen.* **2009**, *365*, 1–19.

[16] PEM Fuel Cells. http://www.h-tec.com/uploads/pics/PEM{_}Brennstoffzelle{_}01.JPG.

[17] Toyota Mirai Fuel Cell Sedan Priced At $57,500 - Specs, Videos. http://insideevs.com/toyota-mirai-fuel-cell-sedan-priced-at-57500-specs-videos/.

[18] Daimler debuts next-gen Citaro fuel cell bus in Hamburg, cuts fuel consumption in half - Autoblog. http://www.autoblog.com/2009/11/17/daimler-debuts-next-gen-citaro-fuel.

[19] Centre for Sustainable Organisations, Sustainability Context. http://www.acgov.org/sustain/documents/fuelcellfactsheet.pdf.

[20] Toshiba : Press Release (22 Oct, 2009): Toshiba Launches Direct Methanol Fuel Cell in Japan as External Power Source for Mobile Electronic Devices. https://www.toshiba.co.jp/about/press/2009_10/pr2201.htm.

[21] Gasteiger, H. A.; Kocha, S. S.; Sompalli, B.; Wagner, F. T. *Appl. Catal. B Environ.* **2005**, *56*, 9–35.

[22] Mauritz, K. A.; Moore, R. B. *Chem. Rev.* **2004**, *104*, 4535–4585.

[23] Marcinkoski, J.; Spendelow, J.; Wilson, A.; Papageorgopoulos, D.; Reviewed, P.; Ahluwalia, R.; James, B.; Houchins, C.; Moton, J. Fuel Cell System Cost -2015. 2015; https://www.hydrogen.energy.gov/pdfs/15015_fuel_cell_system_cost_2015.pdf.

[24] Carter, D. *Fuel Cell Today* **2013**,

[25] Yu, J.; Matsuura, T.; Yoshikawa, Y.; Islam, M. N.; Hori, M. *Electrochem. Solid-State Lett.* **2005**, *8*, A156.

[26] Knights, S. D.; Colbow, K. M.; St-pierre, J.; Wilkinson, D. P. *J. Power Sources* **2004**, *127*, 127–134.

[27] Sethuraman, V. A.; Weidner, J. W.; Haug, A. T.; Protsailo, L. V. *J. Electrochem. Soc.* **2008**, *155*, B119.

[28] Liu, W.; Crum, M. *ECS Trans.* **2006**, *3*, 531–540.

[29] LaConti, A. B.; Liu, H.; Mittelsteadt, C.; McDonald, R. C. *ECS Trans.* **2005**, *1*, 199–219.

[30] Borup, R. L.; Davey, J.; Davey, J. R.; Garzon, F. H.; Wood, D. L.; Welch, P. M.; More, K. *ECS Trans.* **2006**, *3*, 879–886.

[31] Mitsushima, S.; Kawahara, S.; Ota, K. I.; Kamiya, N. *J. Electrochem. Soc.* **2007**, *154*, B153–B158.

[32] Fuller, T. F.; Gray, G. *ECS Trans.* **2005**, *1*, 345–353.

[33] Franco, A. A.; Gerard, M. *J. Electrochem. Soc.* **2008**, *155*, B367.

[34] Wood, D. L.; Davey, J. R.; Atanassov, P.; Borup, R. L. *ECS Trans.* **2006**, *3*, 753–763.

[35] Oszcipok, M.; Riemann, D.; Kronenwett, U.; Kreideweis, M.; Zedda, M. *J. Power Sources* **2005**, *145*, 407–415.

[36] Müller, A.; Kauranen, P.; Von Ganski, A.; Hell, B. *J. Power Sources* **2006**, *154*, 467–471.

[37] Bing, Y.; Liu, H.; Zhang, L.; Ghosh, D.; Zhang, J. *Chem. Soc. Rev.* **2010**, *39*, 2184–2202.

[38] Greeley, J.; Mavrikakis, M. *Nat. Mater.* **2004**, *3*, 810–815.

[39] Kuttiyiel, K. A.; Sasaki, K.; Choi, Y.; Su, D.; Liu, P.; Adzic, R. R. *Nano Lett.* **2012**, *12*, 6266–6271.

[40] Zhang, J.; Li, K.; Zhang, B. *Chem. Commun.* **2015**, *51*, 12012–12015.

[41] Mani, P.; Srivastava, R.; Strasser, P. *J. Power Sources* **2011**, *196*, 666–673.

[42] Strasser, P.; Koh, S.; Anniyev, T.; Greeley, J.; More, K.; Yu, C.; Liu, Z.; Kaya, S.; Nordlund, D.; Ogasawara, H.; Toney, M. F.; Nilsson, A. *Nat. Chem.* **2010**, *2*, 454–460.

[43] Sandru, Dealloying Process Creates More Efficient and Cheaper Platinum for Fuel Cells. 2010; `http://www.greenoptimistic.com/dealloying-platinum-fuel-cell-20100428/`.

[44] Stariha, S.; Artyushkova, K.; Serov, A.; Atanassov, P. *Int. J. Hydrogen Energy* **2015**, *40*, 14676–14682.

[45] Bashyam, R.; Zelenay, P. *Nature* **2006**, *443*, 63–66.

[46] Springer, T. E. *J. Electrochem. Soc.* **1993**, *140*, 3513.

[47] Marie, J.; Chenitz, R.; Chatenet, M.; Berthon-Fabry, S.; Cornet, N.; Achard, P. *J. Power Sources* **2009**, *190*, 423–434.

[48] Jiang, J.; Kucernak, A. *J. Electroanal. Chem.* **2002**, *520*, 64–70.

[49] Suzuki, A.; Hattori, T.; Miura, R.; Tsuboi, H.; Hatakeyama, N.; Takaba, H.; Williams, M. C.; Miyamoto, A. *Int. J. Electrochem. Sci.* **2010**, *5*, 1948–1961.

[50] Li, Y.; Fu, Z.-Y.; Su, B.-L. *Adv. Funct. Mater.* **2012**, *22*, 4634–4667.

[51] Antolini, E. *Appl. Catal. B Environ.* **2009**, *88*, 1–24.

[52] Dam, V. a. T.; de Bruijn, F. a. *J. Electrochem. Soc.* **2007**, *154*, B494.

[53] Mayrhofer, K. J. J.; Meier, J. C.; Ashton, S. J.; Wiberg, G. K. H.; Kraus, F.; Hanzlik, M.; Arenz, M. *Electrochem. commun.* **2008**, *10*, 1144–1147.

[54] Mathias, M.; Gasteiger, H.; Makharia, R.; Kocha, S.; Fuller, T.; Xie, T.; Pisco, J. *ACS Div. Fuel Chem. Prepr.* **2004**, *49*, 471–474.

[55] Roen, L. M.; Paik, C. H.; Jarvi, T. D. *Electrochem. Solid-State Lett.* **2004**, *7*, A19.

[56] Borup, R. L.; Davey, J. R.; Garzon, F. H.; Wood, D. L.; Inbody, M. A. *J. Power Sources* **2006**, *163*, 76–81.

[57] Huang, S.-Y. Y.; Ganesan, P.; Park, S.; Popov, B. N. *J. Am. Chem. Soc.* **2009**, *131*, 13898–9.

[58] Wang, J.; Yin, G.; Shao, Y.; Wang, Z.; Gao, Y. *J. Power Sources* **2008**, *176*, 128–131.

[59] Taniguchi, A.; Akita, T.; Yasuda, K.; Miyazaki, Y. *J. Power Sources* **2004**, *130*, 42–49.

[60] Makharia, R.; Yu, P.; Pisco, J.; Kocha, S. *ECS Trans.* **2004**, 25.

[61] Álvarez, G.; Alcaide, F.; Miguel, O.; Cabot, P. L.; Martínez-Huerta, M.; Fierro, J. *Electrochim. Acta* **2011**, *56*, 9370–9377.

[62] Park, S.; Shao, Y.; Kou, R.; Viswanathan, V. V.; Towne, S. A.; Rieke, P. C.; Liu, J.; Lin, Y.; Wang, Y. *J. Electrochem. Soc.* **2011**, *158*, B297.

[63] Kim, J.; Chun, Y.-S.; Lee, S.-K.; Lim, D.-S. *RSC Adv.* **2015**, *5*, 1103–1108.

[64] Chhina, H.; Campbell, S.; Kesler, O. *J. Electrochem. Soc.* **2007**, *154*, B533.

[65] Savych, I.; Subianto, S.; Nabil, Y.; Cavaliere, S.; Jones, D.; Rozière, J. *Phys. Chem. Chem. Phys.* **2015**, *17*, 16970–6.

[66] Antolini, E. *Appl. Catal. B Environ.* **2010**, *100*, 413–426.

[67] Bhardwaj, N.; Kundu, S. C. *Biotechnol. Adv.* **2010**, *28*, 325–347.

[68] Koski, A.; Yim, K.; Shivkumar, S. *Mater. Lett.* **2004**, *58*, 493–497.

[69] Chen, H.; Snyder, J. D.; Elabd, Y. A. *Macromolecules* **2008**, *41*, 128–135.

[70] Shenoy, S. L.; Bates, W. D.; Frisch, H. L.; Wnek, G. E. *Polymer (Guildf).* **2005**, *46*, 3372–3384.

[71] Ki, C. S.; Baek, D. H.; Gang, K. D.; Lee, K. H.; Um, I. C.; Park, Y. H. *Polymer (Guildf).* **2005**, *46*, 5094–5102.

[72] Pereira, R. F.; Barrias, C. C.; Granja, P. L.; Bartolo, P. J. *Nanomedicine* **2013**, *8*, 603–621.

[73] Cavaliere, S.; Subianto, S.; Savych, I.; Jones, D. J.; Rozière, J. *Energy Environ. Sci.* **2011**, *4*, 4761.

[74] Onozuka, K.; Ding, B.; Tsuge, Y.; Naka, T.; Yamazaki, M.; Sugi, S.; Ohno, S.; Yoshikawa, M.; Shiratori, S. *Nanotechnology* **2006**, *17*, 1026–1031.

[75] Aravindan, V.; Sundaramurthy, J.; Suresh Kumar, P.; Lee, Y.-S.; Ramakrishna, S.; Madhavi, S. *Chem. Commun.* **2015**, *51*, 2225–2234.

[76] Fetyan, A.; Derr, I.; Kayarkatte, M. K.; Langner, J.; Bernsmeier, D.; Kraehnert, R.; Roth, C. *ChemElectroChem* **2015**, *2*, 2055–2060.

[77] Liang, J.; Su, S.; Fang, X.; Wang, D.; Xu, S. *Mater. Sci. Eng. B* **2016**, *211*, 61–66.

[78] Mollá, S.; Compañ, V. *J. Power Sources* **2011**, *196*, 2699–2708.

[79] Choi, J.; Lee, K. M.; Wycisk, R.; Pintauro, P. N.; Mather, P. T. *J. Electrochem. Soc.* **2010**, *157*, B914.

[80] Kim, Y. S.; Nam, S. H.; Shim, H.-S. H.-S.; Ahn, H.-J. H.-J.; Anand, M.; Kim, W. B. *Electrochem. commun.* **2008**, *10*, 1016–1019.

[81] Shui, J.; Li, J. C. M. *Nano Lett.* **2009**, *9*, 1307–1314.

[82] Zamani, P.; Higgins, D.; Hassan, F.; Jiang, G.; Wu, J.; Abureden, S.; Chen, Z. *Electrochim. Acta* **2014**, *139*, 111–116.

[83] Shui, J.; Chen, C.; Grabstanowicz, L.; Zhao, D.; Liu, D.-J. *Proc. Natl. Acad. Sci.* **2015**, *112*, 10629–10634.

[84] Park, J.-H.; Ju, Y.-W.; Park, S.-H.; Jung, H.-R.; Yang, K.-S.; Lee, W.-J. *J. Appl. Electrochem.* **2009**, *39*, 1229–1236.

[85] Cavaliere, S.; Subianto, S.; Savych, I.; Tillard, M.; Jones, D. J.; Rozière, J. *J. Phys. Chem. C* **2013**, *117*, 18298–18307.

[86] Savych, I.; Bernard d'Arbigny, J.; Subianto, S.; Cavaliere, S.; Jones, D.; Rozière, J. *J. Power Sources* **2014**, *257*, 147–155.

[87] Li, M.; Zhao, S.; Han, G.; Yang, B. *J. Power Sources* **2009**, *191*, 351–356.

[88] Brodt, M.; Wycisk, R.; Pintauro, P. N. *J. Electrochem. Soc.* **2013**, *160*, F744–F749.

[89] Zhang, W.; Pintauro, P. N. *ChemSusChem* **2011**, *4*, 1753–1757.

[90] Brodt, M.; Han, T.; Dale, N.; Niangar, E.; Wycisk, R.; Pintauro, P. *J. Electrochem. Soc.* **2014**, *162*, F84–F91.

[91] Martin, S.; Garcia-Ybarra, P. L.; Castillo, J. L. *J. Power Sources* **2010**, *195*, 2443–2449.

[92] Wang, X.; Richey, F. W.; Wujcik, K. H.; Elabd, Y. A. *J. Power Sources* **2014**, *264*, 42–48.

[93] Rietveld, H. M. *J. Appl. Crystallogr.* **1969**, *2*, 65–71.

[94] Scherrer, P. *Gottinger Nachrichten Gesell* **1918**, *2*.

[95] Patterson, A. L. *Phys. Rev.* **1939**, *56*, 978–982.

[96] Hotaling, N. A.; Bharti, K.; Kriel, H.; Simon, C. G. *Biomaterials* **2015**, *61*, 327–338.

[97] Nock, R.; Nielsen, F. *IEEE Trans. Pattern Anal. Mach. Intell.* **2004**, *26*, 1452–1458.

[98] Ohma, A.; Shinohara, K.; Iiyama, A.; Yoshida, T.; Daimaru, A. **2011**, 775–784.

[99] Lefebvre, M. C. *Electrochem. Solid-State Lett.* **1999**, *2*, 259.

[100] Murthy, M.; Fuller, T. F.; VanZee, J. W.; S.Gottesfeld, Probing Electrode Structure Using Electrochemical Impedance Spectroscopy. Prot. Conduct. Membr. Fuel Cells -III - Proc. Int. Symp. Pennington, NJ, 2002.

[101] Liu, Y.; Murphy, M.; Baker, D.; Gu, W.; Ji, C.; Jorne, J.; Gasteiger, H. A. Determination of Electrode Sheet Resistance in Cathode Catalyst Layer by AC Impedance. ECS Trans. 2007; pp 473–484.

[102] Kim, C.; Yang, K.-S.; Lee, W.-J. *Electrochem. Solid-State Lett.* **2004**, *7*, A397.

[103] Rahaman, M. S. A.; Ismail, A. F.; Mustafa, A. *Polym. Degrad. Stab.* **2007**, *92*, 1421–1432.

[104] Johnson, D. J. *J. Phys. D. Appl. Phys.* **1987**, *20*, 286–291.

[105] Prilutsky, S.; Zussman, E.; Cohen, Y. *Nanotechnology* **2008**, *19*, 165603.

[106] Chayad, F. A.; Jabur, A. R.; Jalal, N. M. *Karbala Int. J. Mod. Sci.* **2015**, *1*, 187–193.

[107] Sadezky, A.; Muckenhuber, H.; Grothe, H.; Niessner, R.; Pöschl, U. *Carbon N. Y.* **2005**, *43*, 1731–1742.

[108] Cuesta, A.; Dhamelincourt, P.; Laureyns, J.; Martínez-Alonso, A.; Tascón, J. *Carbon N. Y.* **1994**, *32*, 1523–1532.

[109] Fischer, A.; Jindra, J.; Wendt, H.; A. Fischer, J. Jindra, H. W. *J. Appl. Electrochem.* **1998**, *28*, 277–282.

[110] Van Rheenen, P. R.; McKelvy, M. J.; Glaunsinger, W. S. *J. Solid State Chem.* **1987**, *67*, 151–169.

[111] Peuckert, M. *J. Electrochem. Soc.* **1986**, *133*, 944.

[112] Xu, Z.; Zhang, H.; Zhong, H.; Lu, Q.; Wang, Y.; Su, D. *Appl. Catal. B Environ.* **2012**, *111-112*, 264–270.

[113] Kim, H.; Subramanian, N. P.; Popov, B. N. *J. Power Sources* **2004**, *138*, 14–24.

[114] Baturina, O. A.; Aubuchon, S. R.; Wynne, K. J. *Chem. Mater.* **2006**, *18*, 1498–1504.

[115] Tarmyshov, K. B.; Müller-Plathe, F. *J. Chem. Phys.* **2007**, *126*, 074702.

[116] Merzougui, B.; Swathirajan, S. *J. Electrochem. Soc.* **2006**, *153*, A2220.

[117] Szajdzinska-Pietek, E.; Wolszczak, M.; Plonka, A.; Schlick, S. *Macromolecules* **1999**, *32*, 7454–7460.

[118] Yuan, X.; Wang, H.; Colinsun, J.; Zhang, J. *Int. J. Hydrogen Energy* **2007**, *32*, 4365–4380.

[119] Itagaki, M.; Hatada, Y.; Shitanda, I.; Watanabe, K. *Electrochim. Acta* **2010**, *55*, 6255–6262.

[120] de Levie, R. *Electrochim. Acta* **1964**, *9*, 1231–1245.

[121] Shinozaki, K.; Hatanaka, T.; Morimoto, Y. Pt Utilization Analysis Using CO Adsorption. ECS Trans. 2007; pp 497–507.

[122] Xu, H.; Brosha, E. L.; Garzon, F. H.; Uribe, F.; Wilson, M.; Pivovar, B. *ECS Trans.* **2007**, *11*, 383–391.

[123] Gasteiger, H.; Panels, J.; Yan, S. *J. Power Sources* **2004**, *127*, 162–171.

[124] Harada, M.; Einaga, H. *Langmuir* **2006**, *22*, 2371–2377.

[125] Grivin, V.; Khmelinski, I.; Plyusnin, V. *J. Photochem. Photobiol. A Chem.* **1991**, *59*, 153–161.

[126] Dong, B.; Gwee, L.; Salas-De La Cruz, D.; Winey, K. I.; Elabd, Y. A. *Nano Lett.* **2010**, *10*, 3785–3790.

[127] Dong, J.; Ozaki, Y.; Nakashima, K. *Macromolecules* **1997**, *30*, 1111–1117.

[128] Liang, Z.; Chen, W.; Liu, J.; Wang, S.; Zhou, Z.; Li, W.; Sun, G.; Xin, Q. *J. Memb. Sci.* **2004**, *233*, 39–44.

[129] Peter, B.; Melke, J.; Muench, F.; Ensinger, W.; Roth, C. *J. Appl. Electrochem.* **2014**, *44*, 573–580.

[130] Sherrell, P. C.; Zhang, W.; Zhao, J.; Wallace, G. G.; Chen, J.; Minett, A. I. *ChemSusChem* **2012**, *5*, 1233–1240.

[131] Li, X.; Chen, W.-X.; Zhao, J.; Xing, W.; Xu, Z.-D. *Carbon N. Y.* **2005**, *43*, 2168–2174.

[132] Ma, J.; Habrioux, A.; Alonso-Vante, N. *J. Solid State Electrochem.* **2013**, *17*, 1913–1921.

[133] Yin, S.; Mu, S.; Pan, M.; Fu, Z. *J. Power Sources* **2011**, *196*, 7931–7936.

Publications

1. **M. K. Kayarkatte**, O. Delikaya, C. Roth, *Freestanding Catalyst Layers: A novel electrode fabrication technique for PEM fuel cells via electrospinning* ChemElectroChem **2017**, **accepted** *http://dx.doi.org/10.1002/celc.201600530*.

2. **M. K. Kayarkatte**, O. Delikaya, C. Roth, *Evaluating PAA-Nafion as stable support for PEM fuel cells* Electrochim Acta, **under submission**.

3. C. Brieger, J. Melke, N. van der Bosch, U. Reinholz, H. Riesemeier, A. Guilherme Buzanich, **M. K. Kayarkatte**, I. Derr, A. Schkel, C. Roth, **J. Catal. 2016, 339, 57-67** *http://dx.doi.org/10.1016/j.jcat.2016.03.034*.

4. A. Fetyan, I. Derr, **M. K. Kayarkatte**, J. Langner, D. Bernsmeier, R. Kraehnert, C. Roth, **ChemElectroChem 2015, 2, 2055-2060** *http://dx.doi.org/10.1002/celc.201500284*.

Patents

1. K S Dhatatreyan, R. Natarajan, **M. K. Kayarkatte**, *A method of preparation of supported platinum nano particle catalyst in tubular flow reactor via polyol process*. (**Indian Patent: Published on 19/12/2014**)

Conferences

1. Presented a talk on,"*Freestanding Catalyst Layer Prepared via Electrospining for Proton Exchange Membrane Fuel Cells*" at Electrospinning and Energy conference (ElEn-2016), Montpellier, France.

2. Presented a poster titled, *PEM Fuel Cell Electrodes Prepared by Photocatalytically Deposited Pt on Titania and Successive Electrospinning* at ECS satellite meeting 2015, Glasgow, Scotland.

3. Presented a poster on *PEM Fuel Cell electrodes via electrospinning* at Gordon Research Conference - 2014, USA.

4. Presented a paper on, *Development of Porous Titania Electrodes for Fuel Cells* at a national level conference CHEMFERENCE-2011, Indian Institute of Science, Bangalore, India

5. Presented a paper on, *A Simple Algorithm for Rigorous Multi-Component Distillation Design* at ENGINEER-2009, NITK, Mangalore India

Curriculum Vitae

For reasons of data protection,
the curriculum vitae is not included in the online version.